Surface Chemistry of Silicon Anodes for Next-Generation Lithium-Ion Batteries

By

Joseph Crider Yeager

A dissertation submitted in partial fulfillment of

the requirements for the degree of

Doctor of Philosophy

(Chemistry)

at the

UNIVERSITY OF WISCONSIN-MADISON

2013

Date of final oral examination: 07/26/2013

The dissertation is approved by the following members of the Final Oral Committee:

Robert J. Hamers	Professor	Chemistry
John C. Wright	Professor	Chemistry
Kyoung-Shin Choi	Professor	Chemistry
Mahesh K. Mahanthappa	Associate Professor	Chemistry
Dane Morgan	Associate Professor	Materials Science & Engineering

Surface Chemistry of Silicon Anodes for Next-Generation Lithium-Ion Batteries

Joseph Crider Yeager

Under the supervision of Professor Robert J. Hamers

University of Wisconsin-Madison

Abstract

Batteries play a critical role in modern society and will only increase in importance as electric vehicles and grid-scale storage applications continue to grow. Silicon is a material of great interest as an anode for future battery applications, as it offers the possibility of greatly increased battery capacities and reduced weights. This work investigates two methods in which silicon may find use in batteries. First, silicon was shown to be a viable anode in primary battery systems using carbon monofluoride as a high-energy cathode for extremely high-temperature environments such as deep mineshafts. The temperatures achieved in these studies were some of the highest ever observed for a functioning lithium battery. In addition, the fundamental surface chemistry of silicon as a rechargeable anode for safer lithium-ion batteries was also investigated. Organosilicon-based electrolytes offer much higher flash points than the current generation of electrolytes, but the surface chemistry of their solid-electrolyte interphase formation on the silicon anode surface remains relatively unexplored until now. Finally, this work also presents a method for creation and subsequent functionalization of graphitic nanopillars. These nanopillars may serve as a route to well-ordered graphene nanoplatelets of monodisperse size and controllable chemistry.

Acknowledgements

This thesis is dedicated to the memory of Mike McCoy, who continues to remind me of what it means to be a good friend and a good person.

I owe a great debt to many colleagues from the Hamers group, past and present. Drew Mangham was a great first mentor and guide to running the group SEM, and Jamie Wheeler has proved to be a fine successor as I pass on that same torch. Though we overlapped a relatively short time, Beth Landis and Xiaoyu Wang were amazing role models of what great graduate students could be. Ryan Franking and Stephanie Hogendoorn both helped me learn some of the group's many instruments, from the inner workings of our network to the CVD plasma chamber. It was hard to stay in a bad mood when Rose Ruther was around, always accompanied by her infectious laughter, and her German lessons were the finest I've ever had. By my best estimate, I have consumed 1,825 L of coffee generously made by Yizheng Tan. Lee Bishop was a great project mentor for one fine summer as we collaborated on nanoparticle surface chemistry at a time when my own project was more than a little frustrating. The number of conversations I've had with Becca Putans, Linghong Zhang, and other office-mates is beyond counting; all of them were either very entertaining or highly productive, and some were even both. Laura Slaymaker deserves immense praise for surviving our collaborations for nearly a full year. I also owe a great debt to Xin Chen and Monica Usrey for getting me off to a running start in the world of batteries. And finally, I owe the greatest thanks to my fellow world traveler Kacie Louis, for being a fine mentor in the guise of a best friend.

I have been fortunate to have research support from a National Science Foundation Graduate Research Fellowship and from research funds provided by Silatronix Inc. I would also like to thank my advisor, Bob Hamers, for being a truly thoughtful and wise mentor throughout my time in grad school. Bob took in a young student who knew next to nothing about real, cutting-edge research, and more than anyone else is to thank for the scientist I have become. John Wright has also served on my committees since my early days, and was also one of my favorite professors to have in class. When I worked as a TA for Mahesh Mahanthappa during my first semester, I was constantly impressed by his teaching ability (which somehow didn't seem to suffer despite being to a room of 350 people), and he has continued to be a great mentor, collaborator, and committee member. Thanks also go to Frank Keutsch for serving on my TBO and RP committees and to Dane Morgan and Kyoung-Shin Choi for serving on my thesis committee.

Finally, no list of acknowledgements would be complete without mentioning my father, who sparked my interest in science; my mother, who sparked my interest in everything else; my brother, who still keeps me on my toes; and my wife, who still sweeps me off my feet.

Table of Contents

Chapter 1

Introduction and Background

1.1 Introduction to Batteries

Simply put, a battery is a device for storing energy in the form of chemical bonds where all active chemical species are permanently contained inside the cell (i.e. there is no "fuel")[1,2]. Only electrons enter and leave the battery, via two external terminals. These terminals each connect to an internal electrode. When the two external terminals are connected while the battery is in its charged state, electrons will flow through the completed external circuit and perform useful work. This occurs because inside the battery a spontaneous chemical reaction is occurring involving a reduction at one electrode (the cathode) and an oxidation at the other (the anode). The battery provides these electrons at a voltage equal to the difference between the electrochemical potentials of the reductive half-reaction and the oxidative half-reaction. Primary batteries are those that are assembled in the charged state and can only be discharged once; secondary batteries (commonly called rechargeable batteries) are generally assembled in the discharged state and may be charged and discharged many times.

In general the chemical species undergoing oxidation or reduction is either the electrode material itself (in the case of some metals) or another material adsorbed to the electrode surface. Strong adsorption is critical in order to make good electrical contact, as the electrons involved in the reduction or oxidation must travel easily to the metal electrode and therefore into the external circuit. The other critical component of any battery is the electrolyte (nearly always a liquid[3], but there are several examples of solid electrolytes[4,5]), which must be ionically conductive but insulating to electrons. The ionic conduction is necessary to balance the charges created by the

electrons moving during the reduction/oxidation reactions, and the electrolyte must be electronically insulating to prevent the flow of electrons entirely inside the battery ("shorting"), which would lead to very rapid self-discharging of the battery and complete impracticality. In many cases batteries are assembled with a porous material to serve as a separator between the electrodes[6]. This separator is often made from glass fibers or a porous polymeric sheet to provide electrical insulation and electrolyte permeability.

Batteries have several parameters typically used by investigators to characterize them that are functions of their construction and material composition. The *open-circuit voltage* (OCV, or sometimes open-circuit potential, OCP) of a battery is the voltage one would measure given an infinite resistance between the two terminals; it is what a voltmeter should read when connected to the battery. It is mainly a function of the two active materials (one at the cathode and one at the anode) that are undergoing the reduction and oxidation chemistry as well as the state of charge of the battery. The *state of charge* is commonly represented on any electronic device as the battery indicator. In more physical terms, the state of charge is simply the degree to which the battery will operate spontaneously – for example, a battery that is fully charged will operate spontaneously for the maximum time possible for its given electrode composition, and it will also have the highest open-circuit potential of any point in the battery's normal cycle. The battery will also have a *capacity* that is dependent on the amount of active material at the two electrodes (one will be usually be limiting) and represents the total number of electrons the cell can deliver spontaneously beginning from a full state of charge. Capacities are typically reported in the slightly unusual units of ampere-hours, which is equivalent to a unit of electric charge (1 A•h = 3600 Coulomb). When charging or discharging a battery, the cell will operate for a

particular amount of time that depends on the current drawn from or input into the battery. These experiments are often conducted at a particular *C-rate*, which is a measure of how many hours it will take to fully charge or discharge the battery. For example, a C/4 rate is equivalent to a current that will fully charge the battery (starting from the completely discharged state) in 4 hours, while a 4C rate represents a current that will fully charge the battery in 15 minutes. In general, when a battery is operated at a higher current (C-rate), the capacity achievable for the cell decreases somewhat compared to that obtainable at a lower current. This can be thought of as a kinetic limitation, with faster currents resulting in incomplete reactions and trapped redox species that are unable to complete the full set of reactions occurring in the cell.

1.2 Lithium Primary Batteries

A lithium primary battery is a type of non-rechargeable battery that uses lithium metal as the anode material[2,7]. Because lithium has the lowest electrochemical reduction potential on the common scale (-3.02V vs. NHE), it allows the construction of batteries with large open-circuit potentials. The large OCP in turn leads to batteries with a higher energy density. Lithium metal will react with oxygen, water, and even nitrogen gas, so such batteries must typically be assembled in dry rooms or, preferably, protected atmosphere environments such as an argon glove box. Lithium also has an extremely high inherent gravimetric capacity (approximately 3.86 Ah/g)[2], which permits construction of lightweight cells with high capacity. Primary lithium batteries are commonly found in watches, pacemakers, and other applications where light weight and long, stable performance are desirable and where recharging is either unnecessary (due to ease of replacement) or unfeasible (in the case of an internal medical device)[2].

One common cathode material paired with lithium primary batteries is carbon monofluoride (CF_x)[2,8]. Members of this class of materials are prepared by fluorination of a carbon precursor such as carbon fiber or graphite[9]. In a lithium-CF_x primary battery, Li metal atoms are oxidized to Li^+ cations at the anode surface during the discharge cycle, then subsequently travel through the electrolyte to the cathode surface and react with the CF_x to form LiF and another carbon byproduct. These batteries are primary cells because LiF is an extremely stable compound, and once it is generated, it cannot be decomposed again to regenerate the CF_x by running the cell in reverse. CF_x is an excellent cathode choice for many applications because of its extremely high gravimetric capacity (up to 735 mAh/g)[10] compared to other cathodes, long shelf life, and flat discharge profile. It has found particularly widespread use in applications like pacemakers where reliability and long-term stability are key attributes, while high current operation is not required[2].

1.3 Lithium-Ion Batteries

As illustrated in Figure 1.1, lithium-ion batteries are secondary (rechargeable) cells that operate by shuttling Li^+ cations between the anode and cathode during cycling, though neither electrode is made of Li metal and therefore the Li^+ is never formally reduced or oxidized itself[11,12]. Rather, by intercalation into the lattice of another material, the Li^+ cation induces an oxidation or reduction in its host. Lithium-ion batteries were first demonstrated by Goodenough and co-workers[13] in the 1980s and have played an extremely important role in the personal electronics boom of the last decade. Because lithium-ion batteries tend to have very high energy densities compared to other battery systems as well as reasonably long cycle lives, they are ideal

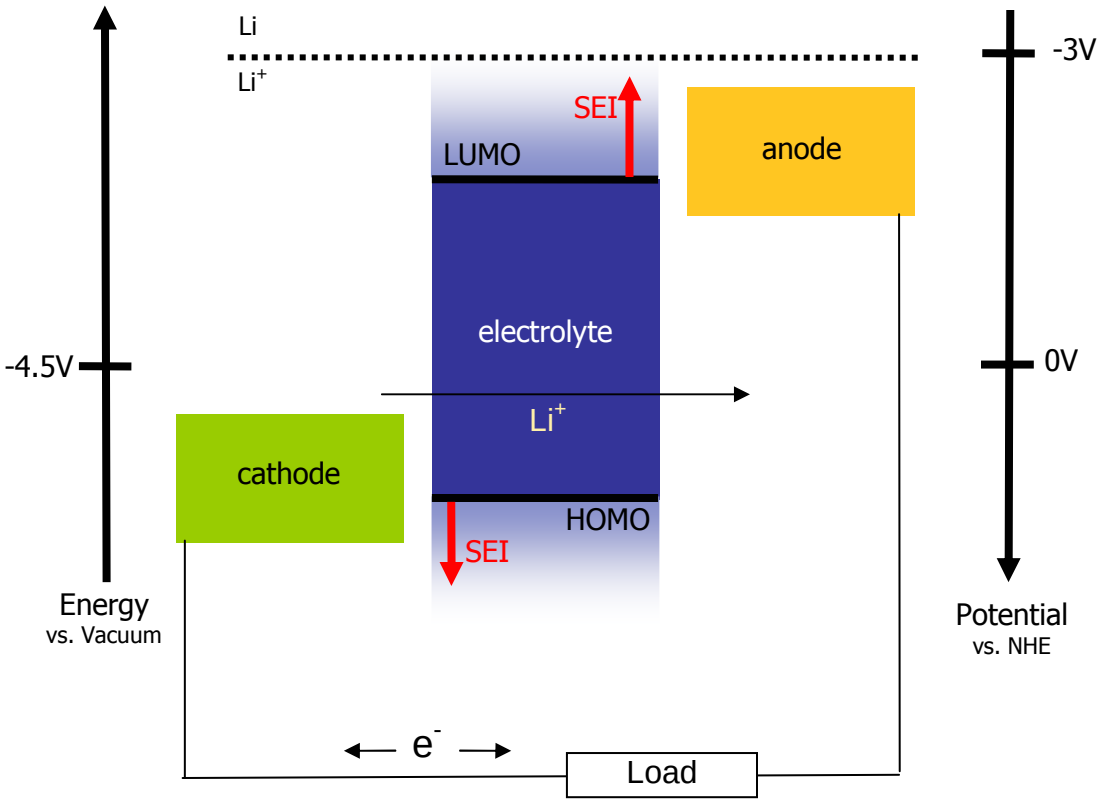

Figure 1.1 – A general schematic and energy diagram for a lithium-ion battery. The anode, cathode, and electrolyte are contained within the battery casing. Lithium cations travel through the electrolyte, while electrons travel through the external circuit and the load.

in many ways for the creation of small, lightweight battery packs for use in portable devices. The current generation of lithium-ion batteries are assembled using graphite anodes, lithium metal oxide cathodes, and an electrolyte consisting of an organic solvent and a lithium salt[14]. Each of these will be described in turn in the next sections.

1.3.1 Lithium-Ion Battery Anodes

Graphite has found extensive use in commercial lithium-ion batteries[2,15] because it is able to undergo many lithiation and delithiation cycles with little to no structural damage, because it operates at an electrochemical potential very close to that of lithium metal itself[16], and because it is relatively inexpensive and non-toxic. When a graphite anode is charged, lithium cations intercalate between the sheets of the graphite. Because lithium cations are quite small and the distance between graphene planes in graphite is already relatively large (approximately 3.4 Angstrom), the lithium intercalation does not drastically alter the volume of the graphite[17]. This is important because large volume changes could disrupt the mechanical state of the battery, leading to electric shorts, deformation of the cell casing, and/or loss of electrical contact inside the cell. Graphite is capable of forming several lithiated phases, principally LiC_{12} and LiC_6, the latter of which is the most lithiated phase[17]. Therefore, graphite possesses a moderate lithiation capacity (372 mAh/g) due to the relatively large number of atoms of the anode (6 carbon atoms) per atom of lithium in the fully charged state[18].

A matter of large concern when selecting a lithium-ion battery anode is the fact that the anode typically operates at an extremely reducing electrochemical potential. Many electrolyte solvents and salts are capable of being reduced at the potentials near 0V vs. Li/Li^+ (-3.02 V vs.

NHE), and therefore when the battery is charged, these electrolyte components will often react at the surface of the anode[19]. Commonly, these decomposition reactions produce solid products on the surface of the anode, forming a layer referred to as the Solid-Electrolyte Interphase (SEI)[20]. SEI formation can be detrimental to cell performance if it happens continuously or during part of each cycle, and therefore successful lithium-ion batteries must have electrolyte components that form a self-passivating SEI layer. A good SEI layer would ideally not hinder Li^+ transport at all, while being electrically insulating and chemically inert. Many portable devices powered by lithium-ion batteries instruct the user to ensure the battery is charged to 100% full the first time the battery is charged; the reason for this instruction is to form a well-structured SEI layer that will persist for the many future cycles of the battery.

For future lithium-ion battery applications, anodes with even higher lithium capacities are desired. Lithium itself has an extremely high gravimetric capacity (since there are no other atoms present) but presents a different problem: during repeated cycling, lithium metal does not plate evenly onto the electrode surface but instead forms dendrites that can reach out into the electrolyte. If these dendrites are permitted to grow long enough, they can even penetrate the cell separator and come into contact with the cathode on the opposite side of the cell[21]. When this occurs, an electrical short is created, a great deal of current passes through the lithium dendrite, and the dendrite becomes extremely hot as a result, possibly causing the electrolyte to combust. This process is the most common cause of lithium-ion battery fires, which have affected both personal electronics as well as larger-scale lithium-ion batteries such as those used in electric cars and on airplanes[22,23].

Instead of using lithium metal, then, future lithium-ion batteries must employ some other anode material that does not cause dendrite formation. Silicon is a very attractive candidate, as surprisingly, highly lithiated silicon can have an even higher atomic Li density than pure lithium metal does. This is true for both of the most lithiated phases, $Li_{22}Si_5$ (which is only formed at high temperature) and $Li_{15}Si_4$ (the most lithiated phase formed at room temperature)[24]. Silicon is also non-toxic and abundant in the earth's crust. The main concern when using silicon as an anode material is tied to its incredibly high capacity, in that such high degrees of lithiation cause significant amounts of volumetric expansion. For example, in transitioning from pure Si to $Li_{15}Si_4$, the material undergoes an approximately 300% increase in volume[24]. This change can fracture the particles of silicon depending on their size, leading to a loss of electrical contact or even pulverization of the internal cell components. Fortunately, this problem can be mostly mitigated by the use of nanoscale silicon particles[25]. On the other hand, the surface chemistry of silicon is quite different from that of graphite, and so even if an optimized electrolyte has formed an electrochemically stable SEI on the silicon, the SEI layer may not survive the mechanical expansions during charge and contractions during discharge. Therefore, effective practical use of silicon as an anode material in the future depends on understanding and optimizing the chemistry of the SEI layer formed on the silicon surface.

1.3.2 Lithium-Ion Battery Electrolytes

The current generation of lithium-ion batteries uses organic carbonates as the electrolyte solvent with a lithium salt dissolved at high concentration[3]. The most common salt used by far is $LiPF_6$, though others used include $LiBF_4$, lithium trifluoromethyl sulfonimide (LiTFSI)[26] and related compounds, and lithium bis-oxolatoborate (LiBOB)[27,28]. For the solvent, the most

commonly used compounds are linear carbonates such as diethyl carbonate (DEC), dimethyl carbonate (DMC), or ethyl methyl carbonate (EMC) with a significant fraction of ethylene carbonate (EC)[3]. Ethylene carbonate is a solid at room temperature so it cannot be used alone, hence the inclusion of the linear carbonates, which are much more volatile. EC is also important because it plays an important role in SEI formation, due to ring-opening reduction reactions that occur at the anode surface and form passivating layers[29]. Another common class of solvents that has found some use is the glyme family of linear ethers. For both the carbonates and glymes, the oxygen atoms in the solvent are able to chelate Li^+ cations, assisting in ion transport through the electrolyte[30].

The principal issues facing current lithium-ion battery electrolytes mainly stem from their high flammability. In order to enhance Li^+ conductivity of the electrolyte, solvents have been chosen that are relatively non-viscous and volatile, but this has the additional affect of decreasing their flash points. If electrolytes could be devised that possessed both high conductivity and a high flash point, the safety of lithium-ion batteries could be greatly improved. This is particularly important in the case of an accidental short created internally (such as by dendrite formation) or through external means (such as in a vehicle crash that deforms the cell casing). One must always keep in mind that batteries are, by design, chemical systems where large amounts of energy can be released exothermically, and every precaution must be taken to ensure that the energy can only ever be released through the desired load rather than through another path.

One class of molecules that offers promise for future battery systems are organosilicon compounds[31,32]. These compounds contain one or more silicon atoms (which generally increase the flash point) and generally one or more glyme units (to assist in Li^+ conduction)[33]. A large

variety of these molecules have been synthesized[34,35] and tested in battery cells, and the variety of structures available for synthesis provides the ability to custom-tailor the solvent to achieve the best balance of electrochemical and physical properties. In general, organosilicon electrolytes have exceptionally large voltage stability windows, high flash points, and can have high conductivities as well. Nevertheless, the chemistry of many of these compounds in contact with electrode surfaces remains relatively unknown.

1.3.3 Lithium-Ion Battery Cathodes

Typical cathodes used in modern lithium-ion batteries are metal oxide materials such as $LiCoO_2$ or $LiMn_2O_4$ [36], or other metal compounds such as $LiFePO_4$[37]. These materials all share the common characteristic of having at least one metal center in the unit cell that can be oxidized (as Li^+ leaves the cathode during the cell charge) and reduced (as Li^+ enters the cathode during discharge). In addition, these cathode materials also possess a relatively open structure, with either one-dimensional channels or two-dimensional layered planes that contain the lithium cations[12]. These pathways allow for efficient Li^+ transport as the cathode continuously charges and discharges. One drawback of this type of geometry is that not all of the lithium may be extracted, because if enough lithium leaves the cathode material, these channels or planes can collapse and form new structures that no longer permit lithium intercalation[38]. This is one reason that in general, current-generation cathodes possess lower lithiation capacities than graphite and therefore much lower capacities than next-generation anodes such as silicon.

The next generation of cathodes may consist of materials with multiple metal centers such as the family of materials containing nickel, manganese, and cobalt in the general formula $LiNi_xMn_yCo_zO_2$ [39]. Mixing metal centers in this way can create enough disorder in the lattice of

the cathode material that decreases the risk of structural collapse. In addition, next-generation cathodes will also most likely operate at higher potentials than $LiCoO_2$, which increases the total energy that the battery can store and subsequently produce. A major goal is to enable a cell that operates with an open-circuit potential of 5V, meaning the cathode is operating near 5V vs. Li/Li^+ (2V vs. NHE)[40]. This brings new challenges in terms of surface chemistry, since these more oxidizing potentials bring greater chance of electrolyte decomposition and SEI formation, though this problem is currently more prevalent on the anode side of the cell.

1.4 Graphite and Graphene

In a completely different realm from its application as a lithium-ion battery anode, graphite has also attracted a great deal of research effort in recent years due to its role as a precursor to graphene[41]. Whereas graphite consists of many stacked layers of sp^2-hybridized carbon, graphene is a single layer of such carbon. Though for many years graphene was predicted to be unstable with respect to transformations such as rolling into a spiral tube (thus destroying its inherent 2-dimensional nature), in 2004 Geim and co-workers successfully isolated graphene by a mechanical exfoliation technique[42]. This technique is simpler than it sounds and involves continually applying and then removing adhesive tape to a graphite sample until only one layer remains. Once isolated, graphene was quickly found to have a number of novel properties, including ballistic (non-scattered) charge transport, semi-metallic character, and the ability to display the quantum Hall effect[43], as well as impressive mechanical strength[44].

Despite the numerous groups working to probe graphene's unusual properties, synthetically the material remains difficult to produce in large quantities that are still pristine. The mechanical exfoliation technique produces the highest-quality graphene, but is quite slow

and cannot be used to produce large quantities. Similarly, epitaxial growth on copper or other substrates can produce large-area graphene of good quality, but is also relatively limited in scalability[45]. On the other hand, chemical oxidation and exfoliation of bulk graphite is easily scaled up, but produces a material known as graphene oxide (GO), which has myriad oxygen-containing functional groups randomly scattered throughout the graphene lattice[46]. Reduction of graphene oxide is possible, but never returns the material to the pristine graphene state, as some carbon atoms are completely removed during the oxidation process. Therefore, reduced graphene oxide (RGO) may only find use in some applications where a perfect graphene sample is not required.

The surface chemistry of graphite and graphene is somewhat unusual because of the highly anisotropic nature of the sp^2 carbon sheets. For both materials, the surfaces are distinguished between the edge plane and the basal plane. The basal plane is parallel to the graphene sheet and thus has no dangling bonds emerging from it, but instead only the π-orbitals of the sp^2-hybridized carbon rings. Therefore, the basal plane is quite chemically unreactive and electronic conduction is extremely slow in this direction, as conduction requires hopping the relatively large (and non-conjugated) distance between sheets[47]. On the other hand, the edge planes of graphite and graphene are perpendicular to the carbon sheets, and do contain dangling carbon bonds from the rings directly on the edge of each sheet. Graphite and graphene edge planes are therefore much more reactive than the basal plane, and electron transfer is approximately 10,000 times faster out of the edge plane than out of the basal plane[48]. In this manner, the edge planes of graphene and graphite dominate the surface chemistry of these materials.

1.5 Scope of This Thesis

Chapter 2 describes the development of lithium primary batteries capable of operating at extremely high temperatures, above the melting point of lithium metal. These cells employ a well-known cathode material, carbon monofluoride, which is notable for its very high energy density and also possesses good thermal stability. Instead of the traditional lithium metal anode typically used with carbon monofluoride cathodes, this study used pre-lithiated silicon anodes. Several different electrolytes were investigated in these high-temperature cells, and all three were shown to produce cells that could successfully operate at 190°C. Furthermore, several differences between the three electrolytes were noted in the course of the cell tests, and the chemical insights provided by those experiments are discussed.

Chapter 3 investigates the surface chemistry of single-crystal silicon anodes used in lithium-ion batteries in conjunction with organosilicon electrolyte solvents. These solvents have several attractive properties, among which are their very high thermal stabilities and flash points, indicating that they may soon find use in a new generation of safer lithium-ion batteries. Since this next generation of batteries may very well employ silicon anodes instead of the current generation of graphite-based anodes, it is critical to understand the surface chemistry occurring at the interface between the organosilicon electrolyte and the silicon anode. X-ray photoelectron spectroscopy (XPS) served as a primary tool to investigate the formation of solid-electrolyte interphase (SEI) layers at the anode surfaces.

Chapter 4 discusses older work on the surface chemistry of graphite, which consisted of both patterning and chemical functionalization. First, highly ordered pyrolytic graphite (HOPG) was coated with a block copolymer solution containing metal ions; these metal ions were later

reduced into metal nanoparticles segregated in particular locations on the graphite surface due to their preferential location in one block of the polymer. Once the particles were in place, plasma etching was used to anisotropically remove material from the graphite except where the metal nanoparticles acted as a protecting mask. The end result was to create many nanoscale pillars of well-ordered graphite discs stacked like plates, with edges exposed along the sidewalls of the pillars. As edge-plane graphite is significantly more reactive than the basal plane initially exposed on the surface before patterning, the next step was to functionalize these edges using both photochemical grafting of an alkene and the copper-catalyzed alkyne-azide cycloaddition reaction. Both XPS and Fourier-transform infrared spectroscopy (FTIR) were used to monitor the progress of the functionalization reactions.

Finally, chapter 5 concludes the thesis with a summary as well as some remarks about possible directions for future studies.

1.6 References

(1) Winter, M.; Brodd, R. *Chemical Reviews,* **2004,** *104*, 4245.

(2) Reddy, T. B.; Linden, D. *Linden's Handbook of Batteries*, 4th ed. McGraw-Hill Companies, New York, **2011**.

(3) Xu, K. *Chemical Reviews,* **2004**, *104*, 4303

(4) Stephan, A. M.; Nahm, K. S. *Polymer*, **2006**, *47*, 5952

(5) Minami, T.; Hayashi, A.; Tatsumisago, M. *Solid State Ionics*, **2006**, *177*, 2715

(6) Arora, P.; Zhang, Z. M. *Chemical Reviews,* **2004**, *104*, 4419

(7) Whittingham, M. S. *Chemical Reviews*, **2004**, *104*, 4271

(8) Endo, M.; Momose, T.; Touhara, H.; Watanabe, N. *Journal of Power Sources*, **1987**, *20*, 99

(9) Root, M. J.; Dumas, R.; Yazami, R.; Hamwi, A. *Journal of the Electrochemical Society*, **2001**, *148*, A339.

(10) Hany, P.; Yazami, R.; Hamwi, A. *Journal of Power Sources*, **1997**, *68*, 708

(11) Goodenough, J. B.; Park, K.-S. *Journal of the American Chemical Society,* **2013**, *135*, 1167.

(12) Hayner, C. M.; Zhao, X.; Kung, H. H. *Annual Reviews of Chemical and Biomolecular Engineering*, **2012**, *3*, 445

(13) Mizushima, K.; Jones, P. C.; Wiseman, P. J.; Goodenough, J. B. *Materials Research Bulletin*, **1980**, *15*, 783.

(14) Tarascon, J.-M.; Armand, M. *Nature,* **2001**, *414*, 359

(15) Mohri, M.; Yanagisawa, N.; Tajima, Y.; Tanaka, H.; Mitate, T.; Nakajima, S.; Yoshida, M.; Yoshimoto, Y.; Suzuki, T.; Wada, H. *Journal of Power Sources*, **1989**, *26*, 26.

(16) Flandrois, S.; Simon, B. *Carbon*, **1999**, *37*, 165.

(17) Dresselhaus, M. S.; Dresselhaus, G. *Advances in Physics*, **2002**, *51*, 1.

(18) Endo, M.; Kim, C.; Nishimura, K.; Fujino, T.; Miyashita, K. *Carbon*, **2000**, *183*, 197.

(19) Aurbach, D.; Ein-Eli, Y. *Journal of the Electrochemical Society*, **1995**, *142*, 1746

(20) Peled, E. *Journal of the Electrochemical Society*, **1979**, *126*, 2047.

(21) Yamaki, J.; Tobishima, S.; Hayashi, K.; Saito, K.; Nemoto, Y.; Arakawa, M. *Journal of Power Sources*, **1998,** *74*, 219.

(22) Drew, C. Boeing to Propose Redesign of 787 Battery to F.A.A. *The New York Times*, New York City, Feb. 21, 2013, p. B1.

(23) Muller, J. GM Moves Quickly To Put Out Chevy Volt Firestorm. *Forbes* [Online], Nov. 28, 2011. http://www.forbes.com/sites/joannmuller/2011/11/28/gm-moves-quickly-to-put-out-chevy-volt-firestorm/ (Accessed July 7, 2013).

(24) Obrovac, M. N.; Christianson, L. *Electrochemical and Solid State Letters*, **2004**, *7*, A93.

(25) Liu, X. H.; Zhong, L.; Huang, S.; Mao, S. X.; Zhu, T.; Huang, J. Y. *ACS Nano*, **2012**, *6*, 1522.

(26) Foropoulos, J.; DesMarteau, D. D. *Inorganic Chemistry*, **1984**, *23*, 3720.

(27) Xu, W.; Angell, C. W. *Electrochemical and Solid State Letters.*, **2001**, *4*, E1.

(28) Xu, K.; Zhang, S.; Jow, T. R.; Xu, W.; Angell, C. A. *Electrochemical and Solid State Letters*, **2002**, *5*, A26.

(29) Aurbach, D.; Ein-Eli, Y.; Markovsky, B.; Zaban, A.; Luski, S.; Carmeli, Y,; Yamin, H. *Journal of the Electrochemical Society*, **1995**, *142*, 2882.

(30) Fenton, D. E.; Parker, J. M.; Wright, P. V. *Polymer*, **1973**, *14*, 589

(31) Rossi, N. A. A.; West, R. *Polymer International*, **2009**, *58*, 267.

(32) Chen, X.; Usrey, M.; Peña-Hueso, A.; West, R.; Hamers, R. J. *Journal of Power Sources*, **2013**, *241*, 311.

(33) Zhang, L.; Zhang, Z.; Harring, S.; Straughan, M.; Butorac, R.; Chen, Z.; Lyons, L.; Amine, K.; West, R. *Journal of Materials Chemistry*, **2008**, *18*, 3713.

(34) Kricheldorf, H. R.; Al Masri, M. *Journal of Polymer Science Part A: Polymer Chemistry*, **1995**, *33*, 2667.

(35) Leska, B.; Gierczyk, B.; Eitner, K.; Rybachenko, V.; Schroeder, G. *Supermolecular Chemistry* **2004**, *16*, 303.

(36) Koksbang, R.; Barker, J.; Shi, H.; Saïdi, M. Y. *Solid State Ionics*, **1996**, *84*, 1.

(37) Chung, S.-Y.; Bloking, J. T.; Chiang, Y.-M. *Nature Materials*, **2002**, *1*, 123.

(38) Kang, K.; Meng, Y. S.; Bréger, J.; Grey, C. P.; Ceder, G. *Science*, **2006**, *311*, 977

(39) Yabuuchi, N.; Ohzuku, T. *Journal of Power Sources*, **2003**, *119-121*, 171.

(40) Ein-Eli, Y.; Howard, W. F. *Journal of the Electrochemical Society*, **1997**, *144*, L205.

(41) Novoselov, K. S.; Fal'ko, V. I.; Colombo, L.; Gellert, P. R.; Schwab, M. G.; Kim, K. *Nature*, **2012**, *490*, 192.

(42) Novoselov, K. S.; Geim, A. K.; Morozov, S. V.; Jiang, D.; Zhang, Y.; Dubonos, S. V.; Grigorieva, I. V.; Firsov, A. A. *Science*, **2004**, *306*, 666.

(43) Novoselov, K. S.; Geim, A. K.; Morozov, S. V.; Jiang, D.; Katsnelson, M. I.; Grigorieva, I. V.; Dubonos, S. V.; Firsov, A. A. *Nature*, **2005**, *438*, 197.

(44) Lee, C.; Wei, X. D.; Kysar, J. W.; Hone, J. *Science*, **2008**, *321*, 385.

(45) Li, X.; Cai, W.; An, J.; Kim, S.; Nah, J.; Yang, D.; Piner, R.; Velamakanni, A.; Jung, I.; Tutuc, E.; Banerjee, S. K.; Colombo, L.; Ruoff, R. S. *Science*, **2009**, *324*, 1312.

(46) Bagri, A.; Mattevi, C.; Acik, M.; Chabal, Y. J.; Chhowalla, M.; Shenoy, V. B. *Nature Chemistry*, **2010**, *2*, 581.

(47) Chung, D. D. L. *Journal of Materials Science*, **2002**, *37*, 1475.

(48) Rice, R. J.; McCreery, R. L. *Analytical Chemsitry*, **1989**, *61*, 1637.

Chapter 2

High-Temperature Carbon Monofluoride Primary Batteries Operating Above 180 °C Using Lithiated Silicon Anodes

2.1 Introduction

Lithium primary batteries (as well as the related rechargeable varieties) have experienced tremendous success in recent years due to their numerous attractive properties, including their combination of high energy density and power density relative to other types of batteries[1,2,3,4]. Lithium and lithium-ion batteries have found their way into most standard electronics, but applications exist where the conditions are too extreme for standard lithium battery formulations, such as very high and low temperature environments. For high-temperature operation, every cell component must be designed for stability at the operating temperature. In particular, deep mineshafts can have ambient temperatures above 150 °C, and battery systems are sought for autonomous robotic systems that operate at these depths. In such high-temperature environments, the principal areas of concern are the organic materials commonly used in the electrolyte[5] and the separator[6,7], the latter of which may even be designed to stop functioning slightly above the normal operating temperature to limit thermal runaway. A number of previous studies have pushed the boundaries of performance to 100 °C and higher[8,9,10], but with further work there is the potential to bring the capabilities of lithium-ion battery systems into environments at even higher temperatures.

Carbon monofluoride (CF_x) is an exceptional cathode material for primary (non-rechargeable) lithium-ion batteries due to its very high energy density (approximately 2190 Wh/kg), long shelf life, and stable discharge profile[11,12,13]. The typical anode paired with CF_x is

lithium metal, which produces a cell open circuit voltage of 3.2V and a typical operating voltage of 2.5-2.7V[11]. CF_x itself has also demonstrated stability up to 400 °C[11]. The main design challenge for CF_x batteries is the lithium metal anode, as the melting point of Li is 180 °C and molten lithium is an extremely difficult material to work with[14]. Using other anode materials could raise the temperature limit for practical usage, assuming the other components of the cell are also able to accommodate such high temperatures.

One approach to overcoming the limitation of bare lithium is to work with alloys of lithium with silicon or other elements. Of these, lithiated silicon has been most extensively studied because of the very high capacity for Li intercalation (3579 $mA \cdot h\ g^{-1}$ for $Li_{15}Si_4$)[15] and the very high thermal stability of lithium-silicon alloys, since the most lithiated phase ($Li_{22}Si_5$) melts above 600 °C, and less lithiated phases have even higher melting points[16].

Herein we report the construction of CF_x primary cells using lithiated silicon anodes in place of lithium metal and demonstrate the successful operation of these primary cells using several different electrolytes at operating temperatures up to 200 °C.

2.2 Experimental Methods

We investigated electrodes made from both nanocrystalline silicon and from single-crystal silicon wafers. Initial studies showed that cells made using nanocrystalline silicon showed poor performance due to very fast loss of open-circuit voltage at high temperatures. Therefore, in order to demonstrate a proof of concept, we focused on anodes made from single-crystal wafers.

2.2.1 Pre-lithiation of Silicon

While lithiated silicon anodes can be made by several processes, we chose to make them by direct electrochemical intercalation of lithium into crystalline silicon wafers. Silicon (100) wafers (B-doped, < 0.004 Ω·cm, Addison Engineering) were cut into ~1cm^2 squares to fit into a 2032 coin cell. The (100) face was chosen for this application since studies have shown lithium intercalation into silicon is relatively fast through this crystal plane[17]. Coin cells were assembled in an argon glove box using Celgard 3401 separators and one of several electrolytes selected for high-temperature operation capability as shown in Figure 2.1a. Although these pre-lithiation cells were not operated above 25 °C, the high-temperature electrolytes were still used so that SEI layer and any intercalated electrolyte would stay consistent and compatible throughout the experiments. Electrolyte formulations were composed of 1M $LiBF_4$ (Aldrich, anhydrous, 99.998%) in a solvent of either tetraglyme (Novolyte), propylene carbonate (Aldrich, dried over CaH_2), or (3-(2-(2-methoxyethoxy)ethoxy)propyl)fluorodimethylsilane, hereafter referred to as F1S3M2 (Silatronix). Li foil (Rockford Lithium, 0.008" thickness) was used as counter electrode. Cells were charged at 100 μA to a set total capacity, usually 10 mA·h, using an Arbin Instruments MSTAT 12-channel battery tester or an Arbin BT-G-502 16-channel battery tester. After reaching the final capacity, the cells were disassembled and the lithiated silicon electrode extracted immediately before use in the high-temperature experiments.

2.2.2 High-Temperature Operation

CF_x films were cast from a slurry consisting of CF_x powder (Advance Research Chemicals, Carbofluor 3000), sodium carboxymethylcellulose (CMC) binder (Aldrich, M_w ~90,000), and carbon black (Alfa Aesar, 99.9+%) in 18 MΩ·cm water. The slurry was mixed so

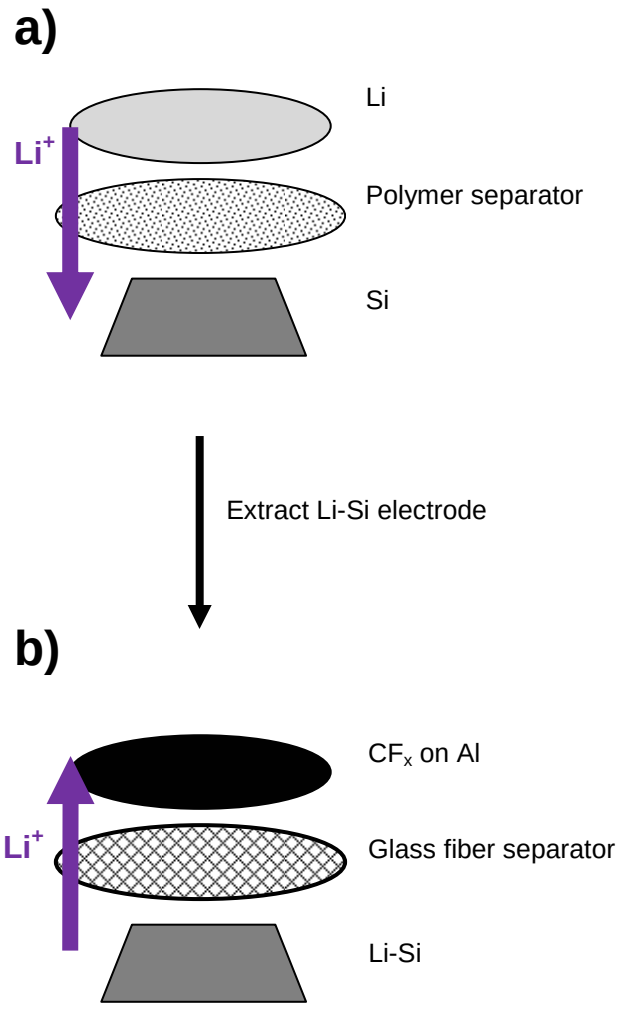

Figure 2.1. Schematic of typical cells used in this investigation. a) The precursor half-cell using a Li metal anode, a traditional polymer separator, and a piece of Si wafer as cathode. This cell was charged at room temperature to produce a lithiated silicon (Li-Si) electrode, which was extracted after charging. b) The high-temperature full cell using a CF_x cast film cathode, glass fiber separator, and the extracted Li-Si anode.

that the final composition of the electrode film was 90% CF_x, 5% CMC binder, and 5% carbon black by weight. CMC was chosen as binder for its extremely high melting point of approximately 274 °C. The films were cast at 250 μm thickness onto aluminum foil (15 μm thickness, MTI) and allowed to dry in air for 12 h and then in a vacuum oven at 130 °C for 24 h.

The pre-lithiation cells described in section 2.1 were disassembled after reaching the desired capacity and the Li-Si electrode was extracted. As seen in Fig 2.1b, the Li-Si electrode and a CF_x cast film electrode were placed into a custom-built electrochemistry cell made of Polyether ether ketone (PEEK) and stainless steel components. The custom cell was needed due to the fact that typical coin cells use a polypropylene sealing gasket that melts at the testing temperatures. All cells were built inside an argon glove box. Glass fiber filter discs (Sterlitech GD-120) were used as separators and were soaked in the high-temperature electrolyte before being placed into the cell. The cell was sealed with two Kalrez O-rings, one above and one below the electrode stack. The sealed cells were then removed from the glove box, placed into an oven at room temperature, and connected to the battery tester through a port in the top of the oven.

2.2.3 Characterization

All electrochemical tests on full cells were conducted using an Arbin Instruments MSTAT 12-channel battery tester. The standard test program began with 4 hours of rest while monitoring the open-circuit potential of the battery. Typical open-circuit potentials were between 2.5 and 3.0 V vs. Li/Li^+. The temperature was increased from room temperature to a minimum of 190 °C at approximately 1 h into this rest period. This procedure allowed the cells to reach the

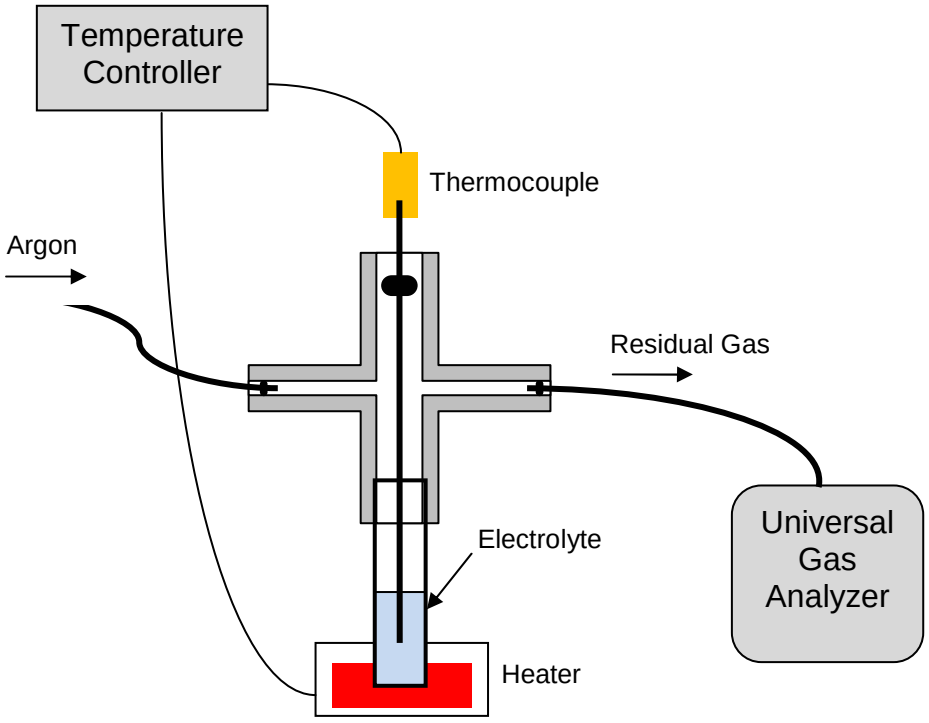

Figure 2.2. A schematic of the UGA setup to investigate the thermal breakdown of electrolytes. The temperature is set and controlled by the PTC while the UGA monitors any gaseous products as the temperature is increased. The cell is continuously purged with argon to provide a clean and nonreactive atmosphere.

elevated temperature and re-equilibrate before any current was applied. After the rest period completed, cells were discharged at a constant current of 100 μA until the potential fell to 0.5 V vs. Li/Li^+.

To detect any gas evolution due from the electrolytes (either alone or with an electrode present) at high temperatures, atmospheric-sampling mass spectrometry data were collected using a Stanford Research Systems UGA200 universal gas analyzer. The electrolytes were placed into a custom-built cell consisting of a small glass vial containing the electrolyte, a thermocouple immersed in the solution, and a sealed line that allowed for argon purging and gas collection by the UGA (see figure 2.2). Temperatures were controlled using a Stanford Research Systems PTC10 programmable temperature controller connected to the thermocouple.

2.3 High-Temperature Discharge Results

2.3.1 Tetraglyme Electrolyte

Tetraglyme was selected as an initial electrolyte solvent for high boiling point of ~275 °C. Figure 2.3a shows the discharge performance of a full cell consisting of a lithiated silicon anode and a CF_x cathode with tetraglyme/$LiBF_4$ (1M) electrolyte at 200 °C. As the cell temperature increased during the initial rest period, a series of small fluctuations appeared in the cell open-circuit potential (OCP). Typical magnitudes of the potential variations were approximately 0.1 - 0.3 V. These fluctuations in potential may be due to formation of surface layers or changes in the conductivity of cell components with temperature.

After the cell re-equilibrated and the 4-hour rest period ended, discharge of the cell began. The voltage quickly dropped to a plateau at approximately 2.5 V, where it remained until

the discharge was nearly completed more than 10 hours later. As shown, the cell survives the extremely high-temperature environment until the final voltage drop as the cell finishes discharging. One limitation of this system is its capacity: though the cell was anode-limited and should have showed a total capacity of approximately 10 mA·h, it was only able to discharge 1.4 mA·h, less than 15% of the theoretical full cell capacity. This implies significant capacity losses in one or both electrodes at these high temperatures.

2.3.2 Propylene Carbonate Electrolyte

Propylene carbonate (PC) was chosen as a second electrolyte solvent because of its high boiling point and ability to dissolve high concentrations of $LiBF_4$. Figure 2.3b shows the discharge performance of a full cell consisting of a lithiated silicon anode and a CF_x cathode with PC/$LiBF_4$ (at a concentration of 1M) electrolyte at 190 °C. The performance of the cell is comparable to that of one using the tetraglyme electrolyte, showing a moderately flat discharge region at approximately 2.5V that lasts for approximately 8 hours. Like the cell with tetraglyme-based electrolyte, the discharge capacity obtained is significantly lower than the theoretical capacity of this anode-limited cell – in this case, only about 10% of the theoretical value. Nevertheless, these results indicate that either propylene carbonate or tetraglyme can perform for at least 8 hours in these high-temperature cells.

2.3.3 F1S3M2 Electrolyte

The organosilicon electrolyte F1S3M2 is similar to glyme-based electrolytes in part of the molecule (which serves to chelate to the Li^+ ions dissolved the electrolyte[18]) but differs via

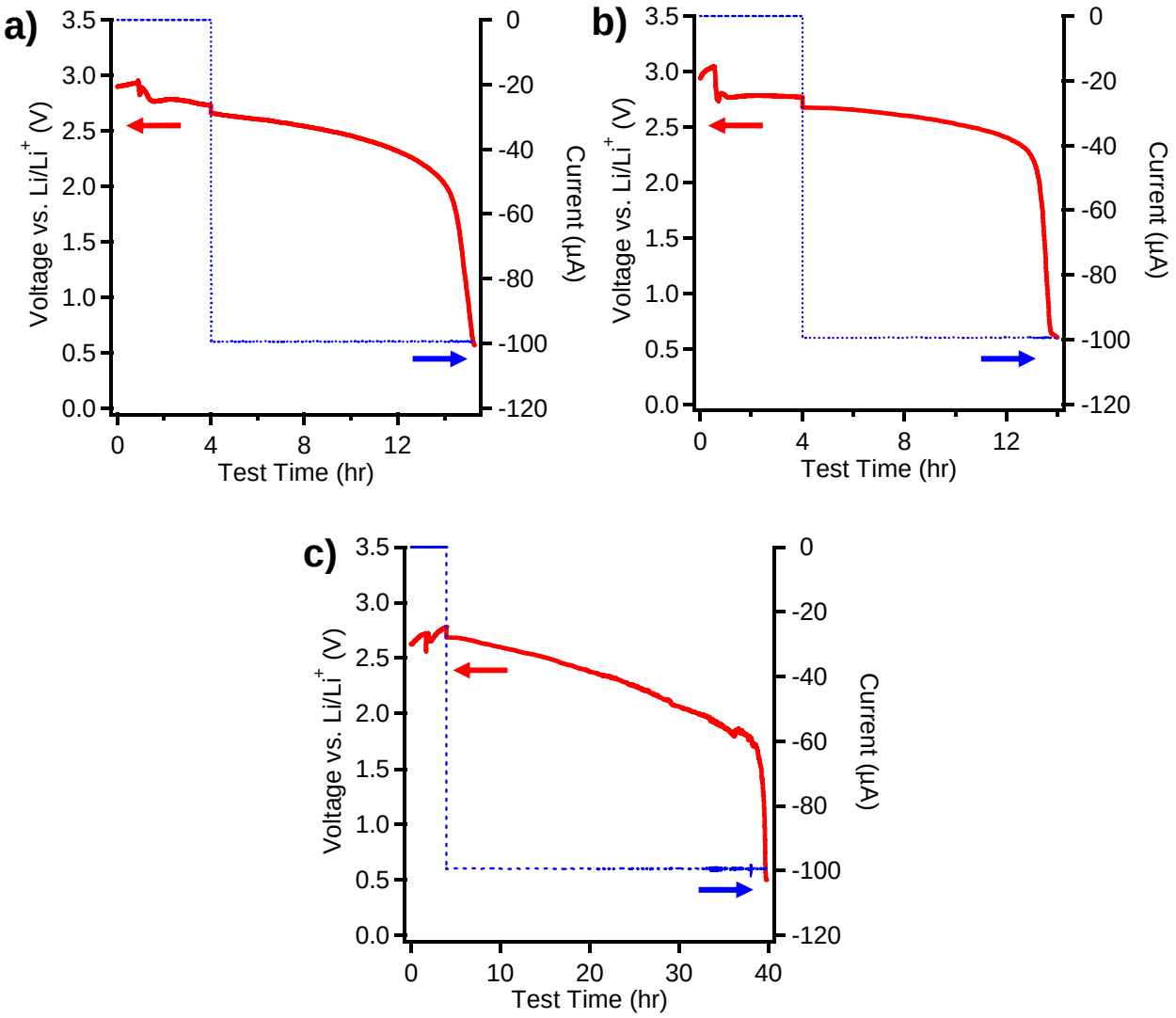

Figure 2.3. The discharge curves for cells containing a pre-lithiated silicon (100) wafer piece and a CF_x film electrode with either a) tetraglyme/$LiBF_4$ (1M) electrolyte, b) propylene carbonate/$LiBF_4$ (1M) electrolyte, or c) F1S3M2/$LiBF_4$ (1M) electrolyte. The graph shows both the voltage (solid red curve, left axis) and current (dashed blue curve, right axis) profiles. The fluctuation at approximately 1h into the initial resting period occurs during the temperature increase of the oven.

the substitution of a silicon atom one end. In general, organosilicon electrolytes possess superior stability at high temperatures versus traditional electrolyte solvents such as alkyl carbonates[19,20,21]. Most organosilicon electrolytes investigated previously contain an Si-O bond that can be easily attacked by fluorinated salt decomposition products[22,23]. The specific compound chosen here replaces the Si-O bond with Si-C and Si-F bonds. Figure 2.3c shows the discharge curve for a cell containing lithiated silicon and a CF_x cast film electrode using an F1S3M2/$LiBF_4$ (1M) electrolyte at 190 °C. Comparison of these data with the results of the tetraglyme and propylene carbonate electrolyte tests shows that the F1S3M2 electrolyte maintains its output voltage for a significantly longer time, although the discharge curve is not as flat. Over the course of the 35+ hours of cell operation, the operating voltage of the cell decayed from approximately 2.7 V to 1.7 V before finally dropping precipitously at the end of the cell lifetime. Because of the longer discharge time, this cell was able to achieve a better fraction of its theoretical capacity (approximately 40%) compared to those cells using either tetraglyme or propylene carbonate as electrolytes.

2.4 Factors Affecting High-Temperature Breakdown

2.4.1 Silicon Self-Discharge and Room-Temperature Discharge

To further investigate the reduced capacity of the high-temperature cells, high-temperature self-discharge experiments were conducted. Si wafer pieces were lithiated to varying charge capacities and then sealed into identical high-temperature cells with a CF_x cathode and high temperature electrolyte. The temperatures were immediately raised to 190 °C while the OCP was monitored, but no discharge current was ever allowed to pass through the cells. Figure

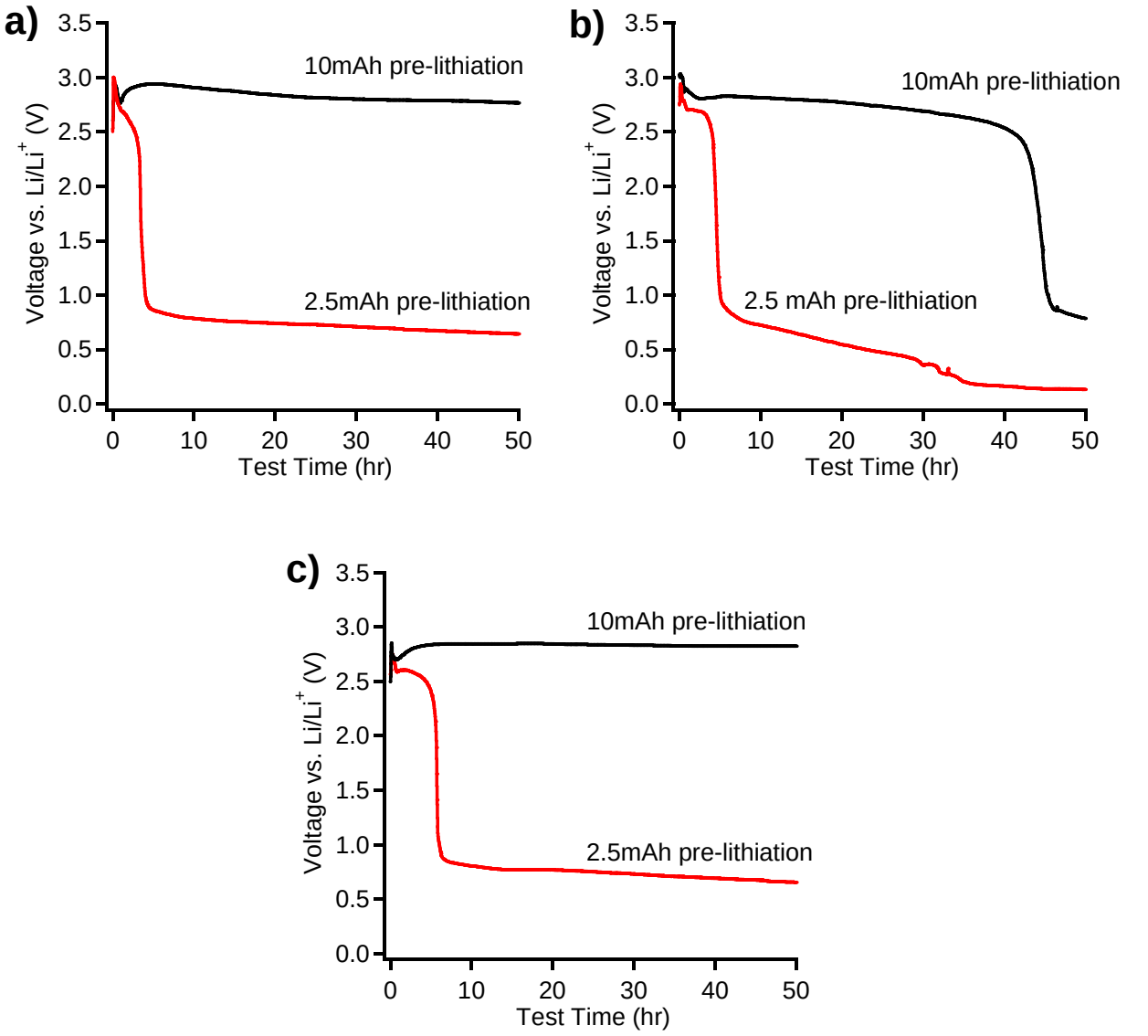

Figure 2.4. The open-circuit voltage of cells containing silicon wafer samples pre-lithiated at 10mA·h (black curves) and 2.5mA·h (red curves). The electrolytes used are a) tetraglyme/$LiBF_4$ (1M), b) propylene carbonate/$LiBF_4$ (1M), and c) F1S3M2/$LiBF_4$ (1M). In each case, the temperature of the oven containing the cells was increased from 25 to 190 °C at the same moment as voltage monitoring commenced.

2.4 shows the resulting curves of OCP versus time spent at 190 °C for each of the three electrolyte systems studied. For each electrolyte, the top curve, representing a cell containing a Si wafer lithiated to 10 mA·h, maintained its OCP above 2.5V for more than 40 hours. Furthermore, the PC-containing cell did eventually decrease in potential after approximately 45 hours, while the tetraglyme- and F1S3M2-containing cells survived for the entire duration of the test (50 hours). In contrast, the bottom curve in each graph, representing a cell containing a Si wafer lithiated to only 2.5 mA·h, showed an OCP decrease to below 1.0 V within the first 6 hours.

We also conducted tests with Li-Si + CF_x cells identical to those in sections 3.1-3.3 but discharged at room temperature. Figure 2.5 shows the voltage and current curves for three cells held at 25 °C during discharge, one each for the three electrolytes investigated in this work. Each is able to discharge for over 75 hours at 100μA, representing a discharge capacity of 78, 79, and 81 mA·h for the cells containing tetraglyme, PC, and F1S3M2 electrolytes, respectively. Since each anode was pre-charged to 100mA·h, these figures imply that approximately 80% of the original charge capacity was recovered in each case. This is a stark contrast to the high temperature experiments, none of which recovered more than 50% of their original charge capacity during discharge at 190 °C. Though the exact values of these recovery percentages depend on the defined voltage point at which the cycle ends (chosen to be 0.5 V for these tests), the relative trend between room- and high-temperature still holds.

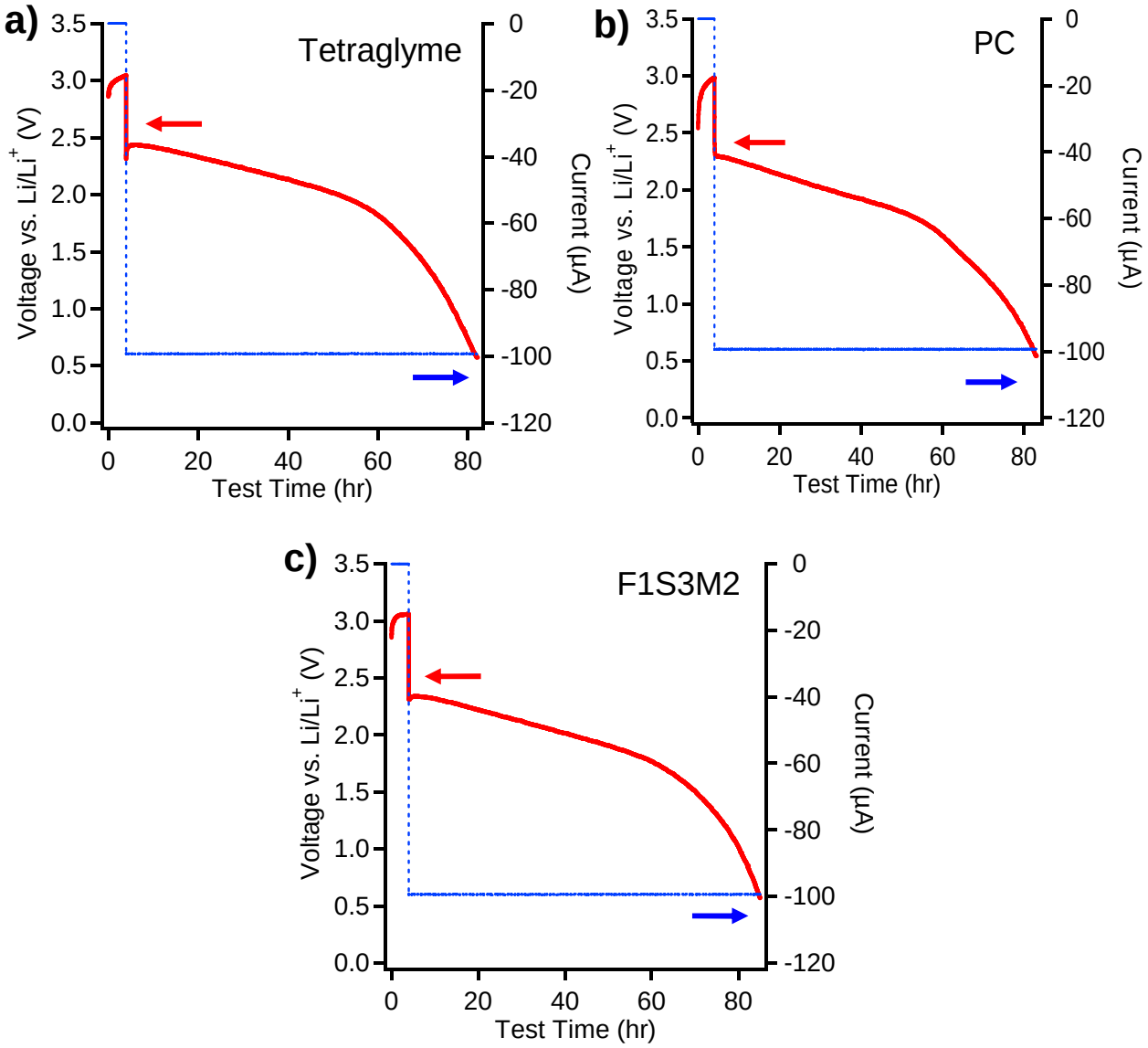

Figure 2.5. The 25 °C discharge curves for cells containing a pre-lithiated silicon (100) wafer chip and a CFx film electrode with an electrolyte made from LiBF4 and a) tetraglyme solvent, b) propylene carbonate solvent, and c) F1S3M2 solvent. Each figure shows the voltage (solid red curve, left axis) and current (dashed blue curve, right axis) profiles. All three cells survived discharge for over 75 hours.

2.4.2 Atmospheric-Sampling Mass Spectrometry

To investigate the high-temperature stability of the electrolytes alone and in contact with electrodes at high temperatures, atmospheric-sampling mass spectrometry was employed to monitor decomposition products present in the headspace above the electrolyte while varying the temperature. Figure 2.6 shows mass spectra for a tetraglyme/$LiBF_4$ electrolyte solution in contact with a CF_x electrode and with a Li-Si electrode identical to those used in the discharge tests described above. First, figure 2.6a shows data for the case where a CF_x film electrode was immersed in the electrolyte. A comparison of the mass spectra shows that there is no change in the mass spectrum as the temperature increases, even at the maximum of 190 °C. The largest peaks in the spectrum are due to argon, which is used as the purge gas in the cell, which displays four main peaks: ^{40}Ar appears at 40 m/z for the 1+ ion and 20 m/z for the 2+ ion, while ^{36}Ar also appears at 36 and 18 m/z for the 1+ and 2+ ions respectively. There are also small remnants of air, represented mainly by N_2^+ at 28 m/z and O_2^+ at 32 m/z as well as their 2+ forms at half of those m/z values. Because of the absence of new peaks with increasing temperature, we can conclude that the tetraglyme/$LiBF_4$ electrolyte is quite stable at temperatures as high as 190 °C even in the presence of the CF_x surface and that no gaseous products are given off in detectable amounts.

Figure 2.6b shows mass spectrometry data after a Li-Si sample was immersed in tetraglyme/$LiBF_4$ (1M) electrolyte. When heated to 190 °C the mass spectroscopy data show several small new peaks at 190 °C. The most immediately obvious are new features at 58 and 88 m/z, and closer examination of the low-m/z region shown in Figure 2.6c reveals that there are also new sets of peaks centered at 29 m/z and 45 m/z. By comparing with literature spectra from

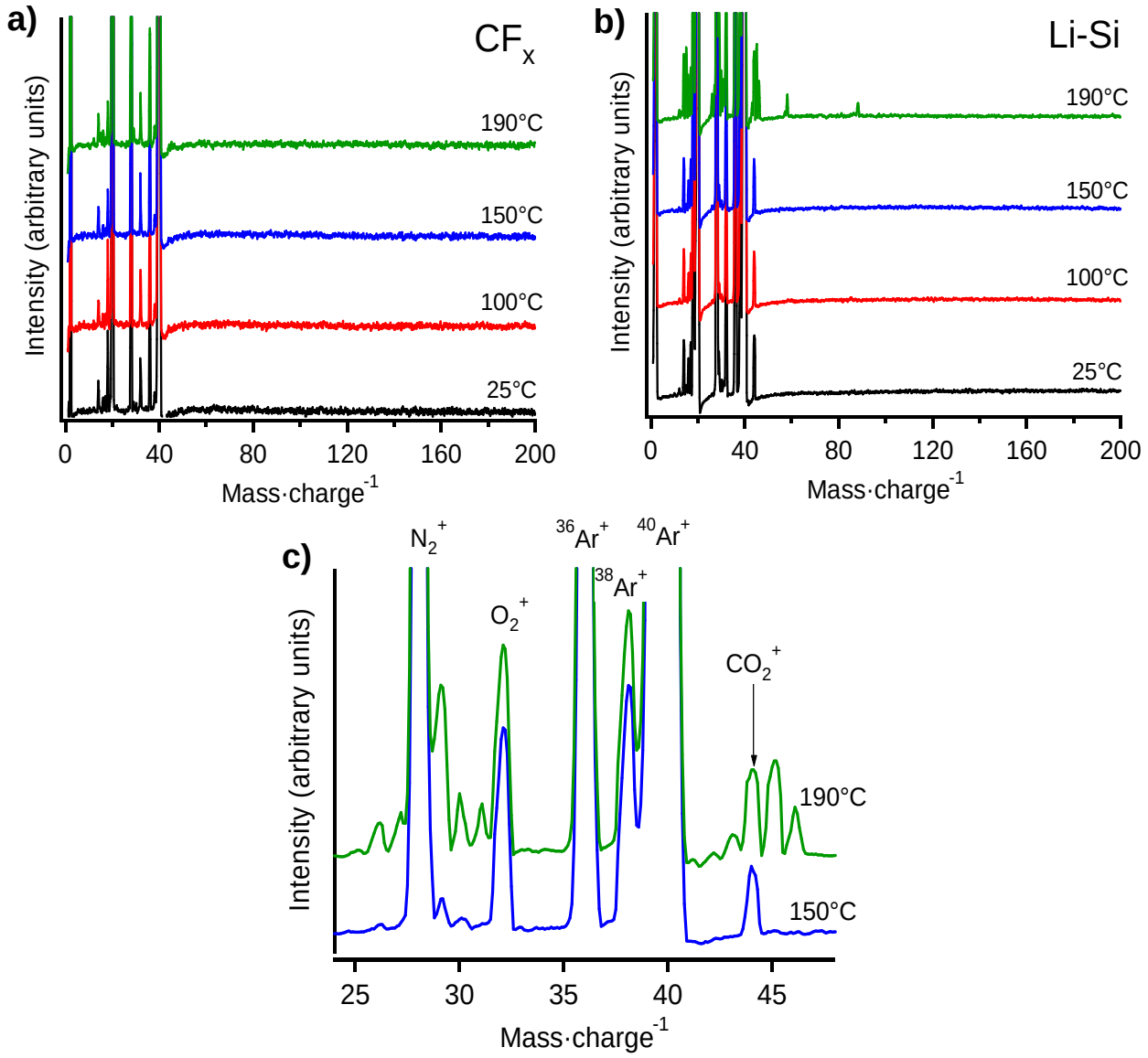

Figure 2.6. Atmospheric sampling mass spectrometry data for a tetraglyme/LiBF4 electrolyte in contact with a piece of a) CFx and b,c) Li-Si electrode at varying temperatures. The largest peaks (off scale) arise from the Ar purging gas and residual atmosphere. No significant change is seen even at 190 °C for the electrolyte in contact with a CFx film electrode, but several small peaks appear for the sample in contact with the lithiated silicon electrode (see detail in part c)

the NIST database, we find that the pattern of peaks is not a good match for tetraglyme[24], which would have its principal peak at m/z = 59 as well as a moderately strong peak at m/z = 103; neither of these is observed. Instead, the spectrum is a better match for 1,4-dioxane[24], which has large peaks at m/z = 58 and 88 and clusters around m/z = 29 and m/z=43. Since these peaks only appear when the electrolyte is in contact with Li-Si electrode and not when the electrolyte is in contact with CF_x, their presence shows that there must be a pathway for decomposition induced by the lithiated silicon.

Further thermal stability tests were also conducted with the other electrolytes used in high-temperature discharge tests. Figure 2.7 shows the atmospheric sampling mass spectrometry data for propylene carbonate/$LiBF_4$ (1M) salt in contact with a Li-Si or CF_x electrode. For both the CF_x electrode in Figure 2.7a and the Li-Si electrode in Figure 2.7b, there are no detectable signals aside from the atmospheric gases even at 190 °C. The absence of new peaks indicates that if there is any decomposition occurring in the PC electrolyte, it does not produce detectable gaseous byproducts in the cells, although solid or nonvolatile liquid products could still be formed.

Finally, Figure 2.8 shows the atmospheric sampling mass spectrometry data for the F1S3M2/$LiBF_4$ (1M) electrolyte tested in the same manner. In this case, the neat solvent displays several peaks indicating some thermal decomposition at 150 °C and above. Figures 2.8b and 2.8c respectively show that inclusion of a CF_x cathode or a Li-Si anode in the testing vial produced no change and we see the same decomposition as for the neat electrolyte. Closer examination reveals the largest decomposition peak appears at m/z = 81 m/z with smaller peaks at m/z = 58, 67, 77, 88, and 96 as well as clusters near m/z = 29 and 42. By comparison with literature

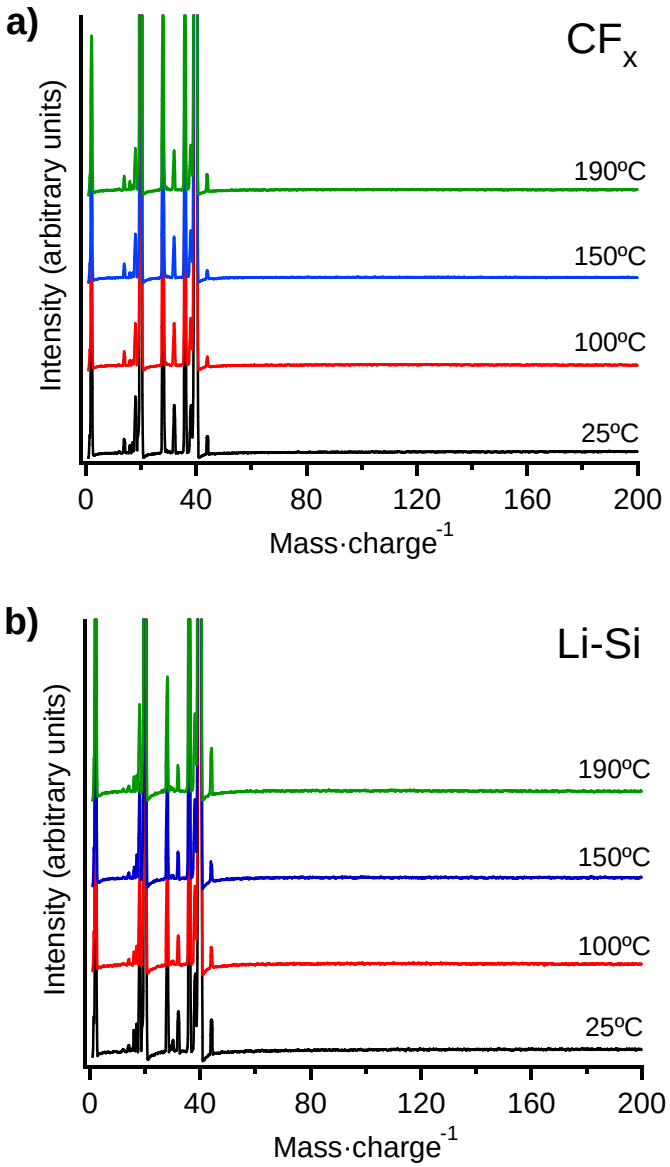

Figure 2.7. Atmospheric sampling mass spectrometry data for a propylene carbonate/LiBF4 electrolyte in contact with a piece of a) CFx and b) Li-Si electrode at varying temperatures. The largest peaks (off scale) arise from the Ar purging gas and residual atmosphere.

spectra[24], we attribute the peaks at m/z = 58 and 88 and the clusters near m/z = 29 and 42 to 1,4-dioxane, just as in the tetraglyme experiments. This assignment is reasonable since both tetraglyme and F1S3M2 contain similar glycol chains that presumably form 1,4-dioxane during decomposition. The other peaks at m/z = 67, 77, 81, and 96 are a good match for difluorodimethylsilane[24], which could result from F^- attack at the silicon atom of F1S3M2. Much like the case for tetraglyme, all the decomposition peaks are relatively small and do not represent catastrophic breakdown of the electrolyte.

2.4.3 Germanium Anode

To further demonstrate the versatility of the system, a germanium (100) wafer piece (Ga-doped, p-type, 0.02-0.03 Ω·cm) was lithiated in the same manner as the silicon samples in the experiments described above. The Li-Ge electrode was then removed from the precursor lithiation cell, put into a high-temperature cell with a CF_x film electrode and tetraglyme/$LiBF_4$ electrolyte. Figure 2.9 shows the discharge curve at 190 °C. The cell displays a flat plateau at approximately 2.5V as the cell discharges, and the cell survives for more than 1 day at 190 °C. The cell in figure 2.9 was able to discharge approximately 28% of the theoretical capacity of this anode-limited cell. These results demonstrate that lithiated germanium can also be an effective anode at high temperatures, and appears able to maintain its capacity even better than silicon in this environment.

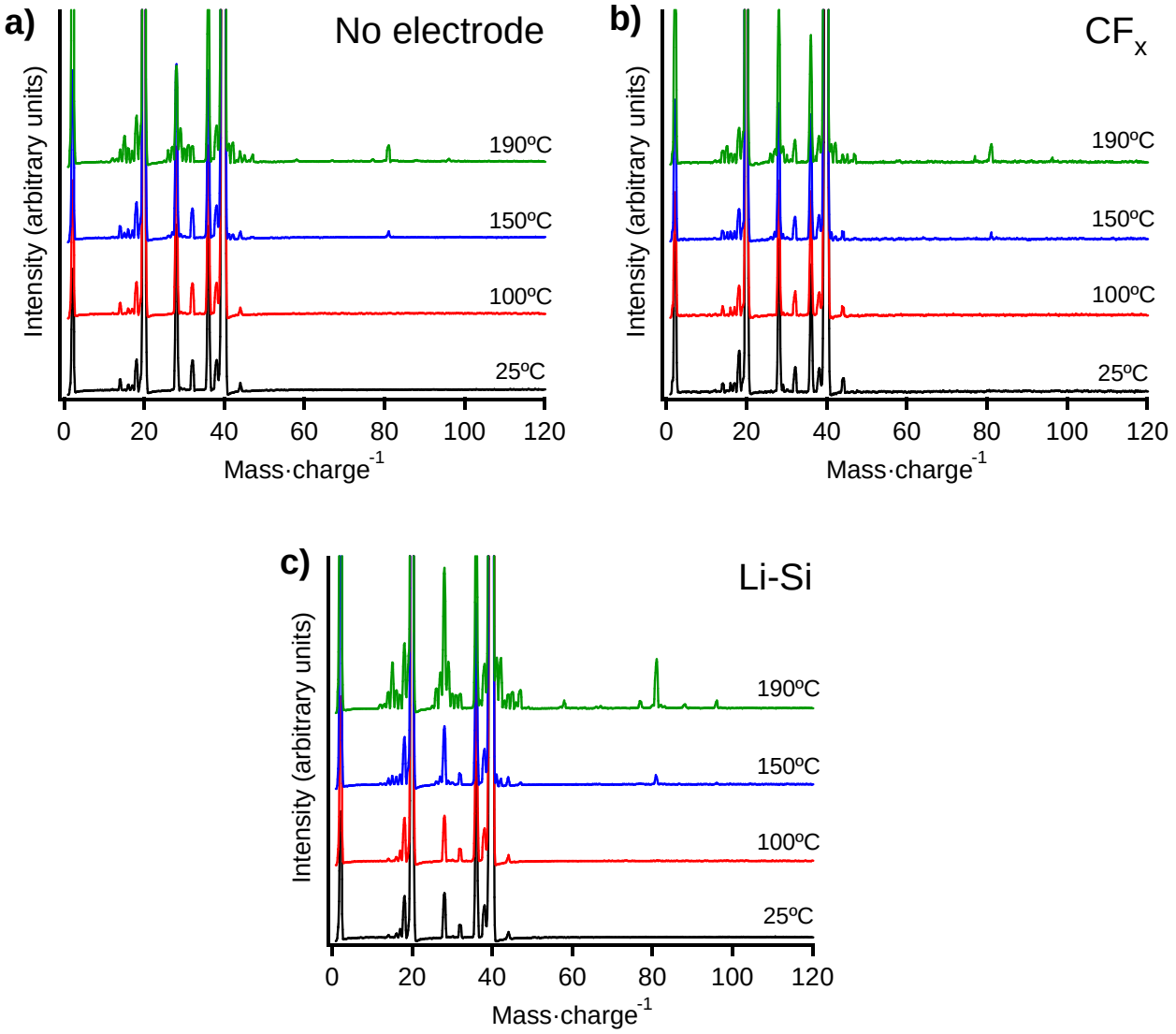

Figure 2.8. Atmospheric sampling mass spectrometry data at various temperatures for an F1S3M2/LiBF4 electrolyte in a) neat solution b) in contact with CFx electrode and c) in contact with Li-Si electrode. The largest peaks (off scale) arise from the Ar purging gas and residual atmosphere.

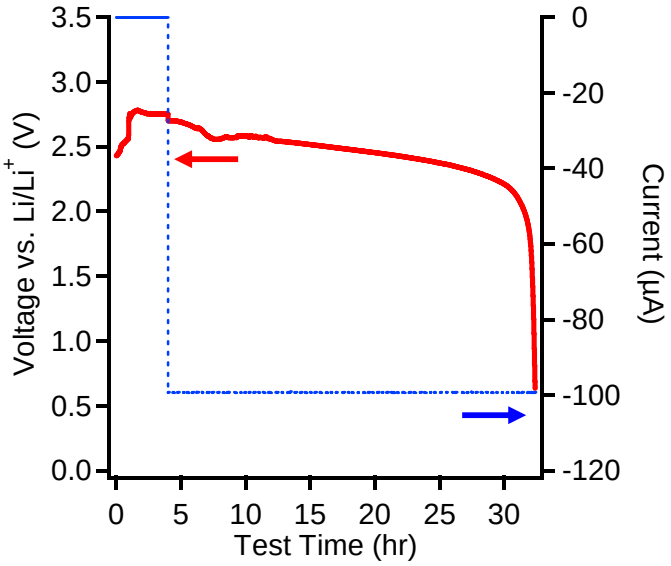

Figure 2.9. The discharge curve for a cell containing a pre-lithiated germanium (100) wafer chip and a CFx film electrode with tetraglyme/LiBF4 electrolyte, consisting of the voltage (solid red curve, left axis) and current (dashed blue curve, right axis) profiles. The rise at approximately 1h into the initial resting period occurs during the temperature increase from 25 to 190 °C.

2.5 Discussion

The experiments described above show that Li-Si anodes can be paired with CF_x cathodes to create primary lithium cells that can operate at very high temperatures in excess of the melting point of lithium. The cells are capable of operating using any of three different electrolyte solvents that are quite chemically distinct (one carbonate, one glyme chain, and one glyme-based organosilicon compound). Going beyond the successful discharging of the cells, two general observations are clear from the collection of data in this study. First, for all three electrolytes there is some lost some capacity at high temperature versus their room temperature performance, as seen by comparing Figures 2.3 and 2.5. Second, even though all three electrolytes perform identically at room temperature, when discharged at high temperature their performances are noticeably different between electrolytes, particularly in the case of F1S3M2 versus the other two solvents, PC and tetraglyme. We will discuss each of these two main observations in turn.

First we will consider the capacity loss seen in all electrolyte systems at high temperature. For all three electrolytes, the substantial decrease in Columbic efficiency from ~80% at room temperature to 10-40% (depending on solvent) observed at 190 °C shows that additional mechanism(s) for capacity loss are introduced at high temperatures. Furthermore, the reduced discharge capacity of the planar silicon cells at high temperature and the complete failure of silicon nanoparticle anodes at high temperature could both be explained by a loss of lithium from the silicon at higher temperatures. Evidence for this process is provided by the fact that for the tetraglyme electrolyte, decomposition to form 1,4-dioxane only occurs when the lithiated silicon anode is present, as seen in Figure 2.6. This proposed lithium loss from the

silicon is also consistent with work by Park and Lee showing that lithiated silicon particles of smaller size display more thermal decomposition (as monitored by differential scanning calorimetry) at lower onset temperatures than larger silicon particles in the presence of an ethylene carbonate/diethylene carbonate/$LiPF_6$ electrolyte[25]. They also found that higher degrees of lithiation in the silicon increased the amount of decomposition and caused a lower onset temperature of the decomposition, indicating that the lithium is a reactant in the decomposition reaction. In the temperature regime relevant for this work, Park and Lee attribute the main decomposition event they observe (near 140 °C) to thermal decomposition of the SEI layer.

Though Park and Lee use a different electrolyte from those in this test, if a similar process is occurring in our cells, SEI decomposition could lead to SEI components dissolving back into the electrolyte, re-exposing the surface of the lithiated silicon surface. This re-dissolution is sensible since the anode SEI is formed by reduction of electrolyte components and is therefore expected to be chemically quite similar to the electrolyte itself. Once the anode surface is exposed by SEI decomposition, new SEI can be formed since the lithiated silicon has not changed and thus should still be at an electrochemical potential low enough to reduce electrolyte components. In order to maintain charge balance, for each electron involved in reduction of an electrolyte component, a corresponding Li^+ cation must also leave the anode and either coordinate in the SEI or solvate in the electrolyte. In this manner, continual cycles of SEI formation and decomposition could considerably deplete the lithium in the anode.

To explain the behavior seen in the self-discharge experiments in Figure 2.4, where the more lithiated electrodes maintained their OCP for many hours while the less lithiated electrodes quickly lost OCP, we can consider the depth of lithiation of the silicon. Silicon samples that are

lithiated to a higher capacity will have lithium deeper into the Si lattice, and deeper lithium atoms will take longer to diffuse out of the silicon surface than shallower lithium atoms. Previous TEM studies have shown[26] that the lithiation front proceeds as a sharp traveling boundary during the electrochemical lithiation of a silicon wafer with a lithium metal counter electrode. Using this approximation, we estimate the lithiation depth for a typical silicon wafer sample as used in this study to be 14 μm for a 10 mA·h charge and 3.6 μm for a 2.5 mA·h charge. Diffusion of Li out from shallow lithiation depths at high temperature would explain the observed total failure of nanoparticle composite anodes, since the depth of lithiation in those particles is, at most, the radius of the particles, which is much less than 1 μm. Even for electrodes that are lithiated to sufficient depth to maintain a stable OCP at high temperature and discharge useful current, this process of lithium loss would explain why a significant fraction of the anode charge capacity is never retrieved during high temperature discharge. Furthermore, the loss must be mainly to the surface and/or electrolyte as opposed to deeper into the bulk of the silicon, since the nanoparticle electrodes do not have a bulk reservoir of unlithiated silicon. Finally, the observed loss of cell potential at approximately 45 hours into the self-discharge test for the PC-containing cell in section 4.1 is consistent with the PC-containing cell having the shortest discharge time in sections 3.1-3, providing further evidence of a connection between those experiments.

We can rationalize the high Coulombic efficiency obtained using a germanium anode (as compared to silicon) in two ways. First, the diffusivity of lithium in germanium is 400 times greater than in silicon[27], so lithium is expected to penetrate more deeply into the Ge lattice than it does into the Si during the pre-lithiation step. Following our working hypothesis that reduced Coulombic efficiency is due to lithium loss from near the surface, we would therefore expect a

higher efficiency for the more deeply lithiated germanium anode as compared to silicon. Second, the solubility of lithium in germanium is significantly higher than in silicon (as calculated by DFT)[28], supporting the hypothesis that the lithium is more unstable in the silicon anode at high temperature than it is in germanium. The lower stability of the Li-Si alloy could then lead to more reaction with the electrolyte for the Li-Si system and therefore decreased Coulombic efficiency compared to the Li-Ge system. At room temperature the lower thermodynamic stability of Li in Si (as compared to Ge) may be partially mitigated by larger kinetic barriers to Li diffusion in silicon (for a single Li^+ ion, 0.62 eV for Si versus 0.44eV for Ge, as calculated by DFT)[29], but at higher temperatures the thermodynamics of the system are more likely to dominate, favoring lithium stability in germanium as compared to silicon.

Next, we consider the superior high-temperature performance of the F1S3M2-based electrolyte as compared to the tetraglyme- and PC-based electrolytes. We may assume that the $LiBF_4$ salt plays only a secondary role in any decomposition processes since it is constant between all three systems. Therefore the primary actor in any decomposition must be the electrolyte solvent, though attack by BF_4^-, BF_3, or F^- may also participate in decomposition as PF_5 does in a different organosilicon electrolyte system[23]. As seen comparing Figure 2.8 with Figures 2.6 and 2.7, the decomposition of F1S3M2 at high temperatures is actually larger than that of either PC or tetraglyme. At first glance this high level of decomposition appears surprising considering that F1S3M2 produces the highest Coulombic efficiency in the high-temperature cell tests. Of course, because the peaks are small in the mass spectra (all are smaller than the residual O_2 that remains even after extensive purging) and the cells still function in the discharge experiments described above, it must be that any decomposition reactions for the

various electrolytes do not take place very rapidly; i.e. the decomposition clearly does not cause catastrophic cell failure. Nevertheless, it may be that the decomposition of the F1S3M2 electrolyte at high temperature is actually the key to its superior performance. In a series of accelerating-rate calorimetry experiments, Wang and Dahn found[30] that both lithiated silicon and lithiated graphite react with an alkyl carbonate-based electrolyte at high temperatures. In a detailed analysis, however, they discovered that a thicker layer of decomposition products is formed on the silicon surface as compared to the graphite surface, and that this thicker layer actually slows down further reaction with the electrolyte once it is formed. In our case, it may be it is the different electrolytes that provide the different breakdown performances that subsequently affect cell performance. By our mass spectrometry results (Figures 2.6-2.8), it is clear that F1S3M2 has the highest degree of breakdown at high temperature of the three electrolytes tested, and if F1S3M2 therefore forms the thickest surface decomposition layer, this could impede further lithium loss from the electrode and explain the higher Coulombic efficiency achieved for the F1S3M2 cell.

It is worth noting that this explanation leads to the conclusion that F1S3M2 occupies a "sweet spot" in terms of the extent of its breakdown. Certainly an electrolyte component (whether solvent, salt, or additive) that reacted too quickly with the lithiated silicon electrode at high temperature would most likely either form a very thick and high-impedance layer that reduced the ability of the cell to transport charge, or possibly even produce gaseous byproducts that would over-pressurize the cell. Conversely, an electrolyte that formed an insufficiently thick decomposition layer would presumably be subject to continuing lithium losses throughout cell operation. This suggests that the best cell performance should be obtained by finding the

electrolyte system that offers the right balance of decomposition and stability, very analogous to the need to form a high-performance SEI layer in room temperature cells that the traditional alkyl carbonate electrolytes fulfill so well.

2.6 Conclusion

This work demonstrates the feasibility of very high-temperature stable lithium-ion batteries, operating at temperatures above the melting point of lithium. The performance appears to depend on sufficient degree (that is, depth) of lithiation of the silicon anode material. Once sufficient lithiation is achieved, the cells are stable under discharge conditions for hours at a temperature above the melting point of lithium (180 °C), and in some cases (such as with the organosilicon electrolyte F1S3M2), they are stable under discharge for days. The cells are also stable at rest for at least several days at the same high temperatures. The cells are fully viable with any of several electrolyte solvents and there is promise for other alloyed anodes (such as lithiated Ge), though the choice of salt is currently limited to $LiBF_4$. Detailed experiments on the nature of the capacity loss at high temperature showed that the mechanism of loss is most likely decomposition or dissolution of the SEI layer at high temperature, which exposes the Li-Si electrode surface and allows for continual new SEI formation, which eventually depletes the cell capacity significantly. The organosilicon F1S3M2 electrolyte displayed the best performance, likely due to forming a decomposition layer on the lithiated silicon surface that, once formed, prevents further lithium loss from the anode. Despite the lost capacity seen at high temperature, the cells are still viable and with further refinement could enable applications such as a new generation of robotic systems for deep-earth exploration where the ambient temperature is extremely high.

2.7 References

(1) Winter, M.; Brodd, R. J. *Chemical Reviews,* **2004**, *104*, 4245.

(2) Tarascon, J.-M.; Armand, M. *Nature*, **2001**, *414*, 359.

(3) Goodenough, J. B.; Kim, Y. *Chemistry of Materials*, **2010**, *22*, 587.

(4) Scrosati, B.; Garche, J. *Journal of Power Sources*, **2010**, *195*, 2419.

(5) Xu, K. *Chemical Reviews*, **2004**, *104*, 4303.

(6) Laman, F. C.; Gee, M. A.; Denovan, J. *Journal of the Electrochemical Society*, **1993**, *140*, L51.

(7) Arora, P.; Zhang, Z. *Chemical Reviews*, **2004**, *104*, 4419.

(8) Kurita, T.; Lu, J.; Yaegashi, M.; Yamada, Y.; Nishimura, S.; Tanaka, T.; Uzumaki, T.; Yamada, A. *Journal of Power Sources*, **2012**, *214*, 166.

(9) Watarai, A.; Kubota, K.; Yamagata, M.; Goto, T.; Nohira, T.; Hagiwara, R.; Ui, K.; Kumagai, N. *Journal of Power Sources*, **2008**, *183*, 724.

(10) Bodenes, L.; Naturel, R.; Martinez, H.; Dedryvère, R.; Menetrier, M.; Croguennec, L.; Pérès, J.-P.; Tessier, C.; Fischer, F. *Journal of Power Sources*, **2013**, *236*, 265.

(11) Reddy, T. B.; Linden, D. *Linden's Handbook of Batteries*, 4th ed. McGraw-Hill Companies, New York, **2011**.

(12) Endo, M.; Momose, T.; Touhara, H.; Watanabe, N. *Journal of Power Sources*, **1987**, *20*, 99.

(13) Hamwi, A.; Daoud, M.; Cousseins, J. C.; Yazami, R. *Journal of Power Sources*, **1989**, *27*, 81.

(14) Muñoz-Rojas, D.; Leriche, J.-B.; Delacourt, C.; Poizot, P.; Palacín, M. R.; Tarascon, J.-M. *Electrochemistry Communications,* **2006**, *9*, 708.

(15) Obrovac, M. N.; Christensen, L. *Electrochem. Solid-State Letters,* **2004**, *7*, A93.

(16) Okamoto, H. *Journal of Phase Equilibrium and Diffusion,* **2009**, *30*, 118.

(17) Jung, S. C.; Han, Y.-K. *Physical Chemistry Chemical Physics,* **2011**, *13*, 21282.

(18) Fenton, D. E.; Parker, J. M.; Wright, P. V. *Polymer,* **1973**, *14*, 589.

(19) Rossi, N. A. A.; West, R. *Polymer International* **2009**, *58*, 267.

(20) Zhang, L.; Zhang, Z.; Harring, S.; Straughan, M.; Butorac, R.; Chen, Z.; Lyons, L.; Amine, K.; West, R. *Journal of Materials Chemistry,* **2008**, *18*, 3713.

(21) Amine, K.; Wang, Q.; Vissers, D. R.; Zhang, Z.; Rossi, N. A. A.; West, R. *Electrochemistry Communications,* **2006**, *8*, 429.

(22) Corey, E. J.; Venkateswarlu, A. *Journal of the American Chemical Society,* **1972**, *94*, 6190.

(23) Chen, X.; Usrey, M.; Pena-Hueso, A.; West, R.; Hamers, R. J. *Journal of Power Sources*, **2013**, *241*, 311.

(24) Stein, S. E., ed. *Mass Spectra*, NIST Chemistry WebBook. NIST Standard Reference Database Number 69, Eds. P. J. Lindstrom and W. G. Mallard, National Institute of Standards and Technology, Gaithersburg, MD, 20899 (retrieved April 29, 2013).

(25) Park, Y.-S.; Lee, S.-M. *Bulletin of the Korean Chemical Society,* **2011**, *32*, 145.

(26) Chon, M. J.; Sethuraman, V. A.; McCormick, A.; Srinivasan, V.; Guduru, P. R. *Physical Review Letters,* **2011**, *107*, 045503.

(27) Graetz, J.; Ahn, C. C.; Yazami, R.; Fultz, B. *Journal of the Electrochemical Society*, **2004**, *151*, A698.

(28) Chan, M. K. Y.; Long, B. R.; Gewirth, A. A.; Greeley, J. P. *Journal of Physical Chemistry Letters*, **2011**, *2*, 3092.

(29) Chou, C.-Y.; Kim, H.; Hwang, G. S. *Journal of Physical Chemistry C*, **2011**, *115*, 20018.

(30) Wang, Y.; Dahn, J. R. *Journal of the Electrochemical Society*, **2006**, *153*, A21188.

Chapter 3

Surface Chemistry of SEI Layer Formation on Single-Crystal Si (100) Using Organosilicon Electrolytes for Next-Generation Lithium-Ion Batteries

3.1 Introduction

Lithium-ion batteries (LIBs) are one of the most important technological advances of the past few decades, enabling everything from smartphones and laptops to electric cars[1]. LIBs were originally proposed by Armand[2] as well as Scrosati and co-workers[3], and credit is generally given to Goodenough and co-workers[4] for demonstrating key parts of the working system (particularly cathode materials). Lithium-ion batteries have been so successful due to their very high energy density and relatively long cycle lives relative to other secondary (rechargeable) battery chemistries[5]. Nevertheless, gains made in recent years to cell efficiencies and capacities have been mostly a result of engineering efforts[1]. Fundamental materials advances will be necessary to make truly groundbreaking advances in LIB capacity with the goal of enabling electric cars that can rival gasoline-powered vehicles in range and reliability. Currently, in order to power an electric car with the same range as a tank of gasoline provides, the batteries necessary would weigh so much that the car would be impractically heavy.

Lithium-ion batteries consist of three principal components: the anode, the cathode, and the electrolyte. By definition, neither electrode in an LIB is made of lithium metal, but instead both are intercalation compounds that can accept lithium cations into their existing lattices. Lithium itself is therefore not oxidized or reduced in a lithium-ion battery, instead remaining as

Li^+; it is the active intercalation material in the anode and cathode that undergo oxidation and reduction. The most commonly used anode material in current generation LIBs is graphite, while cathode materials are generally some lithium-containing metal oxide, most commonly $LiCoO_2$. The capacity of a given cell is determined by the amounts of these active materials present. If we seek a battery with a higher capacity (or, equivalently, a battery of equal capacity but lighter weight), replacement of one or both of the active materials is the most attractive option.

If we seek to improve the capacity of the anode material, we must find a replacement for graphite. Graphite forms LiC_6 in its most lithiated phase[6], which equates to an intrinsic lithium intercalation capacity of 372 mAh/g. Graphite has also been successful in commercial LIBs due to its formation of a very stable solid-electrolyte interphase (SEI) in certain electrolytes. This layer forms on the first charge of the battery and subsequently protects the graphite surface and electrolyte from further decomposition reactions at the very reducing potentials at the anode surface. Nevertheless, graphite's intrinsic capacity is relatively low compared to other materials such as silicon, which has a capacity of approximately 3580 mAh/g for $Li_{15}Si_4$, the most lithiated phase produced at room temperature[7]. This 10-fold increase in capacity means that silicon offers exceptional promise for the next generation of lithium-ion batteries. Silicon is also non-toxic and abundant in the earth's crust, and a large silicon processing industry already exists. Unfortunately, silicon's greatest advantage is also its main disadvantage: in transforming from pure Si to highly lithiated phases such as $Li_{15}Si_4$, the silicon can undergo a volume expansion of as much as 270%[8]. This large volume chance causes self-pulverization of the electrode active material (which is often in the form of micro- or nanoparticles) and loss of electrical contact, leading to severe capacity fade as the cell cycles[8,9].

Though the self-pulverization of silicon anode materials presents a large challenge, significant improvements can be made via nanostructuring the silicon active material[10]. Various groups have used silicon nanowires[11], nanospheres[12], nanoplatelets[13], and even hollow nanoshells[14] to obtain better cycling performance than with larger (microscale or bulk) silicon material. It appears that in many cases there is a critical length for nanoscaled silicon below which the structure will not fracture; for example, for nanospheres it is approximately 150 nm in diameter[12] . For amorphous silicon the dimension appears to be significantly larger, for example 870 nm in amorphous Si nanospheres[15]. The nanoscaling approach appears to solve the inherent pulverization problem of silicon itself, but another challenge remains: that of the accommodation of the volume expansion by the silicon SEI layer, electrode binder, and other materials which may be present in the vicinity of the silicon active material itself[16]. Thus, in addition to the self-passivating and electrochemically stable properties expected from SEI layers in current-generation batteries, electrolytes for next-generation LIBs with silicon anodes must also form mechanically compliant SEI layers.

Another area of desired improvement for lithium-ion batteries is the safety of the electrolyte. Though incidents of failure are relatively rare, current-generation batteries employ organic carbonates as their electrolyte solvents[17]. These compounds are quite flammable, and many have flash points near room temperature. This presents an especially severe problem since one of the failure modes of LIBs involves lithium dendrite formation across the cell, creating an electrical short. Once a short is created, large amounts of current can flow through a relatively small area (particularly if the short is a single dendrite), causing large heat buildup and a possible fire. Next-generation batteries may employ less flammable compounds if suitable electrolyte

solvents can be identified. Of course, any new compounds must also possess the Li^+ conductivity and electrochemical stability that make the organic carbonates so successful in LIBs. One class of compounds that holds great promise is the family of organosilicon glyme-based solvents[18,19]. These compounds have much higher flash points and thermal stabilities than the organic carbonate-based electrolytes currently in use, and can offer nearly equal performance characteristics as well[19,20]. In some cases the electrochemical stability window is even greater than that of a typical carbonate electrolyte[20].

In this study we investigate the surface chemistry of the SEI formation on silicon anodes by two different organosilicon compounds, shown in Figure 3.1 and designated 1NM2 and 1S3M2. A close analogue to the organosilicon compound designated 1NM3 studied previously[21], 1NM2 is an example of an organosilicon compound with an Si-O bond that was found to be a site vulnerable to attack[20] by species deriving from the common electrolyte salt $LiPF_6$. 1S3M2, on the other hand, is identical to 1NM2 except that it possesses no such Si-O bond, instead having a propyl spacer present between the Si atom and the first O atom of the glyme chain. 1S3M2 is therefore expected to offer even greater chemical and thermal stability due to the removal of the Si-O attack site. For ease of interpretation, the Si anodes investigated in this study were single-crystal wafer samples that were boron-doped to a very high conductivity. These samples had very well-defined (100) surfaces exposed and no binder or conductive additive (i.e. carbon black) that would complicate the analysis of the SEI formation.

a)

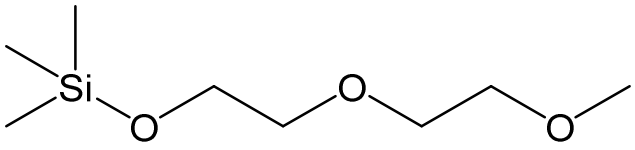

b)

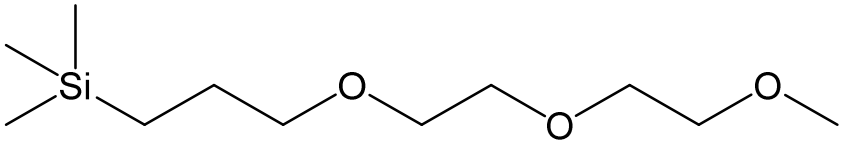

Figure 3.1. Structures of the two organosilicon compounds used in this study, **a)** (2-(2-methoxyethoxy)ethoxy)trimethylsilane (1NM2) and **b)** (3-(2-(2-methoxyethoxy)ethoxy)-propyl)trimethylsilane (1S3M2).

3.2 Experimental Methods

Single-crystal silicon (100) wafers (B-doped, < 0.004 Ω·cm, Addison Engineering) were cut into ~1 cm^2 squares to fit inside the coin cells, and then cleaned by ozone via exposure to a low-pressure Hg lamp for a minimum of 4 hours. After cleaning, Si wafer samples were stored in an argon glove box until use. In order to investigate the SEI formation on silicon single-crystal anodes, anode half-cells were constructed in type 2032 coin cells (Hohsen). Figure 3.2 shows a schematic of the cell assembly process, which was always conducted entirely in an argon glove box. Briefly, the cleaned Si wafer samples were placed into a coin cell bottom, and then covered with 60 μL of electrolyte. Electrolytes consisted of either 1NM2 or 1S3M2 with 1M $LiPF_6$ salt (all obtained from Silatronix). A Celgard 2500 separator was then applied to the wet Si surface, followed by another 20 μL of electrolyte on top of the separator. A Li foil counter electrode (Rockford Lithium, 0.008" thickness) was added next, followed by the rest of the components to complete the cell. The cells were then crimped in a hydraulic press (Hohsen) to seal them and then removed from the glove box to normal atmosphere for electrochemical testing.

All electrochemical tests were conducted on an Arbin Instruments MSTAT 12-channel battery tester. Typically, cells were charged at a constant current of 150 μA until reaching a specific voltage (most commonly, 200 or 50 mV) and then held at that potential for a pre-set amount of time. The amount of hold time was varied to probe the time-dependent SEI formation. Though the silicon SEI remains much less studied, the SEI formation on graphite is known to be strongly voltage-dependent[22], and it has also been found that the SEI growth is strongly time-dependent and relatively independent of the charge rate[23]. The constant current of 150 μA was

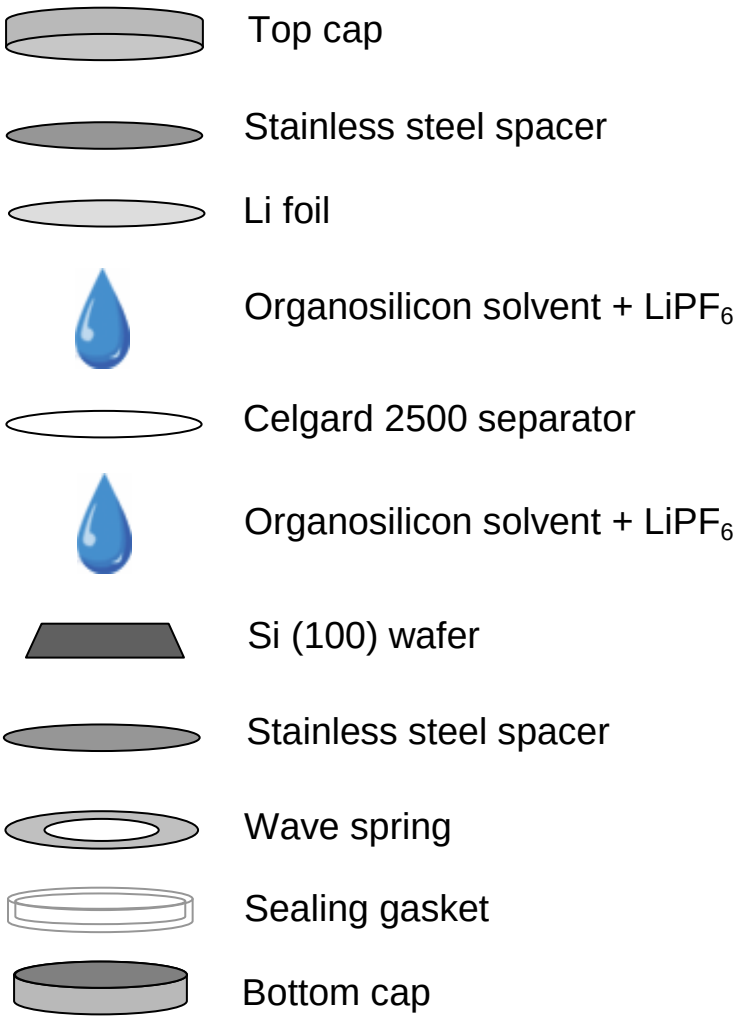

Figure 3.2. A schematic of a typical 2032 coin cell constructed for this study. This anode half-cell consists of a single-crystal silicon (100) wafer electrode with Li foil counter electrode. The electrolyte was added on both sides of the Celgard 2500 separator.

chosen to reach the hold potential in a relatively short amount of time (typically ~2 minutes) so that most of the testing time was spent at precisely the hold potential.

After completion of the electrochemical testing, cells were transported back into the argon glove box and disassembled. The Si electrodes were extracted, rinsed with glyme (Aldrich, anhydrous, 99.5%), dried by blowing with argon, and transported in a sealed container with argon atmosphere to the X-ray photoelectron spectrometer (XPS) or scanning electron microscope (SEM) for analysis. Only a brief (~30 sec) exposure to the atmosphere was required for loading the samples into either the SEM or the XPS. SEM analysis was conducted on a LEO Supra 55 VP field-emission instrument. XPS analysis was conducted in an ultra-high vacuum environment using a monochromated Al K-α source and 16-channel detector attached to a hemispherical analyzer. All spectra were taken using a 45° take-off angle. Data were analyzed by fitting the resulting spectra to Voigt functions with a polynomial baseline and correcting the resulting peak areas by dividing by the atomic sensitivity factors[24] (0.296 for C(1s), 1.0 for F(1s), 0.025 for Li(1s), 0.711 for O(1s), 0.412 for P(2p), and 0.283 for Si(2p)). All spectra were shifted so that the lowest-binding energy carbon (1s) peak, representing the adventitious carbon present on all samples, had a maximum at 284.8 eV.

3.3 Results

3.3.1 Electrochemical Lithiation

Figure 3.3 shows a charging plot for a typical half-cell containing a silicon electrode and Li foil counter electrode. The initial cell open-circuit potential is approximately 2.6 V (values

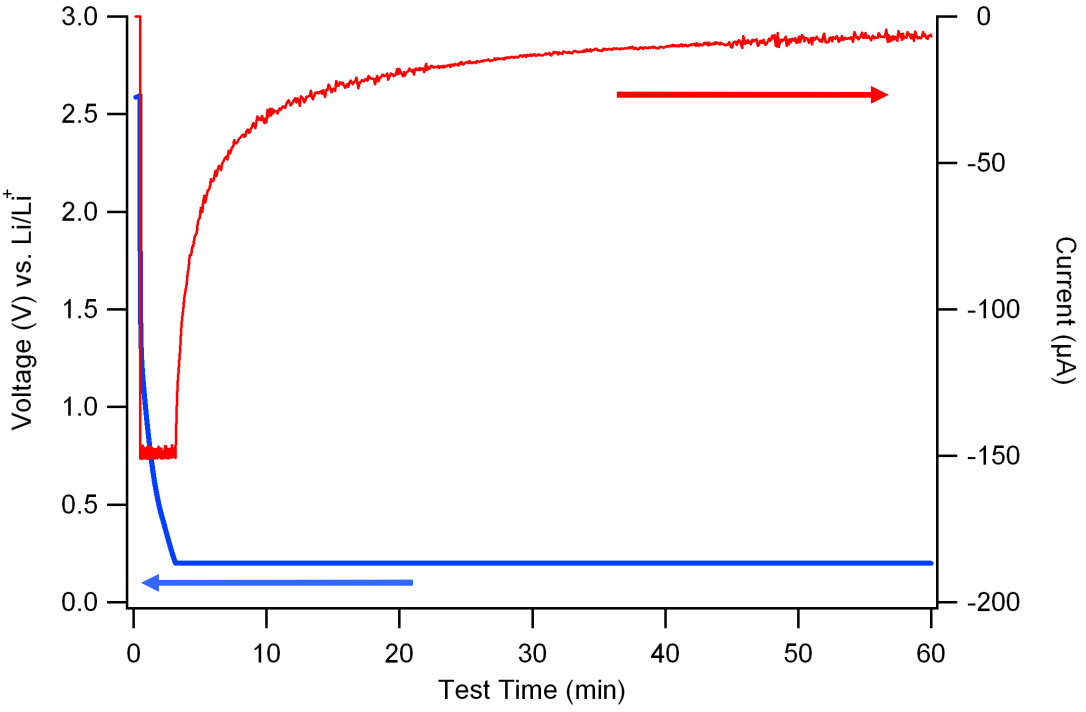

Figure 3.3. A typical charging curve for a silicon electrode half-cell with Li foil counter electrode, in this case containing 1NM2 electrolyte and charged to 200 mV. The cell takes approximately 3 minutes to reach 200 mV at a constant current of 150 µA. Once 200 mV is reached, the cell holds at that potential, requiring continually decreasing current to do so as time proceeds.

ranging from 2.5 V to 3.0V were common for this type of cell). At the beginning of the charge step, the current (red curve) is initially set to a constant value of 150 μA and the potential (blue curve) begins to decrease from its open-circuit value. After approximately 3 minutes, the potential reaches 200 mV, which was the desired potential for this particular cell. At this point the voltage holds at 200 mV for the remainder of the test, while the current begins to decrease. For this step the current value is set to whatever value is necessary to hold the potential at 200 mV, which requires a decreasing current as the charge proceeds. In this case, the cell continued to charge for a total of 4 hours, but only the first 60 minutes are shown for clarity in the initial few minutes. Though a large variety of cells were constructed with varying hold potentials, charge times, and electrolyte compositions, the essential features of the plot in Figure 3.3 were consistent between all cells.

3.3.2 Scanning Electron Microscopy

Figure 3.4 shows scanning electron microscope images of the SEI layer formed on single-crystal Si. In Figure 3.4a, we see the SEI formed by the 1NM2 + $LiPF_6$ electrolyte, which appears to consist of many spherical structures on the surface that have begun to meld. These structures may begin at crystal defects on the surface and grow over time until they merge with one another. In contrast, Figure 3.4b shows the SEI formed by the 1S3M2 + $LiPF_6$ electrolyte. Though qualitatively similar in the appearance of the spherical structures on the surface, the spheres are much more sparsely placed on the surface. For these images, both electrodes were held at 50 mV versus their Li foil counter electrodes, and an equal amount of total charge was allowed to flow for both, though this took ~30 min for the 1NM2 cell and ~ 4 hr for the 1S3M2 cell. The fact that the structures on the electrode from the 1S3M2 cell appear less densely packed

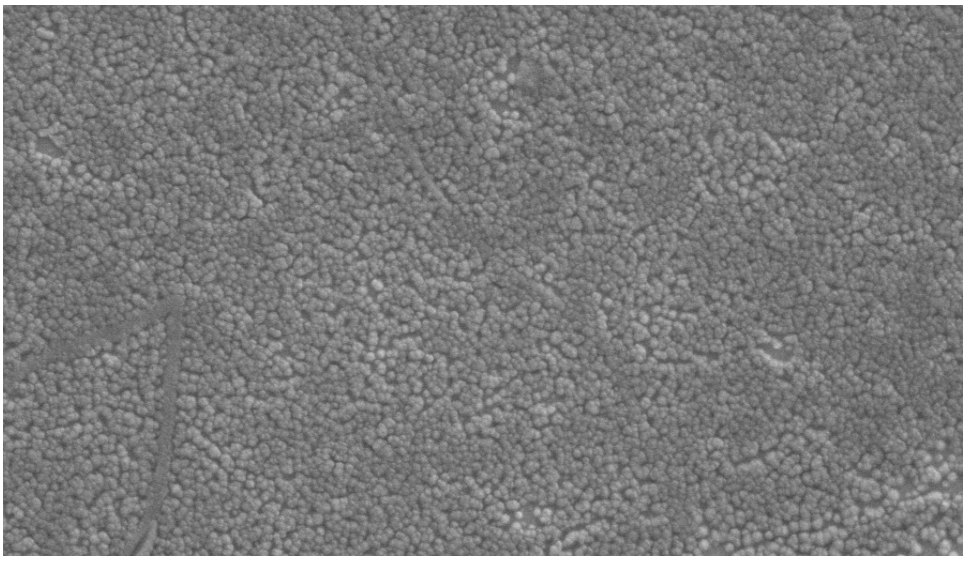

b)

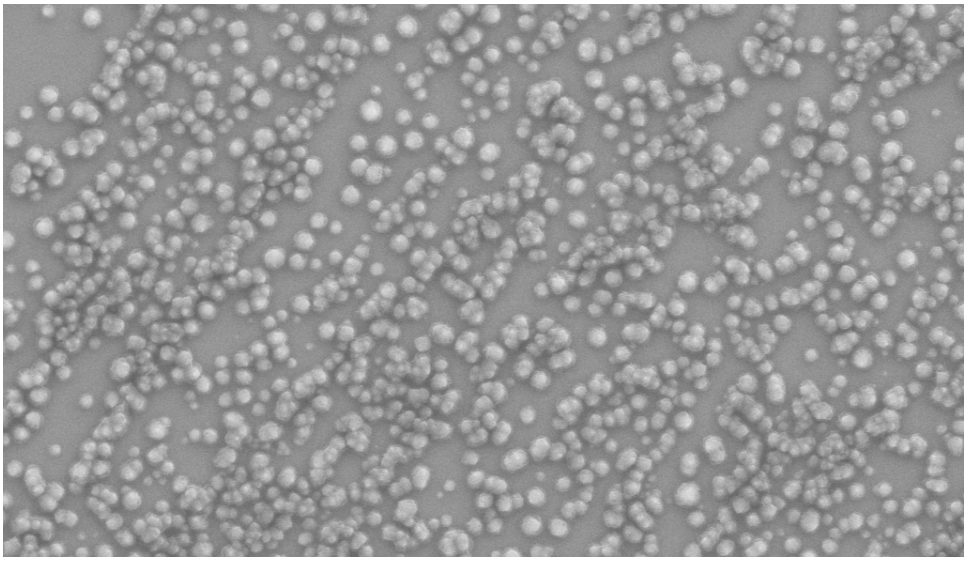

Figure 3.4. Scanning electron microscope images of the SEI layer formed on silicon by **a)** 1NM2 + $LiPF_6$ electrolyte and **b)** 1S3M2 + $LiPF_6$ electrolyte. Both samples were held at 50 mV until reaching the same total capacity. An accelerating voltage of 5kV and a 14mm working distance were used.

and perhaps slightly larger may indicate that SEI formation is more easily initiated for 1NM2 than for 1S3M2.

3.3.3 X-ray Photoelectron Spectroscopy

Figure 3.5 shows high-resolution XPS spectra for a Si (100) wafer electrode charged to 50 mV and held at that potential for 4 hours in a cell containing 1NM2 + $LiPF_6$ (1M) electrolyte and a Li foil counter electrode. Other experiments (*vide infra*) indicated that this time and voltage were sufficient to produce what can be considered the steady-state SEI, which is no longer changing within the sampling depth of the XPS measurement (~5 nm). Spectra for six different elemental regions are shown. Figure 3.5a shows the carbon (1s) region of the spectrum, which displays three constituent peaks. The lowest-binding energy peak, at 284.8 eV, is due to adventitious carbon contamination that appears on all surfaces and is not of significant interest. The middle peak, generally near 286.5 eV, is consistent with lightly oxidized carbons such as those in the ether groups of a glycol chain[25]. The highest-binding energy peak, generally near 289.5 eV, could be due to either highly oxidized carbons such as those in a carboxylic acid or ester group[26], or lightly fluorinated carbons such as -CHF- groups[27]. Figure 3.5b shows the fluorine (1s) region of the spectrum, which displays two components at 685 and 687.5 eV. These could be due to species such as $LiPF_6$ or LiF which have been previously observed in other studies of SEI layers[22]. Figure 3.5c shows the lithium (1s) region of the XPS spectrum, which appears to be composed of two components at very similar binding energies. In this case the fitting routine does not necessarily produce a unique result, and since lithium is nearly always present in a Li^+ oxidation state, the binding energy measured via XPS is not expected to change

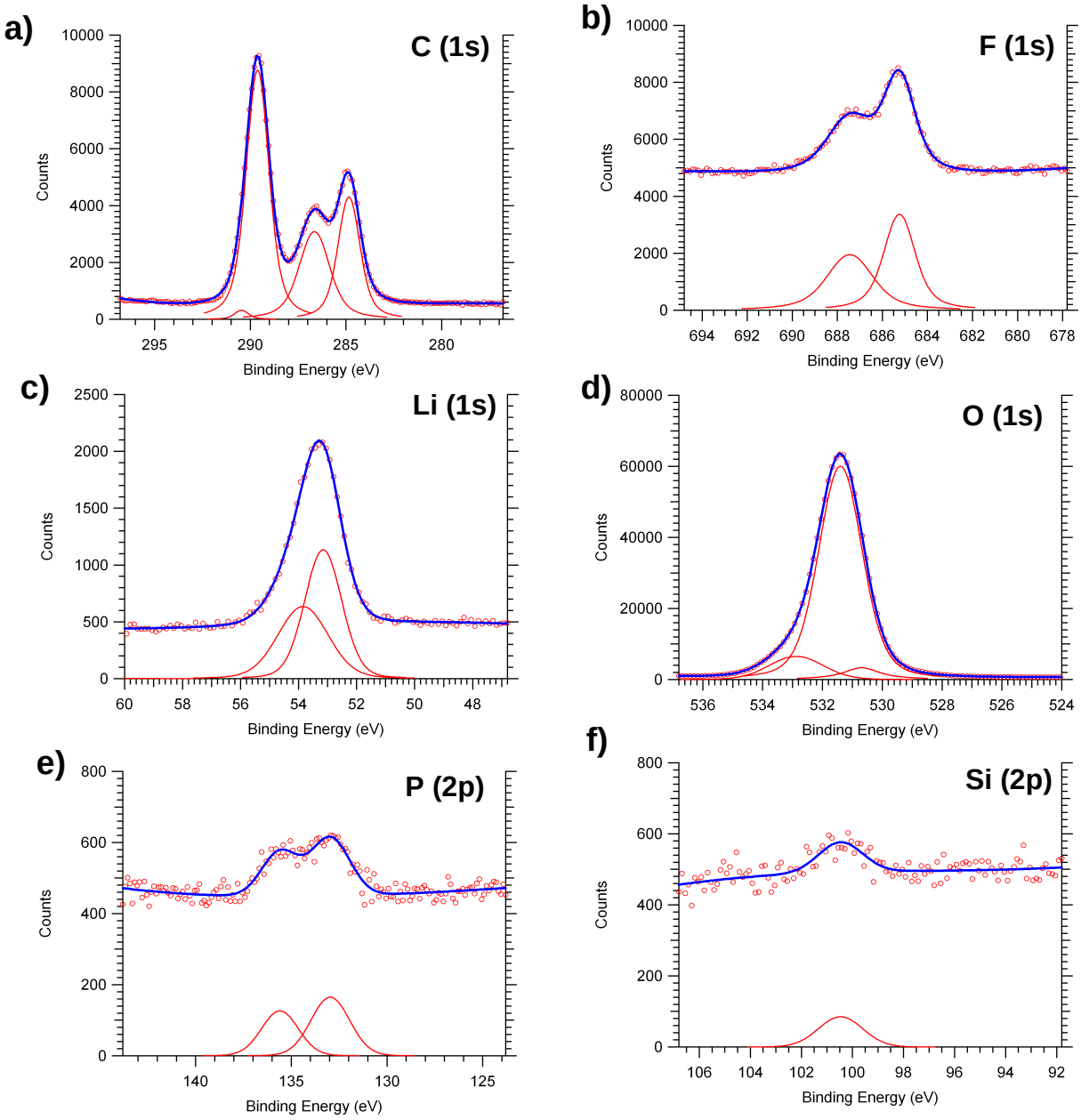

Figure 3.5. High-resolution XPS spectra of a Si (100) wafer electrode extracted from a cell containing 1NM2/$LiPF_6$ (1M) electrolyte that was charged to 50 mV and held at that potential for 4 hours. Experiments conducted at other time points indicated that the spectra above represent the "steady-state" SEI that is no longer changing with time, at least in the sampling depth of the XPS technique.

significantly even for very different Li-containing compounds. Figure 3.5d shows the oxygen (1s) region of the spectrum, and displays one very large feature at 531.5 eV and two smaller ones at 530.5 and 533 eV. Figure 3.5e shows the phosphorus (2p) region, which displays two small features at 133 and 136 eV. Finally, Figure 3.5f shows the silicon (2p) region, which shows only a very small signal at approximately 100.5 eV. This is notable since the substrate is the silicon electrode, indicating that a thick enough layer has formed on the surface of the electrode to almost completely attenuate the signal from beneath the SEI layer.

Figure 3.6 shows XPS data from a Si (100) wafer electrode charged in conditions identical to the electrode detailed in Figure 3.5 but with a 1S3M2 + $LiPF_6$ electrolyte instead of a 1NM2-based electrolyte. As before, other time and voltage experiments indicated that this time and voltage were sufficient to produce the steady-state SEI. Qualitatively, the elemental regions in Figure 3.6 look very similar to those in Figure 3.5. This is not too surprising, as the samples differ only in the electrolyte solvent to which they were exposed, and 1NM2 and 1S3M2 are quite similar structurally as shown in Figure 3.1. Despite the similarities, Figure 3.6f does show one notable difference, in that significantly more silicon appears than seen in the equivalent Figure 3.5f. This relatively lower attenuation of the underlying Si peak indicates that the layer that forms on top of the silicon electrode in the 1NM2 cell must be thicker than the layer that forms in the 1S3M2 cell.

In order to examine the progress of SEI formation, more cells identical in construction to those described above were built and subsequently charged at different voltages and for different amounts of time. In order to provide some focus to the rather large data set that resulted, only the carbon (1s) region is considered for the next section. Figure 3.7 shows XPS results of the carbon

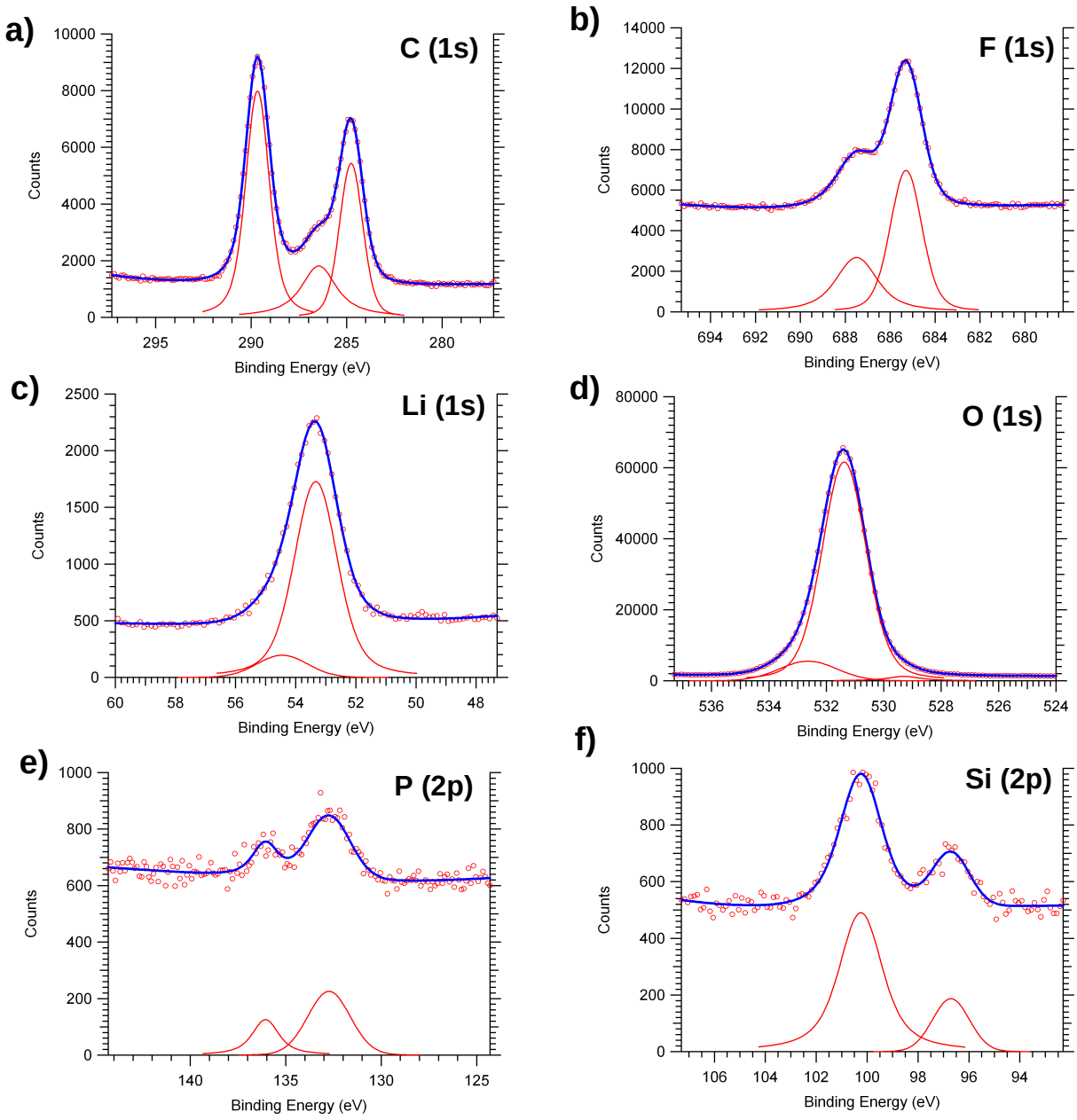

Figure 3.6. High-resolution XPS spectra of a Si (100) wafer electrode extracted from a cell containing 1S3M2/$LiPF_6$ (1M) electrolyte that was charged to 50 mV and held at that potential for 4 hours. Experiments conducted at other time points indicated that the spectra above represent the "steady-state" SEI that is no longer changing with time, at least in the sampling depth of the XPS technique.

(1s) region of the spectrum for samples charged in cells containing the 1NM2 + $LiPF_6$ electrolyte. In the left column, samples held at 200 mV for 1, 2, and 4 hours are shown. At this potential we expect only minimal lithiation of the silicon to occur[28], so it provides a way to probe only the initial SEI formation. The three constituent features described previously (adventitious carbon at 284.4 eV, glycol-like carbon at 286.5 eV, and highly oxidized carbon at 289.5 eV) are visible in the spectra for all three time steps. In general, only the area of the adventitious carbon peak changes significantly as the hold time is varied; whatever surface species are formed at 200mV appear to remain relatively unchanged over the course of the studies.

The right-hand column of Figure 3.7 shows similar carbon (1s) spectra, for cells that have been charged to and held at 50mV. At this potential, significant lithiation of the silicon is expected to occur[28] as well as continuing SEI formation. As before, we see three main features in the carbon (1s) region. Also as before, the features do not change significantly from 1 to 2 to 4 hours of charge time, indicating that whatever surface species appear in the first hour do not change significantly after that point. The most notable difference between these spectra and those in the left column is that the peak at highest binding energy (289.5 eV) is much larger in relative intensity. This increase in C(1s) intensity at binding energies higher that that of adventitious carbon demonstrates clear formation of a significant SEI layer[29,30].

In a parallel series of studies, similar experiments were conducted using 1S3M2 + $LiPF_6$ (1M) electrolyte and time steps of 2, 4, and 8 hours. The times used in these experiments were longer than those discussed above since the conductivity of 1S3M2 is lower than that of 1NM2 and therefore less current flows when a 1S3M2-containing cell is held at a given voltage than would flow for an equivalent cell containing 1NM2. In the left column of Figure 3.8 we see the

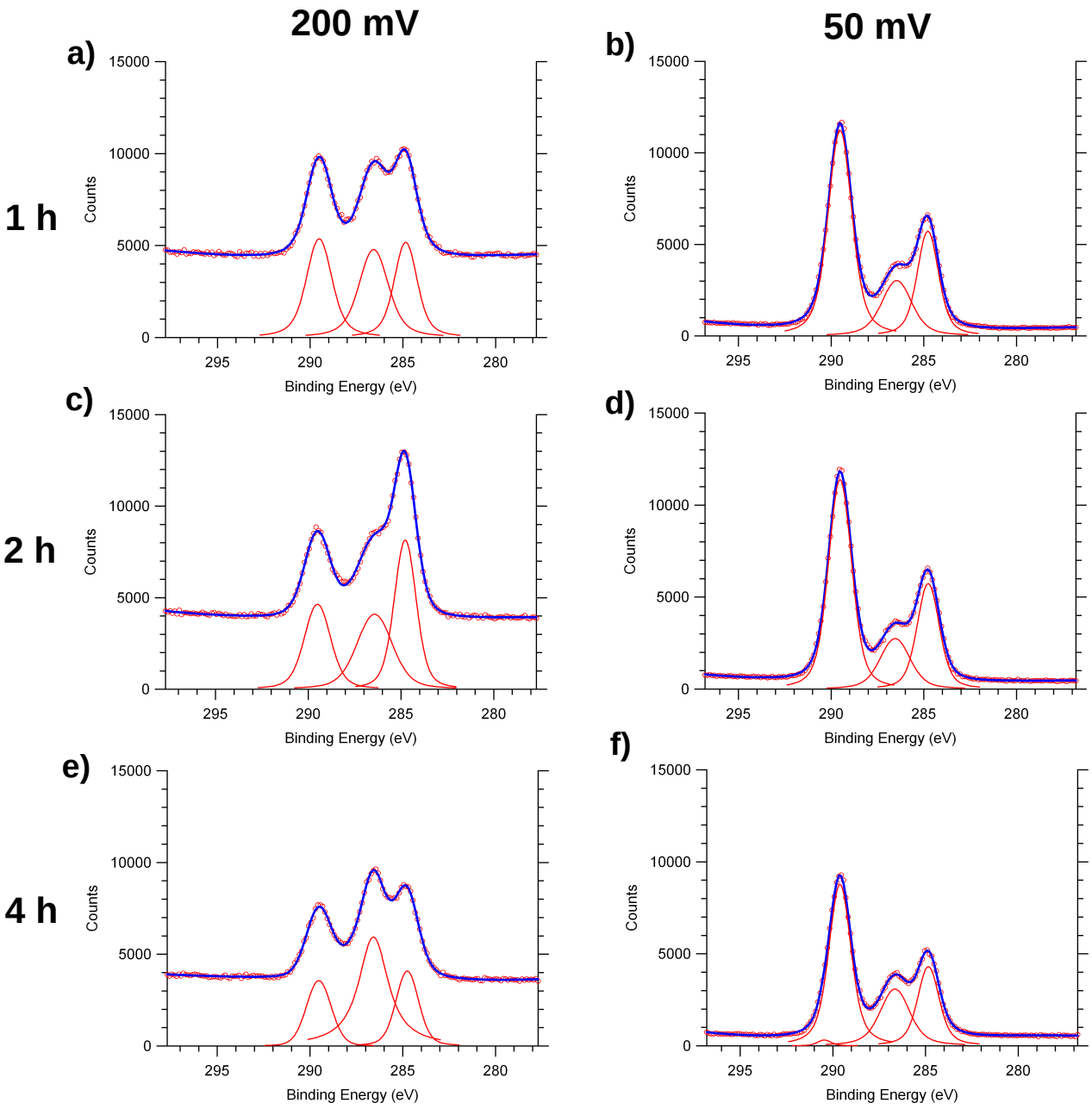

Figure 3.7. High-resolution XPS spectra of the carbon (1s) area for six single-crystal Si electrodes charged in half-cells with 1NM2+$LiPF_6$ electrolyte and held at either 200 mV or 50 mV for 1, 2, or 4 hours.

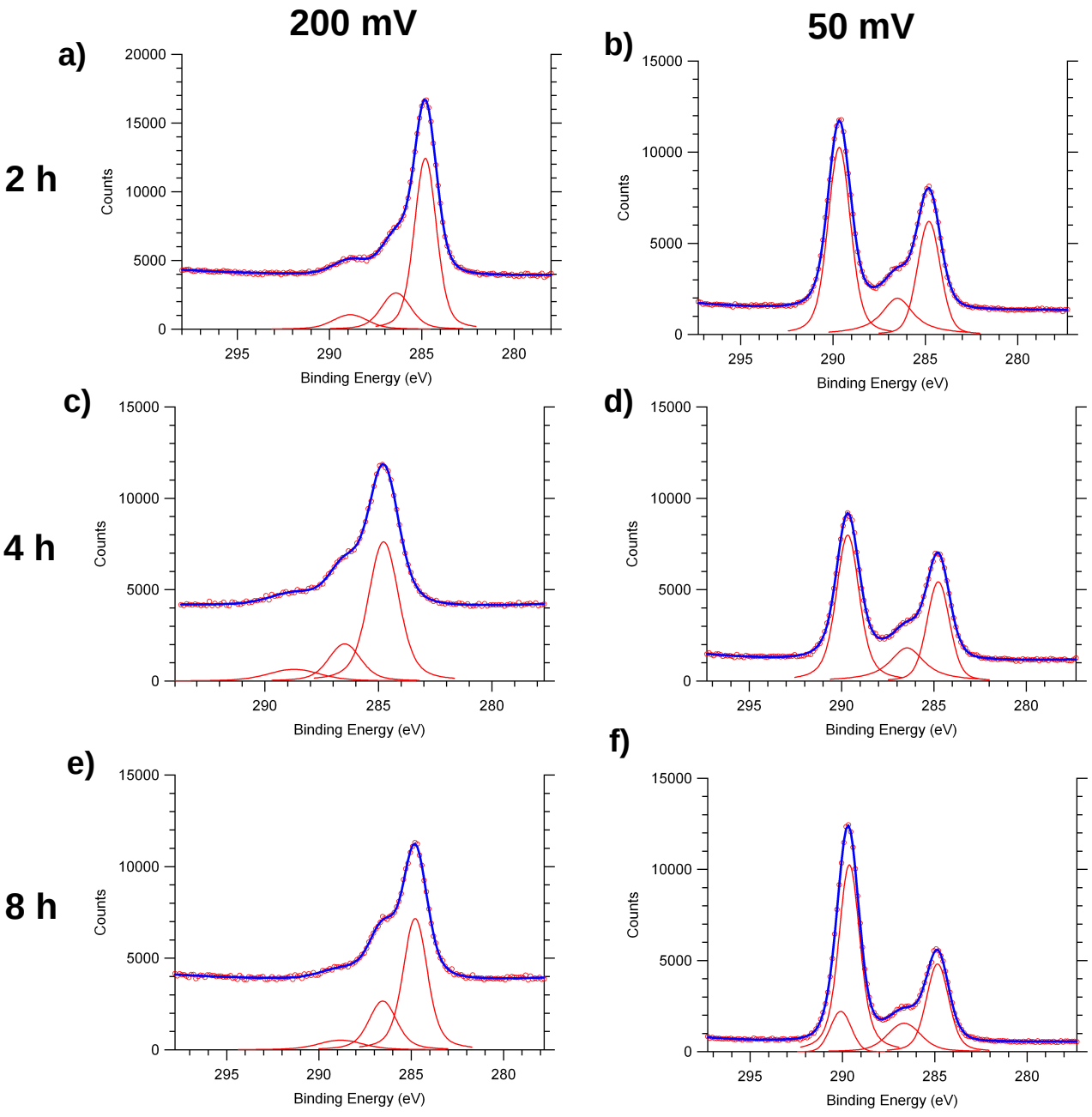

Figure 3.8. High-resolution spectra of the carbon (1s) area for six single-crystal Si electrodes charged in half-cells with 1S3M2+$LiPF_6$ electrolyte and held at either 200 mV or 50 mV for 2, 4, or 8 hours.

result of cells charged to and held at 200 mV. Much like the results shown in Figure 3.7, there are three principal peaks visible, at 284.8 eV, 286.5 eV, and 289.5 eV. A comparison of the spectra obtained after lithiation in 1S3M2 (Fig. 3.8) and in 1NM2 (Fig. 3.7) shows that the highest-binding energy peak in all three spectra on the left side of Figure 3.8 (1S3M2 electrolyte) is much smaller than the equivalent peaks in Figure 3.7 (1NM2 electrolyte). The middle peak is somewhat smaller in comparison as well. In contrast, the spectra on the right side of Figure 3.8 are much more similar to their counterparts in Figure 3.7, with a very large highest-binding energy peak that dwarfs both the adventitious carbon and glycol-like carbon peaks. The middle ether-like peak in these spectra for 1S3M2 also appears slightly smaller than its counterpart from the 1NM2 spectra at 50 mV.

3.3.4 XPS Correlation Analysis

Another observation from Figures 3.7 and 3.8 is that there are moderately large variations in the absolute intensities of many of the peaks between different samples. These variations are most likely due to inhomogeneities in the SEI layers formed on top of the silicon electrodes. In order to help identify what changes are reflections of the changes in surface chemistry, we embarked on a program of correlation analysis to attempt to extract information from the data in aggregate that would otherwise be obscured by sample-to-sample variations. This approach can shed light on which elements are positively correlated (indicating that they are most likely present together in the SEI) or negatively correlated (indicating that the species containing one is replacing or covering up the other).

First, we examine the correlations apparent for the high-binding energy carbon peak at around 289.5 eV. Figure 3.9 shows a correlation plot where each point signifies a single

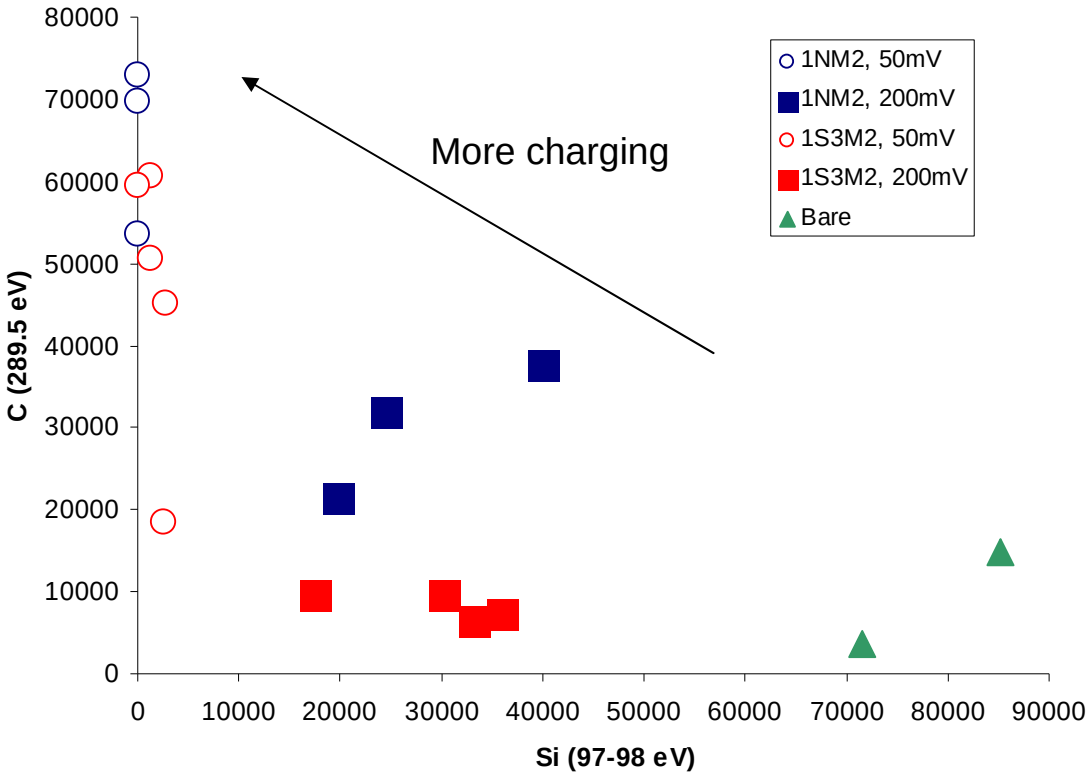

Figure 3.9. XPS correlations between the high-binding energy carbon (1s) peak at approximately 289.5 eV and the bulk silicon (2p) peak at approximately 97-98 eV. Results from cells using 1NM2 electrolyte are in blue, cells using 1S3M2 electrolyte are in red, and bare Si controls are in green. Cells charged to and held at 50 mV are in open circles while cells charged to and held at 200 mV are in filled squares.

electrode, plotted according to its peak area for the silicon (2p) peak on the x-axis and its peak area for the 289.5 eV carbon (1s) peak on the y-axis. The plot includes electrodes from both 1NM2 and 1S3M2 cells held at various voltages (mostly 50 mV and 200 mV) as well as several bare Si samples that were never exposed to electrolyte. The bare silicon samples lie at the right extreme, representing only carbon contamination and very high silicon signal. All other points, from electrodes that were lithiated to varying degrees, contain more carbon and less silicon. The negative correlation between high-binding carbon and Si is thus apparent when the data are plotted in this way. There is also a trend that the points that represent higher degrees of lithiation (those in open circles) correspond to much higher amounts of carbon and lower amounts of silicon.

Figure 3.10 shows correlations of the highest-binding carbon (1s) peak in order to determine if the peak's origin is in an oxidized species (such as a carboxylic acid) or a fluorinated species (such as CF_2). First, in Figure 3.10a, the correlation between the highest-binding carbon (1s) peak and the total fluorine is presented. The negative correlation is quite clear, and more highly charged samples have more carbon and less fluorine. In addition, the electrodes charged in the presence of 1NM2 electrolyte generally display more carbon and less fluorine than the electrodes charged in the presence of 1S3M2 electrolyte, though all the points appear to lie near the same curve. On the other hand, Figure 3.10b, shows the correlation between the highest-binding carbon (1s) peak and the total oxygen (1s) area. In this case, there is a positive correlation, with both high-binding carbon and oxygen increasing together as charging and lithiation proceed to greater extents. Again, the points from cells with the two different electrolytes appear to follow one curve, though the 1NM2-charged electrodes display higher

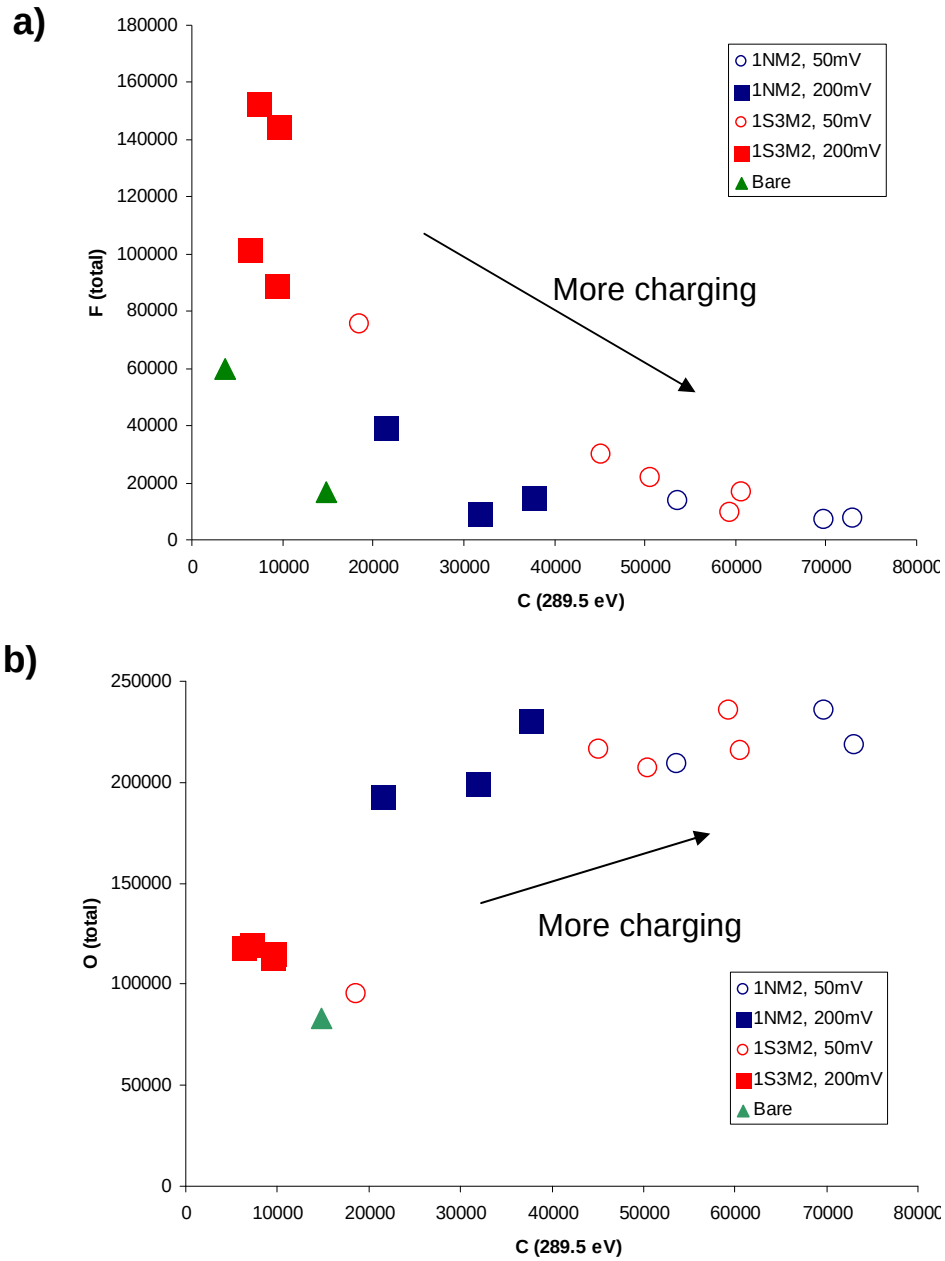

Figure 3.10. XPS correlations between the high-binding energy carbon (1s) peak at approximately 289.5 eV and: **a)** the total fluorine (1s) peak area near 685 eV, and **b)** the total oxygen (1s) peak area near 531 eV. Results from cells using 1NM2 electrolyte are in blue, cells using 1S3M2 electrolyte are in red, and bare Si controls are in green. Cells charged to and held at 50 mV are in open circles while cells charged to and held at 200 mV are in filled squares.

carbon (and thus also higher oxygen) than their counterparts from cells containing 1S3M2. Taken together, the comparisons in Figure 3.10 unambiguously demonstrate that the highest-binding carbon peak has its origins in a highly oxidized species such as a carboxylate or ester and not in a fluorinated species.

The correlations of the total phosphorus (2p) peak area are also useful to examine. In Figure 3.11a, the correlation of the high-binding carbon (1s) with total phosphorus (2p) is presented. The bare silicon controls displayed no phosphorus and very little carbon, while the lithiated electrode samples display a negative correlation with relatively higher degrees of charge displaying more carbon and less phosphorus. Both 1NM2 and 1S3M2 cells produced points that appear to fall on the same curve. The electrodes charged with 1NM2 also tend to be clustered farther to the right, indicating the presence more carbon and less phosphorus at the electrode surface for 1NM2 than for 1S3M2. The negative correlation of both P and F with the high-binding carbon suggests that P and F may be positively correlated with one another. Figure 3.10b confirms this relationship, showing a positive correlation with less phosphorus and fluorine on samples that had been charged more extensively. In general, electrodes from 1NM2-containing cells also displayed lower amounts of both phosphorus and fluorine than those from cells using 1S3M2.

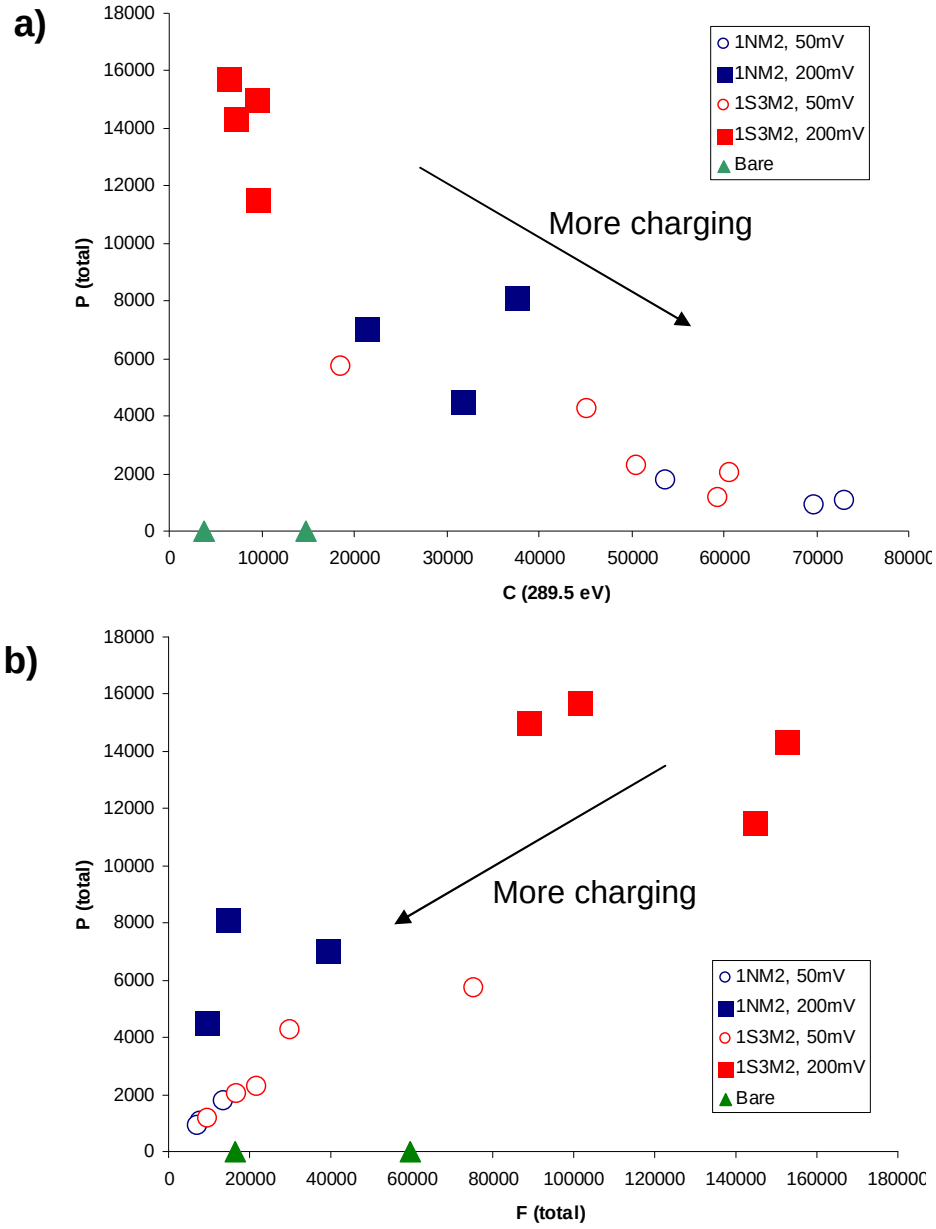

Figure 3.11. XPS correlations between the total phosphorus (2p) area near 133 eV and: **a)** the total carbon (1s) peak area at approximately 289.5 eV, and **b)** the total fluorine (1s) peak area near 685 eV. Results from cells using 1NM2 electrolyte are in blue, cells using 1S3M2 electrolyte are in red, and bare Si controls are in green. Cells charged to and held at 50 mV are in open circles while cells charged to and held at 200 mV are in filled squares.

3.4 Discussion

Figures 3.5 and 3.6 together show the formation of a significant carbon-containing SEI layer on the surface of the silicon electrodes that significantly attenuates the signal from the underlying silicon. The small remaining silicon peak at 100.5 eV seen in Figures 3.5f and 3.6f may be due to either native silicon oxide from the electrode or the organosilicon electrolyte depositing onto the surface. Large amounts of fluorine, lithium, and oxygen as well as small amounts of phosphorus all appear in the SEI layer as well. Qualitatively, the SEI layers appear quite similar between silicon electrodes charged in 1NM2 and 1S3M2-based electrolytes. Furthermore, examination of the carbon (1s) data in Figures 3.7 and 3.8 leads to two major observations. First, the data show that it is the voltage that determines the major chemical components of the SEI layer formation, not the time spent holding at the selected potential. Second, the SEI layers form relatively quickly, reaching an apparent steady state as judged by XPS within as little as 1 hour.

While battery performance is typically characterized as a function of charging rate, the intrinsic electrochemical reactions that occur at the surface primarily depend on the potential of the electrode surface. For both 1NM2-containing cells in Figure 3.7 and 1S3M2-containing cells in Figure 3.8, the SEI layer observed at 200 mV is similar at all time points. Likewise, for each electrolyte, the SEI layer observed at 50 mV is similar at all time points. However, for both electrolytes, the SEI layer observed at 200 mV is drastically different than that observed for the same electrolyte at 50 mV. In addition, at 200 mV, there is significantly more high-binding carbon present (at 289.5 eV) on the electrodes from the 1NM2-containing cells than the electrodes from the 1S3M2-containing cells. This difference in the carbon signals most likely

indicates that 1NM2 begins to decompose at a higher potential than 1S3M2 does, which could also explain the SEM observations from Figure 3.4. If it is easier for 1NM2 to decompose than for 1S3M2, the decomposition reaction might be initiated at more points on the surface, as seen from the microscopy results. At 50 mV, on the other hand, the SEI layer observed for 1NM2 greatly resembles that observed at 50 mV for 1S3M2, indicating that the end-stage SEI is not greatly affected by the structural difference between 1NM2 and 1S3M2. In addition to its independence from the hold time at the selected potential, the observed SEI is also independent of the total charge accumulated during the cell test. This can be observed by comparing a cell that spent a long time at 200 mV to a cell that spent a short time at 50 mV. For instance, in comparing a cell that spent 8 hours charging at 200 mV (Fig. 3.8e) to a cell that spent 2 hours charging at 50 mV (Fig. 3.8b), one notices that the peak area at 289.5 eV is much larger for the 50mV cell despite the shorter test time. If we assign the highest-binding energy carbon (1s) peak as the main carbon-containing component of the SEI, then this result means that a short time at 50 mV is sufficient to create much more SEI than a long time at 200 mV. The higher amount of SEI on the 50 mV cell appears even though the 200 mV cell accumulated more total charge (29.6 μA·h) than the 50 mV cell (15.6 μA·h).

The relationships between elemental peak areas plotted in figures 3.9 – 3.11 were selected because the two elements under evaluation displayed a clearly identifiable negative or positive correlation. However, many other correlation plots for other pairs of elements displayed no such clear trends (not shown for the sake of brevity). In particular, the total lithium (1s) peak area did not display any noticeable correlation with any other elemental peak. Lithium is a particularly difficult element to analyze for two reasons: First, the measured counts are quite low

as Li has an extremely low atomic sensitivity factor of 0.025, compared to 0.29 and 1.00 for the 1s orbitals of carbon and fluorine, respectively. Secondly, lithium is nearly always present in the +1 oxidation state, so that all lithium-containing species give rise to a peak at nearly the same energy. Therefore, the lack of observed correlations may indicate that multiple lithium species are being formed on the sample surface over time, but therefore as other peaks grow in and/or disappear, the *total* lithium signal is complex and not possible to deconvolute. The middle peak at 286.5 eV in the carbon (1s) spectrum is the same way: no strong correlations were observed when paired with any other elemental peak. This may be due to contamination effects, as while the main carbon contamination appears at 284.8 eV, some lightly oxidized contamination appears as well.

Even though not all elements show correlations from these data, the correlations that are observed in Figures 3.9-3.11 allow deeper understanding of the SEI layer formation process. As seen in Figure 3.9, the fact that high-binding carbon at 289.5 eV (and oxygen, which Figure 3.10b shows it is positively correlated with) grows as the cells are charged and the Si peak decreases means that the carbon and oxygen are forming a surface layer on top of the Si electrode. This increase in carbon and oxygen is a direct observation of the SEI formation process. Furthermore, the positive correlation between P and F seen in Figure 3.11b means that these two elements appear proportionally in the surface layer. This positive correlation is not surprising since the only source of either element is the $LiPF_6$ salt in the electrolyte. At first glance it may appear that this conclusion means that the PF_6 is not decomposing significantly. However, closer examination of the correlation plot in Figure 3.11b shows that the slope is approximately 1/12. If only $LiPF_6$ were depositing on the electrode surface, the slope should be

1/6. Instead, the ratio of 1/12 indicates that there is more fluorine present than can be explained by the presence of $LiPF_6$. Thus, some of the $LiPF_6$ in the electrolyte must be decomposing to form another F-containing species, while other $LiPF_6$ may remain intact to produce the phosphorus signal and some of the fluorine signal. This other F-containing species could be a fluorinated silicon oxide as seen in other studies of the silicon SEI[31]. Lastly, the negative correlation between P/F and C/O seen in Figures 3.10a and 3.11a implies that these two groups of elements are present at different times. The fact that P/F decrease together as charging proceeds while C/O increase together means that there is an initial P/F enriched layer that is later covered up by a C/O enriched layer.

3.5 Conclusion

Through the course of these studies, a picture of the SEI formation on Si single-crystal electrodes using organosilicon-based electrolytes has emerged. The timescale of SEI formation is clearly on the order of minutes, as samples charged for as little as 1 hour have already reached a steady state in terms of composition. Initially, a phosphorus- and fluorine-rich layer is deposited on the Si/SiO_x surface, the origin of which must be the $LiPF_6$ salt. With continued charging at lower potentials (closer to Li/Li^+), the initial P/F containing layer is covered up by a carbon- and oxygen-enriched layer. The origin of this second layer, representing something more like the traditionally envisioned SEI, must be the organosilicon electrolyte solvent. Furthermore, the composition of the SEI is not very different between 1NM2 and 1S3M2, though there is evidence that the 1NM2 begins to decompose at a higher potential than 1S3M2. This latter fact is direct evidence that the carbon spacer in the structure of 1S3M2 contributes to an increased

electrochemical stability compared to 1NM2. Hopefully, these results will contribute to a better understanding of SEI formation on silicon electrodes that will also translate to more practically feasible geometries like Si nanoparticles. With better understanding of silicon SEI formation, perhaps new electrolytes can be designed to form a mechanically and electrochemically robust SEI that can survive the extreme volume changes that silicon anodes are subject to.

3.6 References

(1) Goodenough, J. B.; Park, K.-S. *Journal of the American Chemical Society*, **2013**, *135*, 1167.

(2) M. B. Armand, *Materials for Advanced Batteries* (Eds: D. W. Murphy, J. Broadhead, B. C. H. Steele), Plenum, New York. **1980**, 145.

(3) Di Pietro, B.; Patriarca, M.; Scrosati, B. *Journal of Power Sources*, **1982**, *8*, 289.

(4) Mizushima, K.; Jones, P. C.; Wiseman, P. J.; Goodenough, J. B. *Materials Research Bulletin*, **1980**, *15*, 783.

(5) Hayner, C. M.; Zhao, X.; Kung, H. H. *Annual Review of Chemical and Biomolecular Engineering*, **2012**, *3*, 445.

(6) Endo, M.; Kim, C.; Nishimura, K.; Fujino, T.; Miyashita, K. *Carbon*, **2000**, *183*, 197.

(7) Obrovac, M. N.; Christensen, L. *Electrochemical and Solid State Letters*, **2004**, *7*, A93.

(8) Chon, M. J.; Sethuraman, V. A.; McCormick, A.; Srinivasan, V.; Guduru, P. R. *Physical Review Letters*, **2011**, *107*, 045503.

(9) Ryu, J. H.; Kim, J. W.; Sun, Y.-E.; Oh, S. M. *Electrochemical and Solid-State Letters*, **2004**, *7*, A306.

(10) Gauthier, M.; Danet, J.; Lestriez, B.; Roué, L.; Guyomard, D.; Moreau, P. *Journal of Power Sources*, **2013**, *227*, 237.

(11) Chan, C. K.; Peng, H. L.; Liu, G.; McIlwrath, K.; Zhang, X. F.; Huggins, R. A.; Cui, Y. *Nature Nanotechnology*, **2008**, *3*, 31.

(12) Liu, X. H.; Zhong, L.; Huang, S.; Mao, S. X.; Zhu, T.; Huang, J. Y. *ACS Nano*, **2012**, *6*, 1522.

(13) Saito, M.; Nakai, K.; Yamada, T.; Takenaka, T.; Hirota, M.; Kamei, A.; Tasaka, A.; Inaba, M. *Journal of Power Sources*, **2011**, *196*, 6637.

(14) Yao, Y.; McDowell, M. T.; Ryu, I.; Wu, H.; Liu, N. A.; Hu, L. B.; Nix, W. D.; Cui, Y. *Nano Letters*, **2011**, *11*, 2949.

(15) McDowell, M. T.; Lee, S. W.; Harris, J. T.; Korgel, B. A.; Wang, C.; Nix, W. D., Cui, Y. *Nano Letters*, **2013**, *13*, 758.

(16) Wu, H.; Cui, Y. *Nano Today*, **2012,** *7*, 414.

(17) Xu, K. *Chemical Reviews*, **2004**, *104*, 4303.

(18) Rossi, N. A. A.; West, R. *Polymer International*, **2009**, *58*, 267.

(19) Zhang, L.; Zhang, Z.; Harring, S.; Straughan, M.; Butorac, R.; Chen, Z.; Lyons, L.; Amine, K.; West, R. *Journal of Materials Chemistry*, **2008**, *18*, 3713.

(20) Chen, X.; Usrey, M.; Pena-Hueso, A.; West, R.; Hamers, R. J. *Journal of Power Sources*, **2013**, *241*, 311.

(21) Dong, J.; Zhang, Z.; Kusachi, Y.; Amine, K. *Journal of Power Sources*, **2011**, *196*, 2255.

(22) Verma, P.; Maire, P.; Novák, P. *Electrochimica Acta*, **2010**, *55*, 6332.

(23) Smith, A. J.; Burns, J. C.; Zhao, X.; Xiong, D.; Dahn, J. R. *Journal of the Electrochemical Society*, **2011**, *158*, A447.

(24) Moulder, J. F.; Stickle, W. F.; Sobol, P. E.; Bomben, K. D. *Handbook of X-ray Photoelectron Spectroscopy*, Perkin-Elmer Corp., Eden Prairie, MN, 1992.

(25) Pale-Grosdemange, C.; Simon, E. S.; Prime, K. L.; Whitesides, G. M. *Journal of the American Chemical Society*, **1991**, *113*, 12.

(26) Gelius, U.; Hedén, P. F.; Hedman, J.; Lindberg, B. J.; Manne, R.; Nordberg, R.; Nordling, C.; Siegbahn, K. *Physica Scripta*, **1970**, *2*, 70.

(27) Clark. D. T.; Feast, W. J.; Kilcast, D.; Musgrave, W. K. R. *Journal of Polymer Science Part A: Polymer Chemistry*, **1973**, *11*, 389.

(28) Obrovac, M. N.; Krause, L. J. *Journal of the Electrochemical Society*, **2007**, *154*, A103.

(29) Nie, M.; Chalasani, D.; Abraham, D. P.; Chen, Y.; Bose, A.; Lucht, B. L. *Journal of Physical Chemistry C*, **2013**, *117*, 1257.

(30) Nie, M.; Abraham, D. P.; Chen, Y.; Bose, A.; Lucht, B. L. *Journal of Physical Chemistry C*, **2013,** *117*, 13403.

(31) Philippe, B.; Dedryvère, R.; Gorgoi, M.; Rensmo, H.; Gonbeau, D.; Edström, K. *Chemistry of Materials*, **2013,** *25*, 394.

Chapter 4

Formation of Graphite Nanopillars on HOPG and Their Surface Modification Using Photochemical Grafting and "Click" Chemistry

4.1 Introduction

Graphite is a common and well-studied material with many practical uses, including the writing "lead" of pencils and many varieties of lubricants[1]. It performs well in these applications due to its somewhat unique structure as a layered material. Graphite consists of stacks of two-dimensional planes of sp^2-hybridized carbon atoms in fused hexagonal rings. Because each carbon atom is fully bonded only to atoms within its own sheet, the attractive forces between sheets are relatively small (Van der Waals interactions) and the interlayer spacing is quite large (approximately 3.4 Angstrom, much larger than a typical C-C bond). This leads to relatively easy separation of the layers from one another, which allows some graphite to remain behind as a pencil is dragged across a surface, leaving a mark.

Due to its layered structure, graphite is anisotropic in many of its properties. Since each layer is completely conjugated, electrical conduction is relatively fast in the two directions parallel to the sheets and relatively slow in the perpendicular direction. The surface chemistry is also anisotropic; the surfaces that expose sheet edges are referred to as the edge planes, while the surfaces parallel to the sheets are referred to as the basal planes. Another anisotropic characteristic of graphite is that electron transfer out of the edge plane is approximately 10^5 times faster than electron transfer out of the basal plane[2]. As there are also may be dangling bonds present on the edge plane of graphite where there are none on the basal plane, the edge planes are also much more chemically reactive.

In recent years, a great deal of research attention has been focused on graphene, which is the name given to a single layer of graphite[3,4,5]. For many years, graphene (or more accurately, any purely two-dimensional material) was thought to be thermodynamically unstable[6,7]. It came as a large surprise, then, when Geim and co-workers were able to isolate atomically thin graphene in 2004[8]. Their so-called "mechanical exfoliation" method involved repeatedly applying adhesive tape to a successively thinner sample of graphite, each step discarding more of the layers. Eventually, one reaches a limit where some of the remaining material is a single layer thick; a helpful imaging strategy using a precisely controlled thickness of SiO_2 on a silicon wafer substrate allows rapid separation of true graphene from multilayer structures[9]. It is also worth emphasizing that graphene represents the thinnest imaginable material.

Once the synthetic route was established, many groups raced to explore the properties of graphene, which turned out to be exceptional in many ways. Charge carriers in graphene completely lose their effective mass and are better described by relativistic equations than by the Schrodinger equation that typically suffices for all other condensed matter electronic properties[3,4]. Electrons traveling through graphene can travel over relatively long (sub-micron) distances without scattering (ballistic transport)[3]. Because the quantum world is so "close to the surface" in graphene, observations of phenomena such as the quantum Hall effect at room temperature[10] have also been reported. Indeed, for a surface chemist, graphene is an extremely attractive material to study since in most respects it is essentially a *pure surface* – there is no "bulk". Alternatively, one can simply subtract a dimension and imagine the edge planes as the surfaces and the basal plane as the bulk.

Despite the intense pace of research on graphene, one factor has limited its use in scales beyond the laboratory: the problem of manufacture. The mechanical exfoliation method is highly effective at producing small numbers of extremely high-quality samples for exploring new physics, but is not sufficient for a production line. Alternatively, various groups have tried working with a related material, graphene oxide (GO)[11,12]. GO (also sometimes referred to by other names such as chemically converted graphene or functionalized graphene sheets) is obtained by oxidation of bulk graphite[13,14], generally by using strong acids (often sulfuric and nitric) and a chemical oxidant such as $KMnO_4$. The resulting material is hydrophilic and possesses many different oxygen functional groups (carbonyl, epoxide, hydroxyl, and others) interspersed around the lattice, though the material is believed to have a disordered structure and understanding of the exact structures involved is still lacking[15]. Crucially, GO does not possess any of the same unusual electronic properties as graphene due to its structural differences, and therefore many groups have explored reduction of GO as a route to larger quantities of high-quality graphene. The reduction can be chemical[16,17] or electrochemical[18]. Reduced graphene oxide is closer to pristine graphene than GO, but still retains some residual oxygen as well as structural damage from the oxidation and reduction processes (for example, loss of carbon atoms from the basal plane due to CO_2 production during the oxidation step)[15].

Other methods that do not involve graphene oxide have also been attempted to synthesize high-quality graphene. Chemical vapor deposition methods are capable of producing quite large and pristine areas of graphene on a metal substrate such as Cu[19], Ni[20], or Pd[21]. In some cases the underlying substrate can even be dissolved or the graphene otherwise removed[19], though the CVD methods suffer from the same scaling drawback as mechanical exfoliation, though in some

cases they may be adaptable to the computing industry via existing wafer processing techniques. Some researchers have also opted for a bottom-up approach using organic synthesis techniques[22], though this method is most likely to be able to produce only smaller graphene samples, though the promise of scalability is attractive. Therefore, despite the variety of techniques for synthesizing materials in the graphene family, no method yet exists for producing larger quantities of high-quality graphene.

In this work we present a method of patterning highly ordered pyrolytic graphite (HOPG) samples on the nanoscale in order to serve as a first step on a route to functionalized graphene nanoplatelets. The samples are patterned using a block copolymer method that incorporates metal salts exclusively into one block of the resulting polymer film. Specifically, these experiments used a block copolymer of polystyrene and 2-vinyl pyridine, the latter of which coordinates to metal ions via the lone pair of the nitrogen in the pyridine ring. Then, because the block copolymer phase separates into micelles of the metal-pyridine block in a matrix of the polystyrene block, subsequent removal of the polymer by exposure to UV-generated ozone leaves behind metal nanoparticles of well-defined size in an array on the surface with spaces in between each particle and its neighbors. These particles can then serve as an etch mask in an anisotropic plasma etch in order to create graphite nanopillars on the surface. Because of the orientation of the graphite used as a starting material, the graphite nanopillars formed in this way can be thought of as stacked graphene platelets, each one perpendicular to the pillar height. More importantly, the edge planes are exposed along the sidewalls of the pillars, while the basal planes of the graphene discs are protected by their neighbors above and below them in the stack.

The unique geometry of these graphite nanopillars allows chemical functionalization to occur exclusively on the edge planes of the graphite, which was performed using two different chemical methods. Photochemical grafting of an alkene, previously explored on a variety of materials in our group, including silicon[23], diamond[24], metal oxides[25,26,27], and carbon nanofibers[28], was used to modify the pillars with an alkyl chain containing a cleavable end group that was used as a handle for further modifications. In another strategy, exposure to sodium azide attached N_3 groups to the sidewalls of the pillars and also allowed for further modification using the copper-catalyzed azide-alkyne cycloaddition reaction (CuAAC), commonly known as an example of "click" chemistry[29]. Both functionalization strategies were verified using XPS and FTIR spectroscopy, confirming the presence of the new groups on the surface. These strategies could serve as a valuable route in the future towards graphene nanoplatelets with arbitrary functionalization on their edges to impart solubility, photochemical properties, or other desired functions.

4.2 Experimental Methods

Figure 4.1 shows an overview of the various steps required to create the graphitic nanopillars. Detailed information about each step follows.

4.2.1 Block Copolymer – Metal Salt Composite

Based on a previously published method[30], 25mg of $NiCl_2 \cdot 6H_2O$ (99.999% trace metals basis, Aldrich) was dissolved in 5mL of ethanol in an argon-purged glove box to make a green solution. In a separate vial, poly(styrene)-b-(2-vinylpyridine) (Polymer Source, 32.5-b-7.8 kDa,

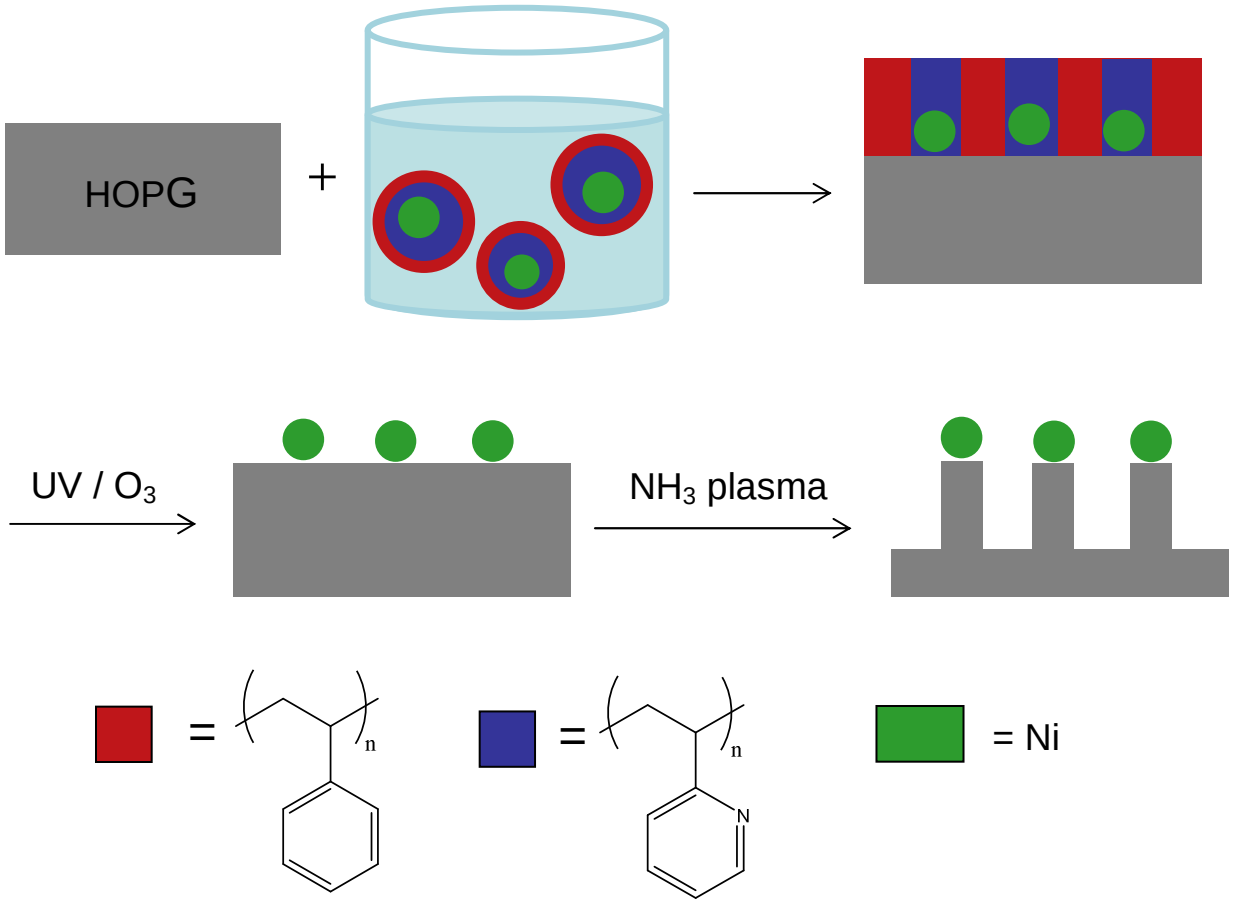

Figure 4.1. Schematic overview of graphite nanopillar synthesis. First, HOPG substrates are coated with a block copolymer solution, at which point the solvent evaporates. The block copolymer forms a well-ordered surface array as it slowly dries. Under exposure to UV-light-produced ozone, the organic polymer matrix is removed via conversion to CO_2, leaving only a well-ordered array of metal nanoparticles behind. Finally, an anisotropic NH_3 plasma etch removes graphite from the substrate except where the underlying area is protected by a metal nanoparticle, leaving graphitic pillars on the surface.

M_w/M_n = 1.05) block copolymer was dissolved in toluene to make a 0.25% solution of the polymer by weight. 0.27 of the $NiCl_2$ – ethanol solution was then added to 10mL of the 0.25% polymer solution in order to produce a metal:pyridine ratio of 1:4. This solution was mixed for 5 hours in a warm water bath at 50 °C. The result was a light blue, transparent solution of polymer and metal salt.

Highly ordered pyrolytic graphite (SPI-2 HOPG, Structure Probe, Inc.) was first cleaned by exfoliation of the surface layers with adhesive tape. This process was performed at least two times per sample (more if required to obtain a very smooth, unscratched surface). The $NiCl_2$ – polymer solution was then spin-coated (Laurell Technologies) onto the HOPG surface at 2000rpm. After the spin-coated film had dried, the polymer-coated HOPG was placed under a mercury lamp in order to remove the polymer via ozone production by the UV emission of the lamp. Typical UV exposures were 6 hours. The UV cleaning removes the polymer while leaving the metal salt behind. Images of the resulting nanoparticle arrays were obtained using a scanning electron microscope (LEO Supra 55VP).

4.2.2 Nanopillar Formation

Once the arrays of metal nanoparticles were formed on the HOPG surface, the samples were placed into a custom-built CVD chamber equipped with an NH_3 gas source fitted with a mass flow controller. Figure 4.2 shows a schematic of the plasma chamber as used for these experiments. The samples rest on a grounded metal platform, approximately 2cm below an electrode connected to an RF power supply. Once the samples are in place, the chamber was evacuated, after which the NH_3 flow was started. Generally a rate of 100 standard cubic

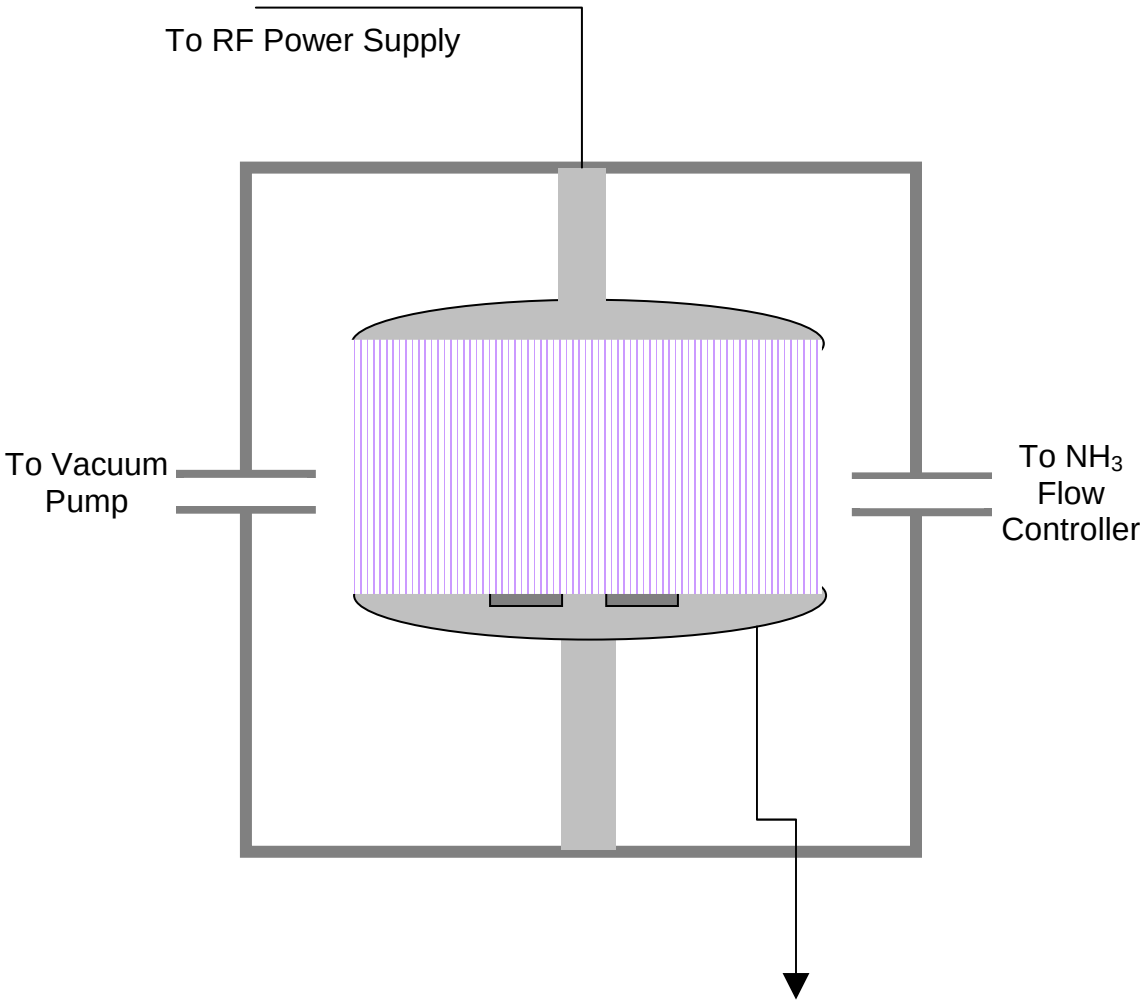

Figure 4.2. Schematic of NH_3 etching apparatus. Samples are placed on the lower electrode plate, which is electrically grounded. The RF power supply is connected to the top electrode, located approximately 2cm above the lower plate. NH_3 gas enters from the mass flow controller on the right, and the vacuum pumping system is connected on the left. When the power supply is on, purple-colored plasma appears between the two plates.

centimeters per minute (sccm) of NH_3 was used. Initially the valve to the vacuum pumping system was kept open as the plasma was ignited (using an RF power of 360 W). Once the plasma was lit, the vacuum valve was mostly closed so that the pressure was controlled by a parallel needle valve, which was adjusted so the total chamber pressure was 3 torr. Typically the plasma etch was continued for 5 minutes, during which time the metal platform under the sample began to glow red-hot. After etching was complete, the power supply was turned off, the vacuum valve was reopened fully, and the sample was allowed to cool down in flowing NH_3 for 15 minutes. The NH_3 flow was then stopped and cooling continued for another 30 minutes. The resulting pillars were then imaged via SEM.

4.2.3 Functionalization of Nanopillars via Photochemical Grafting

For photochemical grafting experiments, a single drop of neat trifluoroacetic acid-protected 10-aminodec-1-ene (TFAAD) (Astatech, Inc.) was placed on top of each graphite sample, which were then sealed inside a custom-built stainless steel cell with a quartz window in the top plate to allow UV transmission. Figure 4.3 shows a schematic of the cell used for the grafting experiments. The cells were assembled so that the quartz window was in contact with the graphite surface, forming only a thin surface tension layer of the alkene between the graphite sample and the quartz window. All cells were sealed inside an argon-purged glove box, then removed to atmosphere after sealing. Cells were placed under a mercury lamp emitting 254nm UV light (~10mW/cm^2) for set grafting times, typically 16 hours. After grafting was complete, cells were unsealed and the samples rinsed with alternating washes of methanol and chloroform.

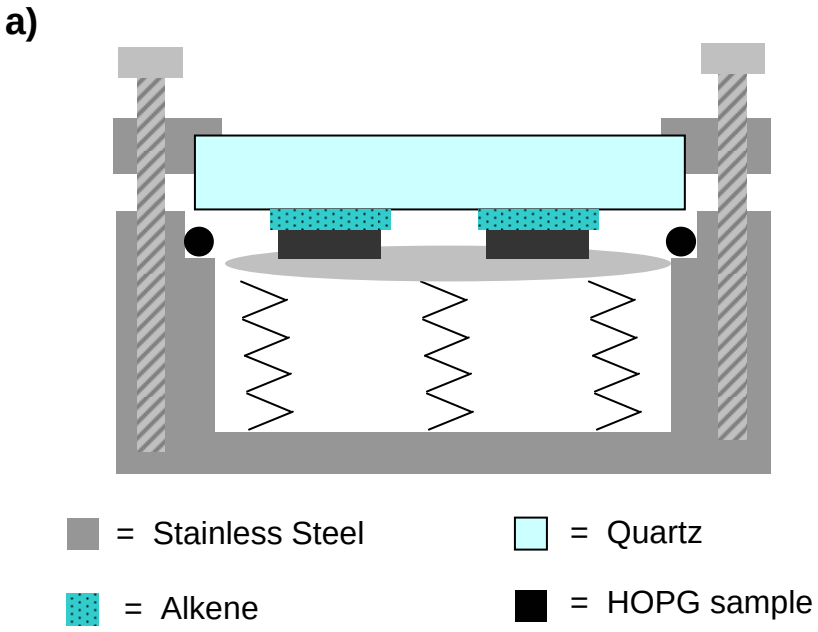

Figure 4.3. a) Schematic of the cell used for photochemical grafting experiments. The samples are held against the quartz window by a lower platform with springs. A thin layer of the reactive alkene is held in between the sample surface and the window by surface tension. The entire cell is bolted together and sealed in an argon-atmosphere glove box before being removed to atmosphere for the UV exposure. **b)** structure of trifluoroacetic acid-protected 10-aminodec-1-ene (TFAAD).

TFAAD-functionalized nanopillar samples underwent further reaction to remove the trifluoroacetate group, leaving a primary amine at the end of the functionalized alkane chain. To perform this deprotection, 0.2g of $NaBH_4$ (Aldrich) was added to 10mL of anhydrous methanol (Aldrich) were combined in a vial along with TFAAD-functionalized nanopillar samples. The vial was sealed and the cap was pierced with a needle to allow evaporation of solvent. The vials were then placed into a block heater at 60 °C and allowed to react, typically for 48 h. The resulting samples were characterized using FTIR to confirm the successful removal of the trifluoroacetate moiety and formation of the primary amine.

In the final step, N-hydroxyl succinimide-functionalized poly(ethylene glycol) (PEG-NHS) (2kDa, NanoCS) was added to dimethyl acetamide (Aldrich) to make a 0.01M solution. 1mL of the resulting solution was combined with 4mL of SSPE 1x Buffer (Aldrich) and amine-terminated graphite nanopillar samples were added into the reaction mixture, typically for a reaction time of 5 hours. After completion, the samples were rinsed with alternating washes of methanol and deionized water. Successful reaction was confirmed via FTIR.

4.2.4 Functionalization of Nanopillars via “Click” Chemistry

For copper-catalyzed azide-alkyne cycloaddition (CuAAC) reactions, based on previously published procedures[31], first graphite nanopillar samples were immersed in a saturated solution containing 0.04g of NaN_3 (Fluka) in 20 mL acetonitrile. The reaction was performed in a well-ventilated fume hood and the reaction vessel was placed into an ice bath to maintain a temperature of 0 °C. Next, 3 drops of ICl (Aldrich, ACS grade) were added to the reaction mixture and stirred for 15 minutes before being removed from the ice bath and warmed

to room temperature. *Note: ICl is extremely corrosive, reacts with water, and can cause severe burns in liquid or vapor form, and should always be used in a fume hood.* The above procedure creates IN_3 species in solution, which are the actual source of azide groups for the subsequent step. Once the reaction solution was warmed, graphite nanopillar samples were immersed in the solution with continued stirring. Typical reaction times were 3 h, after which the samples were rinsed with alternating washes of methanol and chloroform. The presence of the azide group on the surface was verified by FTIR spectroscopy.

For the second step of the reaction, a 1mM solution of $Cu(BF_4)_2 \cdot xH_2O$ (Aldrich) in DMSO was prepared. 25mL of this solution was placed into another container, to which was added 0.0133g of tris-(benzyltriazolylmethyl)amine) (TBTA) (Aldrich, 97%), to form a light blue solution. In a different container, a 20mM solution of trifluoromethoxyphenylacetylene (TFMPA) was made in 50% deionized H_2O and 50% DMSO by volume. Other experiments used a 200 μM solution of PEG-alkyne (1 kDa, Creative PEGWorks) in deionized H_2O for the alkyne solution. The final reaction mixture was composed of 4mL of the Cu-TBTA solution, 1mL of the PEG or TFMPA alkyne solution, and 32 mg of sodium ascorbate (Aldrich) along with azide-terminated graphite nanopillar samples immersed therein. Typical reaction times were 3 h, after which the samples were rinsed with alternating washes of methanol and chloroform. FTIR was used to confirm the successful reaction.

4.3 Results

4.3.1 Block Copolymer Patterning

Figure 4.4 shows SEM images of the nickel-based nanoparticle array on the HOPG surface. The exact chemical composition of the nanoparticles is not known, as it may be the

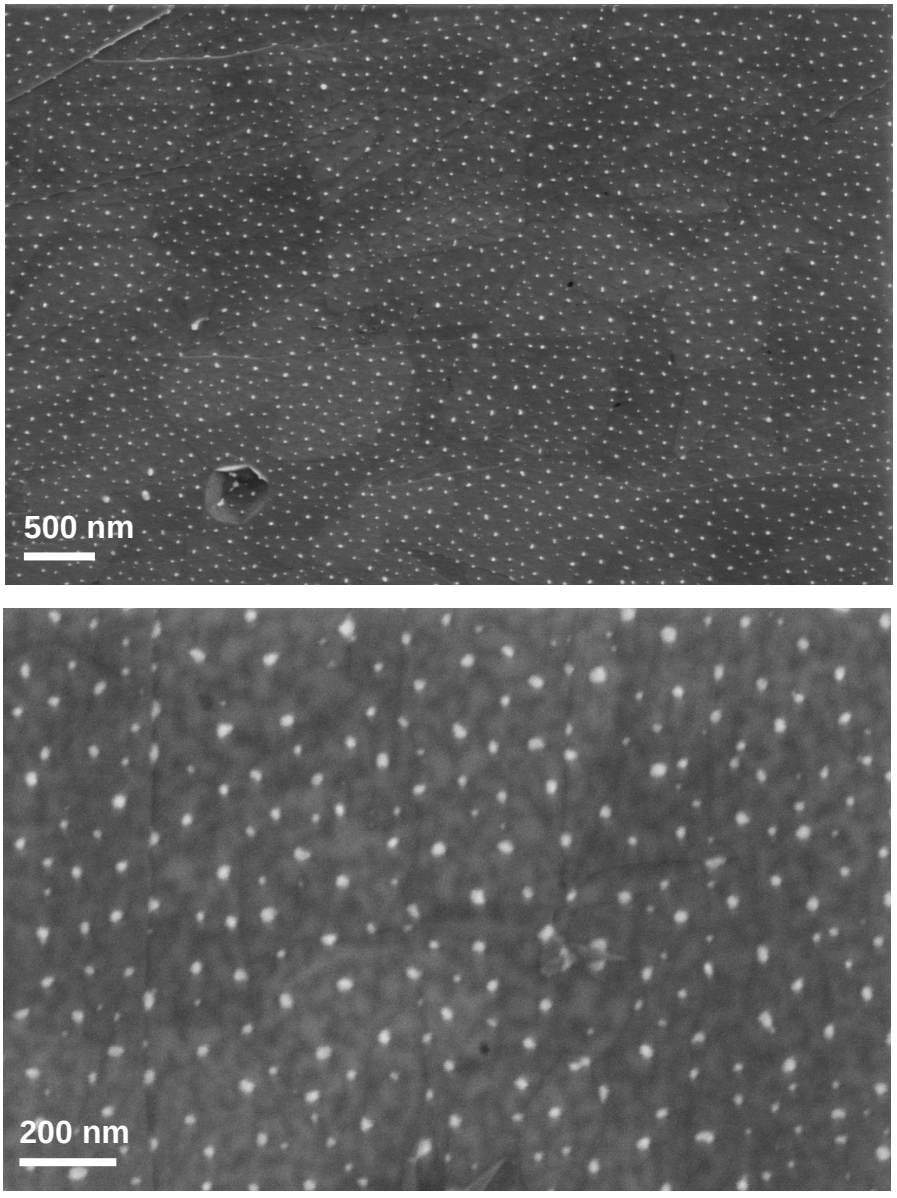

Figure 4.4. Scanning electron microscope images of nickel-based nanoparticles arrayed on an HOPG surface after removal of PS-b-2VP block copolymer. A 1kV accelerating voltage and a 4mm working distance were used to acquire the images.

original $NiCl_2$, or it may instead be some oxidized form created under exposure to the UV/O_3 treatment such as NiO. Nevertheless, the particles are relatively monodisperse in size, with diameters around 50 nanometers. Furthermore, they are well dispersed on the surface, with around 100 nm between each particle and its nearest neighbors. As shown in the first image, the particles are uniformly dispersed across the surface over distances of more than 10 microns. Notably, the particles do not display the highest possible degree of ordering, such as being in a hexagonal arrangement resulting from the micelles being close-packed. This is likely due to the fact that the surface is somewhat rough and the block copolymer does not undergo any thermal or solvent annealing processes, which might increase its long-range order after spin coating and before O_3 removal of the organic components. Nevertheless, long-range ordering is not necessary for generating the graphitic nanopillars described in the next section. It is sufficient for the particles to be relatively monodisperse in size and well spaced.

4.3.2 Nanopillar Formation

Using the nanoparticle arrays generated as described above, anisotropic etching with NH_3 produced nanopillars on the HOPG surface. Figure 4.5 shows SEM images of the nanopillars as formed by different plasma exposure times. For 30 and 60 second etch times as shown in Figure 4.5a and b, the pillars can be seen starting to form gradually, beginning as small hills before starting to gain vertical height with respect to the surface. Next, figure 4.5c shows the pillars after 5 minutes of etch time. The pillars now extend a moderate distance above the sample surface, with fairly vertical sidewalls at the top and some sloping at the base. Taking into account the 45° tilt of the microscope stage in these images, the pillar heights are approximately 250 nm,

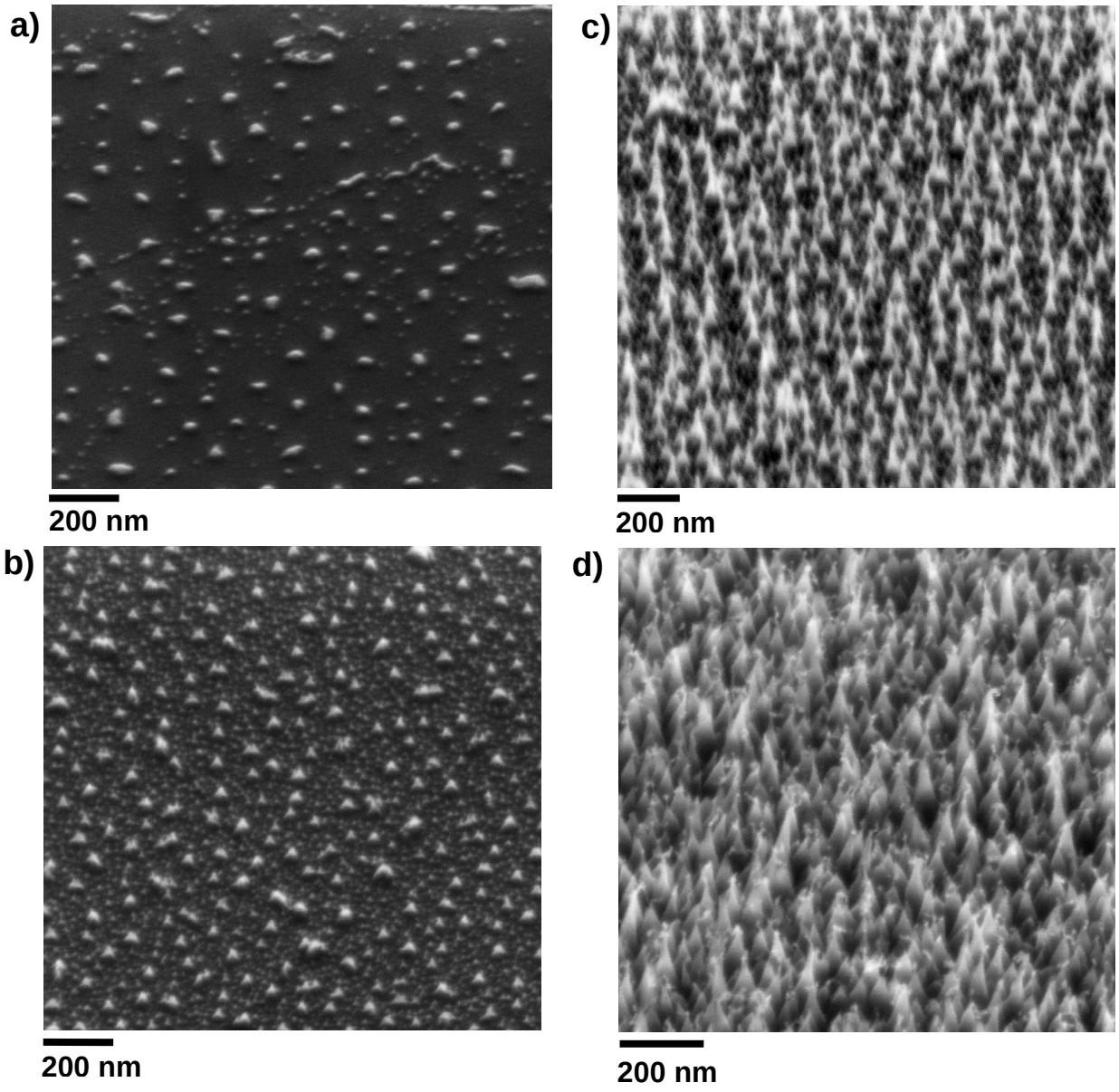

Figure 4.5. Scanning electron microscope images of graphitic nanopillars etched in NH_3 plasma for: **a)** 30 sec, **b)** 60 sec, **c)** 5 min, **d)** 15 min. All images recorded at 45° tilt angle, 5kV accelerating voltage, 14mm working distance.

corresponding to approximately 750 graphene layers. Finally, figure 4.5d shows the pillars after 15 minutes of etching time, at which point their vertical structure has started to break down. The etch must not be perfectly anisotropic in a vertical direction, and therefore some undercutting is occurring during the etch process. If the metal nanoparticle serving as the etch mask is dislodged as a result of undercutting, the etch will no longer form a pillar and instead will remove material from all areas, leading to destruction of the nanopillars. Thus, 5 min of etch time was found to produce the most well-formed pillars and was used for all future experiments.

4.3.3 Chemical Functionalization – Photochemical Grafting

Figure 4.6 shows FTIR spectra comparing neat liquid TFAAD to the graphitic nanopillars with TFAAD grafted to the surface. The black spectrum in Fig. 4.6a was obtained by subtracting the nanopillar-TFAAD sample spectrum from the spectrum of the same graphite nanopillar sample before reaction. Because of the rough and non-uniform surface of the nanopillar samples, this was found to be the best method for obtaining a reasonably flat baseline and the smallest number of interfering features from the graphite itself. As shown in the figure, the nanopillar-TFAAD sample displays many of the same bands seen for neat liquid TFAAD. Perhaps most telling are the three peaks near 1200 cm^{-1} that arise from the CF_3 group and are seen in both spectra. The amide C=O feature at approximately 1700 cm^{-1} is also quite strong, as are the CH features near 2850 and 2950 cm^{-1} that arise from the alkyl chain of the molecule. On the other hand, the small alkene C-H feature at approximately 2975 cm^{-1} that is present for neat TFAAD is not present in the surface-grafted spectrum, indicating that loss of the alkene is the source of the surface binding, consistent with literature results[25]. The doublet at approximately 2300 cm^{-1} is

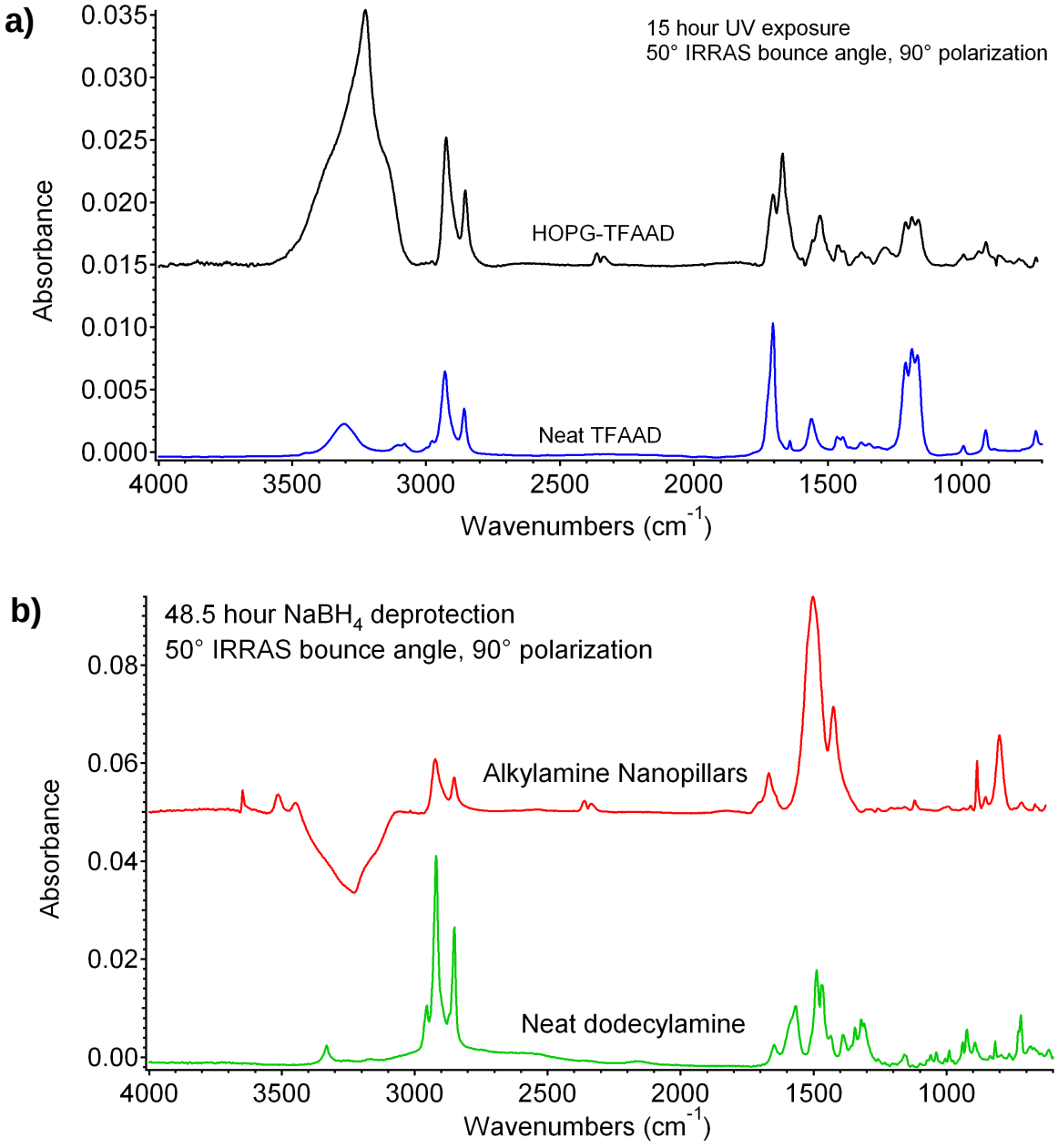

Figure 4.6. a) FTIR spectra showing the neat liquid TFAAD (bottom, blue curve) and graphitic nanopillars functionalized by photochemical grafting of TFAAD (top, black curve). **b)** FTIR spectrum showing the result of deprotection of the TFAAD-nanopillars (top, red curve) and a comparison spectrum of neat liquid dodecylamine (bottom, green curve).

simply due to atmospheric CO_2 and may be ignored. Slightly more mysterious is the large broad feature between 3100 and 3500 cm^{-1}. This broad feature may be due to adsorbed water, but that assignment is not certain. Also of note is the second C=O feature at around 1675 cm^{-1}, which is even larger than that due to the C=O feature from TFAAD itself. TFAAD has been noted to form multilayers in some grafting experiments[32], and so this second carbonyl peak may be due to monolayer formation through the end of TFAAD with the carbonyl, which is also the one farthest from the surface and thus more likely to react further.

The next step of the reaction is the deprotection of the surface-bound TFAAD where $NaBH_4$ is used to remove the trifluoroacetate group. Figure 4.6b shows FTIR spectra of the graphite nanopillar sample after deprotection as well as a reference consisting of neat dodecylamine. If the deprotection is completely successful and only a monolayer of TFAAD was formed on the surface, the species present after deprotection should be very similar to decylamine, which will differ only minimally from dodecylamine (merely in the ratio of the alkyl chain-derived infrared features to those deriving from the amine and methyl group ends of the molecule). First, in comparing the red spectrum of nanopillar-amine in Fig. 4.6b to the black spectrum of nanopillar-TFAAD in 4.6a, one immediately notes a number of changes. The three CF_3 features near 1200 cm^{-1} have completely disappeared and the C=O stretch near 1700cm^{-1} has been significantly reduced in size. The band remaining at this position may even be derived from another source besides the C=O of TFAAD, such as remaining carbonyl functionalities on the edge plane of the graphite itself. The large broad feature between 3100 and 3500 cm^{-1} has also become a negative feature, indicating that the unfunctionalized nanopillars had a stronger absorbance in this region than the nanopillar-amine sample.

The successful functionalization of the nanopillar graphite was also verified using XPS. Because of the presence of the trifluoroacetate group on the distal end of the TFAAD molecule, XPS analysis is relatively straightforward due to the unique signature of the CF_3 carbon as well as the presence of fluorine, which should not arise from any other source. Figure 4.7 shows the XPS spectra in the carbon (1s) and fluorine (1s) regions. First, in figure 4.7a, the carbon region shows a number of different signals. The largest feature, which is seen at relatively low binding energy (approximately 284.5 eV), is due to the underlying graphite substrate. Successively higher-binding energy peaks indicate the presence of other elements which withdraw electron density from carbon, causing the core 1s orbitals to be bound slightly more strongly to the now-partially-positive carbon atom. Two more features, appearing at approximately 285 and 286 eV, are most likely due to various surface atoms of the graphite (which may have oxygen functionalities) as well as the alkyl chain of TFAAD. Finally, we reach two small peaks which we can assign to carbon atoms with very electronegative neighbors. One, at approximately 288 eV, is most likely due to the carbonyl carbon of TFAAD, while the peak at highest binding energy, around 292 eV, is due to the CF_3 carbon. No other plausible source of such a high-binding carbon is present in this system, so the presence of the 292 eV peak is strongly indicative of successful TFAAD functionalization. Furthermore, in Figure 4.7b, the presence of a large amount of fluorine supports the assignment of the CF_3 carbon in TFAAD even more.

The final step in the reaction scheme is to functionalize the deprotected alkylamine-terminated nanopillars with long PEG chains with the goal of eventually increasing the solubility of the graphene nanodiscs. This is accomplished by using a PEG-based molecule with the

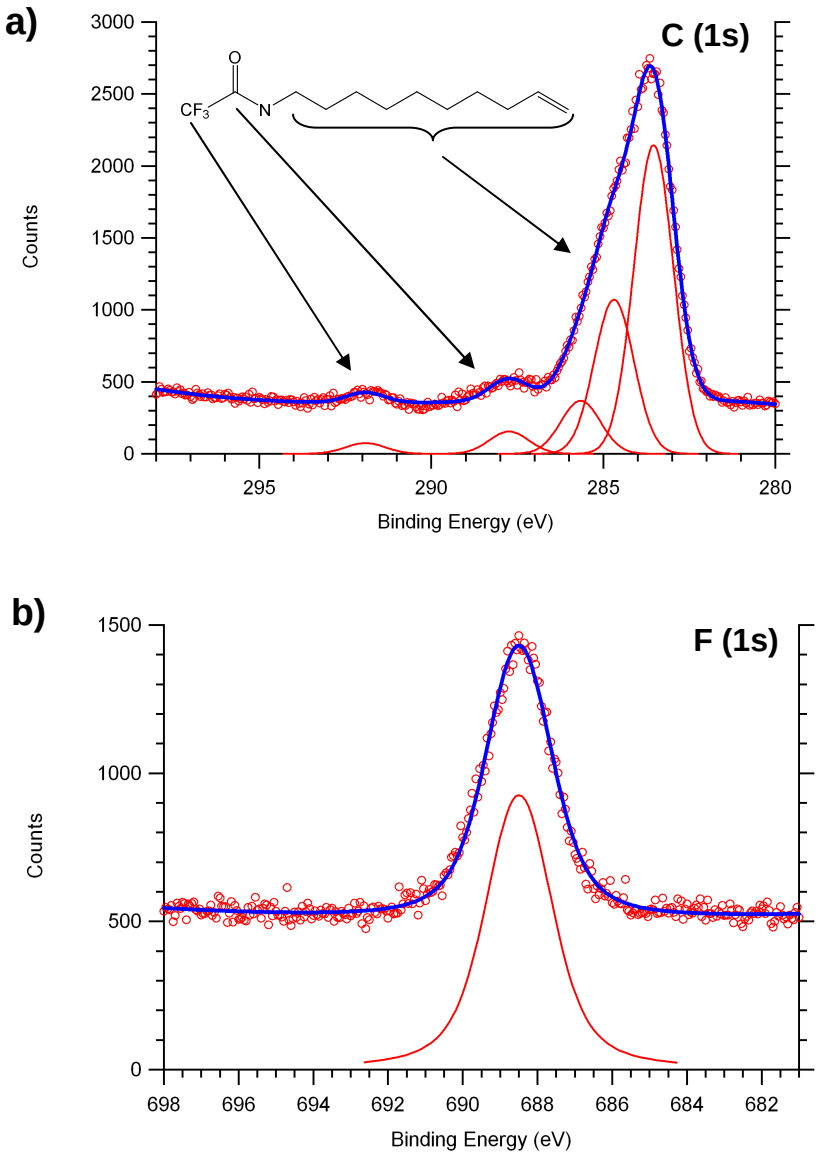

Figure 4.7. X-ray photoelectron spectroscopy (XPS) results for the TFAAD functionalization of graphitic nanopillars. The two higher-binding carbon peaks are indicative of the trifluoromethyl and the amide carbons, strong indicators of the presence of TFAAD on the surface. **a)** carbon (1s) region, **b)** fluorine (1s) region.

reactive N-hydroxyl succinimide group on one end. This group will react with the amine on the nanopillar surface to attach the PEG group to the alkyl chain of the surface-bound molecules. Figure 4.8 shows the reflectance FTIR spectrum of the nanopillars after reaction with PEG-NHS as well as the spectrum of neat PEG-NHS for reference (obtained by ATR). The strongest peak of the PEG-NHS molecule, at approximately 1100 cm^{-1}, is due to the C-O-C ether linkages of the PEG chain. This peak is quite weak in the nanopillar sample if it is indeed present at all. Furthermore, the nanopillar spectrum shows several other peaks, such as those at approximately 1650 cm^{-1} and 750 cm^{-1} that do not have an obvious correspondence to the PEG-NHS molecular spectrum. Therefore, it is difficult to conclude that the reaction proceeded to successfully attaching the PEG chains to the nanopillar surfaces, though at a minimum, the surface does appear quite spectrally different than the amine-terminated surface in Figure 4.6b.

4.3.4 Chemical Functionalization – CuAAC Reaction

To explore an alternative functionalization strategy, namely the CuAAC reactions commonly known as an example of “click” chemistry, the first step was to attach an azide group to the surface of the graphitic nanopillars. Figure 4.9 shows a region FTIR spectrum of the graphitic nanopillars after reaction with sodium azide and ICl. The peak at approximately 2100 cm^{-1} indicates the presence of an N_3 group on the surface of the nanopillars. This region of the FTIR spectrum is typically devoid of any other signals, and so there is little to no chance that this feature could be due to any other functional group.

Once the azide is present on the surface, the next step was to react the surface-bound azide with an alkyne, linking the two together into a triazole ring. Figure 4.10 shows FTIR

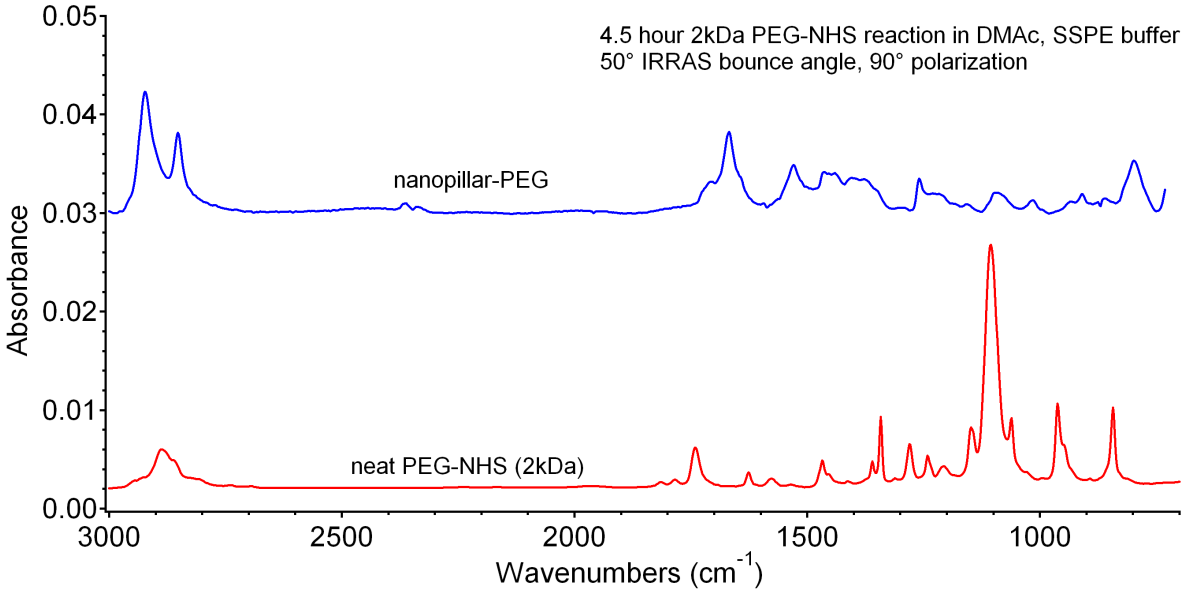

Figure 4.8. FTIR of neat N-hydroxyl succinimide poly(ethylene glycol) liquid (bottom, red) and graphitic nanopillars that underwent the reaction to functionalize with PEG-NHS (top, blue). The very strong C-O-C peak at approximately 1100 cm^{-1} present in the neat PEG-NHS liquid is either extremely small or not present at all in the nanopillar-PEG sample, and the nanopillar-PEG sample possesses numerous other peaks that do not obviously correspond to the PEG-NHS.

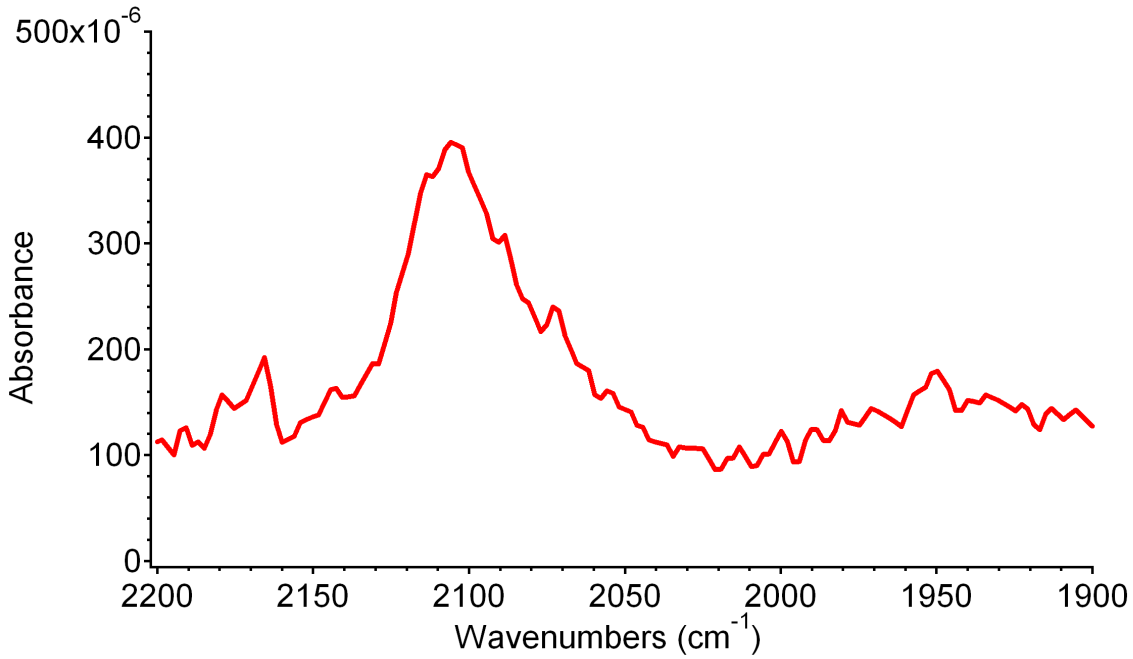

Figure 4.9. FTIR reflectance (IRRAS) spectrum of azide-functionalized pillars. The peak at approximately 2100 cm^{-1} indicates the successful formation of an azide on the surface of the nanopillars.

spectra of the resulting reaction using the molecule trifluoromethoxyphenylacetylene (TFMPA) as the alkyne. Even though this molecule is not expected to significantly alter the solubility of the eventual graphene nanodiscs, it provides a chemical tag in the form of the CF_3 group that assists in verifying the reaction's success via FTIR and XPS. The lowest spectrum (green) in figure 4.10 is that of neat liquid TFMPA for comparison purposes. Next, in black, we have the spectrum of the graphitic nanopillars that have undergone the full reaction conditions and have TFMPA attached to the surface. The three CF_3 peaks that appear near 1200 cm^{-1} are easily identifiable in both the green and black spectra, indicating the presence of the CF_3 group on the nanopillar surface. The feature at approximately 1500 cm^{-1}, due to the C-C bonds in the benzene ring of TFMPA, is also present in the nanopillar spectrum. For additional verification, two control experiments were performed, one with no $Cu(BF_4)_2$ and one with no TFMPA. Figure 4.9 also shows the FTIR spectra of the graphite nanopillars after these control reactions, shown in blue (no Cu) and red (no TFMPA). In both control spectra, the CF_3 peaks are not visible, nor is the C-C peak from the phenyl portion of the molecule. The features at approximately 1580 cm^{-1} and 850 cm^{-1} are from the graphite substrate and thus small differences between the sample and background spectra cause them to be either positive or negative in magnitude.

To further confirm the presence of the TFMPA on the surface of the nanopillars, XPS analysis was employed. Figure 4.11a shows the XPS spectrum for the fluorine (1s) region, which indicates that the amount of fluorine present is significantly higher for the sample that underwent the full click reaction than for either of the two controls. For the no-Cu control, the fluorine present most likely derived from physisorption of the TFMPA to the graphitic surface, or possibly TFMPA that did fully react with the surface even without the Cu catalyst. For the no-

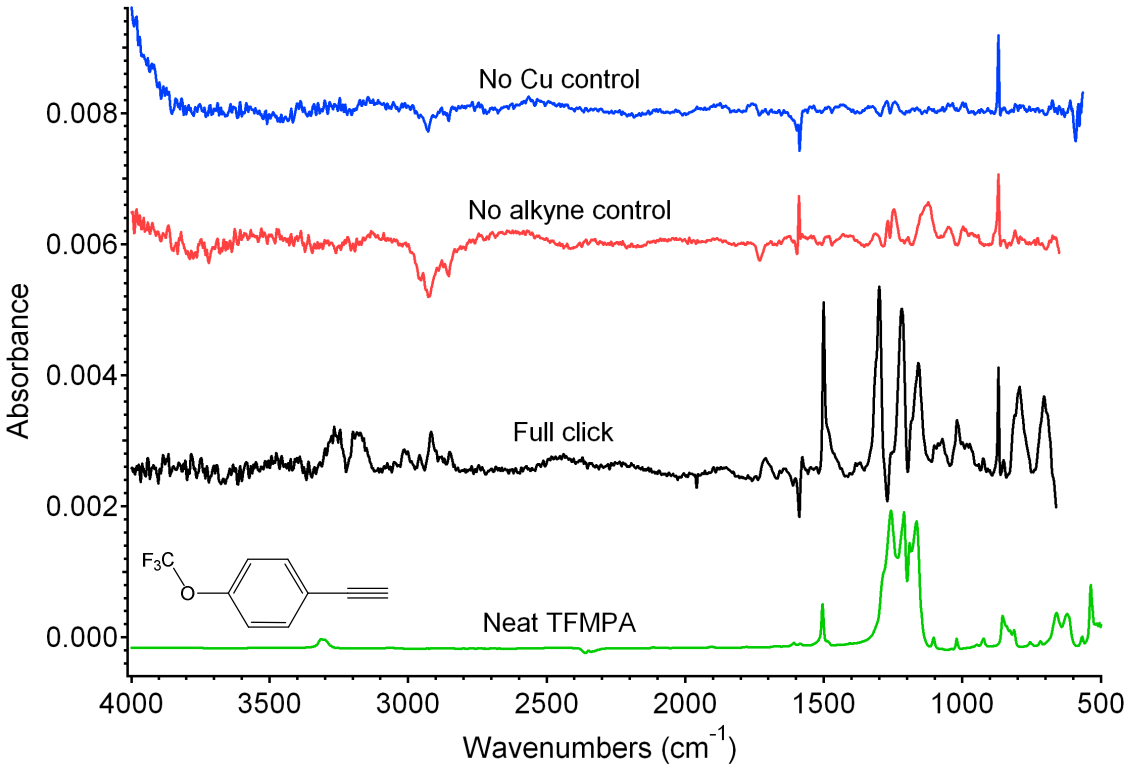

Figure 4.10. FTIR spectra of (green, bottom) neat trifluoromethoxyphenylacetylene (TFMPA) alkyne obtained by ATR as well as IRRAS spectra of (black, second from bottom) the full click reaction performed on graphitic nanopillars, (red, second from top) a control with no TFMPA alkyne, and (blue, top) a control with no Cu catalyst. The large CF_3 peaks near 1200 cm^{-1} and the phenyl C-C peak near 1500 cm^{-1} appear in the full click spectrum but not for either control.

alkyne control, the fluorine must derive from surface adsorption of at least the anion of the $Cu(BF_4)_2$ catalyst in some way. Figure 4.11b further confirms the successful reaction, as neither control spectrum shows detectable CF_3 – type carbon, while the CF_3 carbon in the full reaction sample is small but certainly present, at approximately 292 eV.

As the experiments with TFMPA showed, the click reaction steps all function as intended, so the reactions were repeated using a different alkyne. Specifically, the PEG-alkyne used in the second course of reactions is designed to impart greater solubility to the graphene nanoplatelets via its many ethylene glycol units. Since the PEG-alkyne does not have a similar, easily identifiable chemical tag as TFMPA, analysis was somewhat less straightforward. Figure 4.12a shows the FTIR spectra of the neat PEG-alkyne as well as a PEG-grafted nanopillar sample that experienced the full reaction conditions and a control sample that had no copper catalyst present for the reaction. Though the signals are quite small, the large C-O-C ether peak at approximately 1100 cm^{-1} does appear in the sample that had the copper catalyst present, while no such peak appears in the control sample that had no copper catalyst. In addition, Figure 4.12b shows XPS spectra for the carbon (1s) region of both the full reaction sample and the no-Cu control. The spectra clearly differ in the presence of lightly oxidized carbon at approximately 286.5 eV, which is consistent with carbon atoms in an ether[33]. Taken together, the FTIR and XPS results indicate that the click functionalization was successful, even with a molecule as large as the 1kDa poly(ethylene glycol)-alkyne.

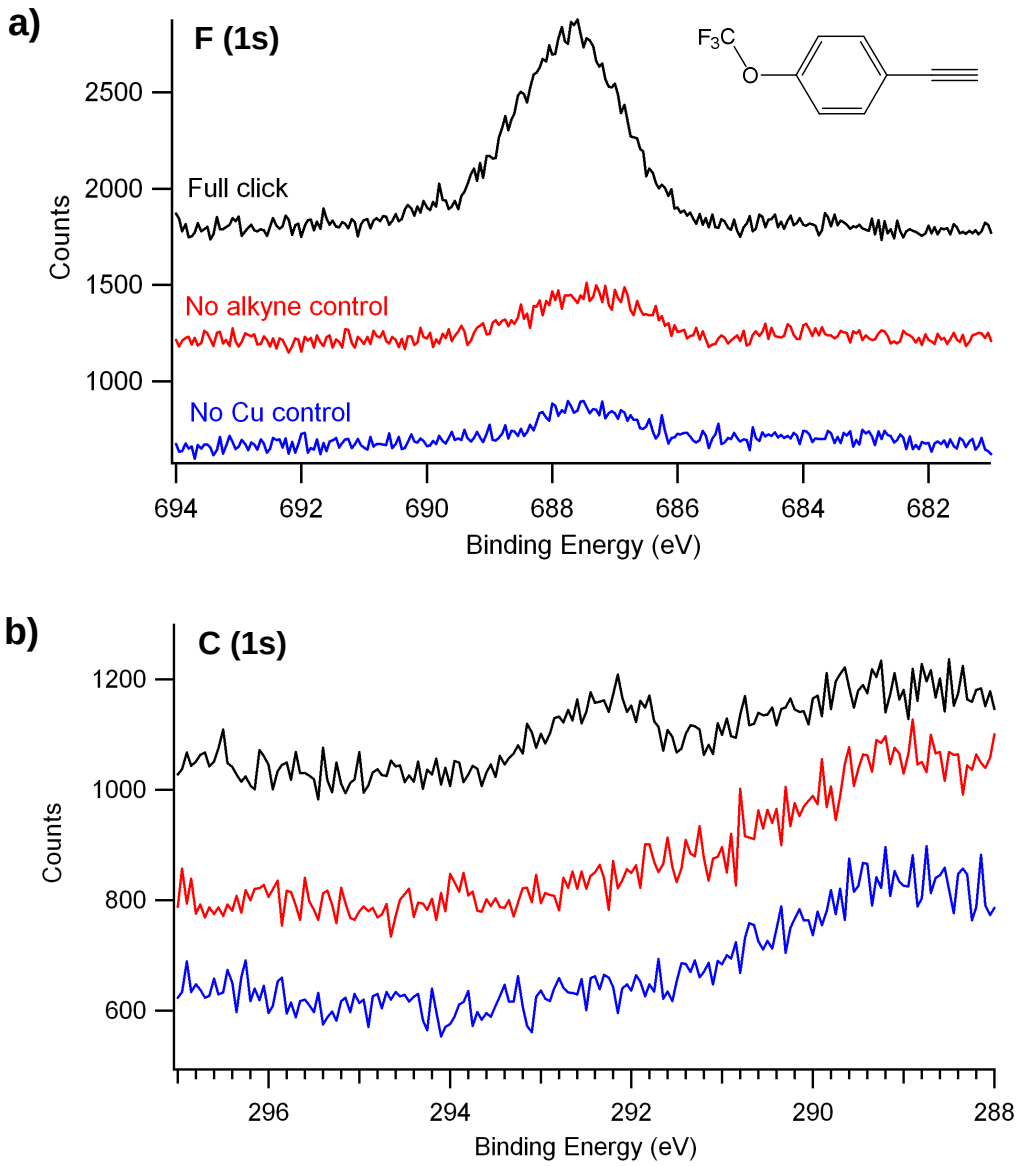

Figure 4.11. X-ray photoelectron spectroscopy (XPS) results for the CuAAC functionalization of graphitic nanopillars. **a)** The fluorine (1s) region of the spectrum, showing much larger F signal for the full reaction compared to two controls with one of the reagents omitted. **b)** The high-binding portion of the carbon (1s) region, showing higher CF_3-type carbon for the full reaction compared to either control.

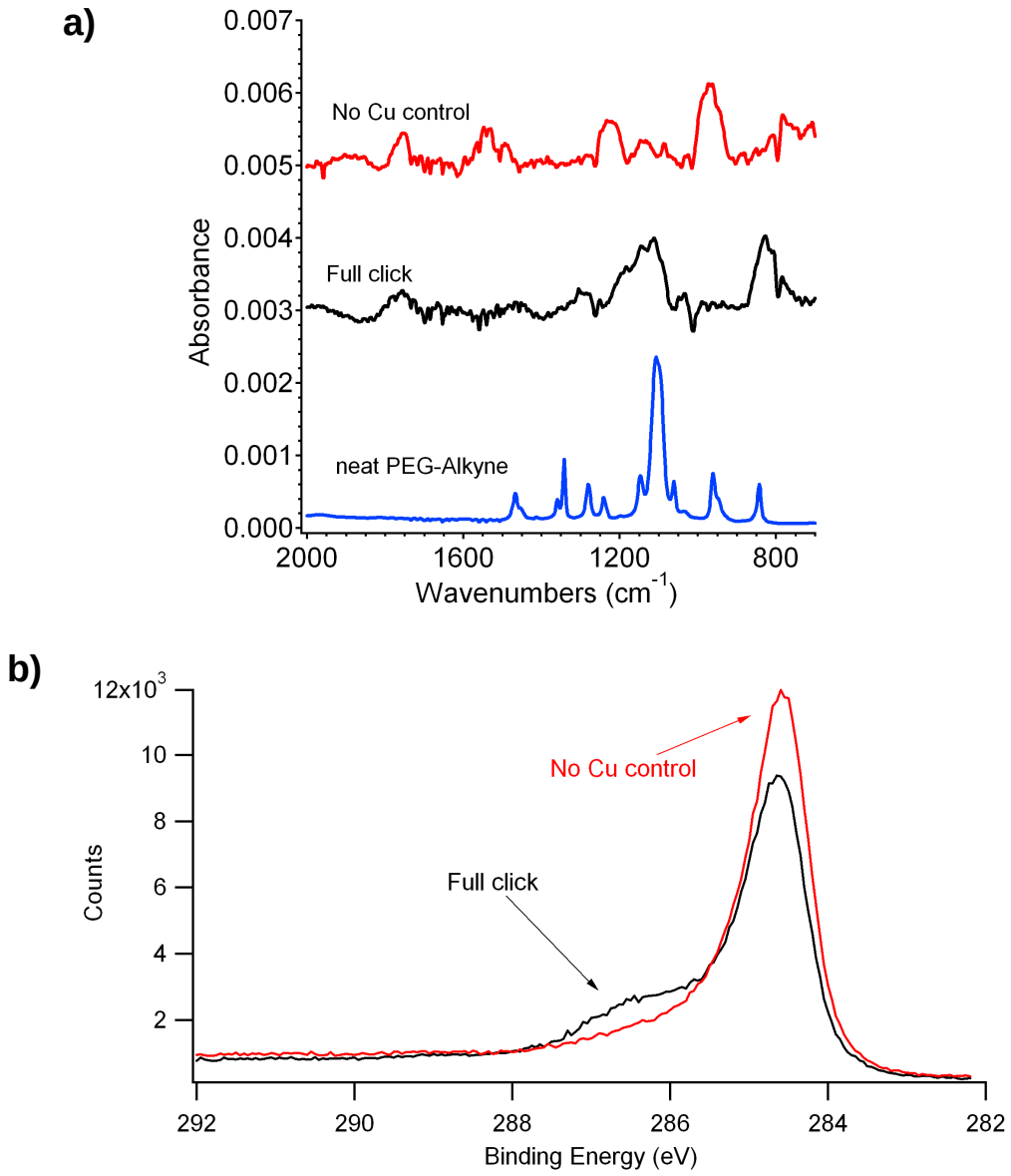

Figure 4.12. Spectroscopic results for the CuAAC functionalization of graphitic nanopillars with PEG groups. **a)** FTIR of the neat PEG-alkyne (bottom, blue), nanopillars that underwent the full reaction conditions (middle, black), and a control reaction performed with no copper catalyst (top, red). **b)** XPS of the carbon (1s) region of graphitic nanopillars functionalized with an alkyne-PEG (black) and a control reaction performed with no copper catalyst (red).

4.4 Discussion

The goal of obtaining graphitic nanopillars that are uniform in diameter, well spaced on the surface, and as tall as possible is not a trivial one, and in some ways these goals may compete against one another. The nanoparticle arrays shown in Figure 4.4 are obviously successful in serving as an etch mask for the nanopillars shown in Figure 4.5, though if the particles were more densely packed, more nanopillars per unit area could perhaps be obtained. This would lead to a higher eventual yield of graphene nanodiscs after exfoliation of the pillars. More densely packed pillars might also serve to enhance the anisotropy of the etching process, as one pillar could effectively serve as a shield to limit the undercutting of its neighboring pillars. The density and packing of the nanoparticle array is controlled by both the absolute size as well as the ratio of the two legs of the block copolymer. For the micelles used to create the arrays in these experiments, the block copolymer was 32.5 kDa of polystyrene units and 7.8 kDa of poly(2-vinyl pyridine) units. These lengths correspond to approximately 310 polystyrene units and 75 poly(2-vinyl pyridine) units, giving a PS:P(2VP) ratio of 4.1. Other block copolymer formulations were tried (results not shown), including some with 4-vinyl pyridine as the metal-coordinating block instead of 2-vinyl pyridine. These compositions included 50.9k-b-29.1k (2VP), 40k-b-5.6k (4VP), and 51k-b-18k (4VP). In addition, other metal salts were tried, including $FeCl_2$ and $TaCl_5$. These results are not shown as none of the other compositions of polymer and metal investigated produced the quality of nanoparticles seen in Figure 4.4. However, the possibility exists that the extreme tunability of block copolymers and the wide variety of metal salts available could lead to some film formation process that produced denser but still well-spaced and monodisperse arrays of nanoparticles.

In investigating the etch behavior of the nanoparticle arrays on the HOPG surfaces, Figure 4.5 indicates that there is a clear life cycle to the nanopillar etch process. Based on the fact that the nanopillars reach a height of approximately 200 nm in 5 minutes, we can estimate the vertical etch rate at approximately 40 nm/min. It is also clear from the SEM results that the pillars start to collapse between 5 and 15 minutes due to undercutting and eventual removal of the area supporting the nanoparticle etch mask. The radius of the pillar tops should be equal to that of the nanoparticle diameter itself, which is seen from Fig. 4.4 (and other SEM images, not shown) to be approximately 20 nm. Thus, if it takes approximately 10 minutes to completely remove the area at the top of each pillar, the horizontal etch rate must be approximately 2 nm/min. Therefore the anisotropy of this etch chemistry provides about a factor of 20 faster etch in the vertical direction than the horizontal. Other etch chemistries, for example using H_2 as the etch gas, were also investigated, but did not produce the well-formed pillars seen in Fig. 4.5. This may be due to the fact that NH_3 has a dipole moment (unlike H_2) and could be accelerated more effectively in the strong DC electric field of the plasma formation area. More efficient acceleration downward (perpendicular to the sample surface) would tend to produce more vertical collisions with the graphite and therefore a more anisotropic etch.

In terms of functionalization chemistry, the two synthetic strategies explored here offer different performances. As shown in Figures 4.6 and 4.7, the photochemical grafting strategy works quite well for the initial grafting step and the deprotection to the primary amine, but does not seem to produce significant PEG coverage for the last step of the reaction according to the FTIR data in Figure 4.8. That said, the surface obviously does change somewhat under the PEG-NHS reaction conditions, as seen in the disappearance of the 1500 cm^{-1} peak between Figure

4.6b and Figure 4.8. Put another way, if all steps in the reaction were successful, each TFAAD molecule would eventually give rise to 10 CH_2 groups from its own alkyl chain as well as approximately 45 CH_2CH_2O units that would be attached during PEG functionalization. Given that the size of the CH_2 peak near 2950 cm^{-1} does not change significantly between deprotection and attempted PEG functionalization (it is approximately 0.01 absorbance units in height in both cases), it is difficult to see how the PEG functionalization could be happening in significant amounts. Further evidence supporting this idea are results (not shown) of control experiments performed with the NHS ester of S-acetylthioglycolic acid (SATA-NHS). This small, sulfur-containing molecule has the same NHS reactive group as the PEG-NHS, and therefore would be expected to react with the amine-terminated surface of the deprotected TFAAD, but no sulfur was detected in XPS experiments with graphitic nanopillars reacted with SATA-NHS.

On the other hand, the "click" chemistry route appears more successful. Both the azide termination and the second "click" step with the alkyne show strong FTIR and XPS indications of success. This is the case for both the small-molecule TFMPA alkyne shown in Figures 4.10 and 4.11 as well as the long-chain PEG-alkyne shown in Figure 4.12. In the end, this is not surprising, as the CuAAC reaction was chosen as an example of "click" chemistry precisely for its selectivity and reliability[29]. The functionalization scheme here may also benefit from being two steps instead of the three required for the photochemical grafting, deprotection, and NHS functionalization route. Though further experimentation may reveal a way for the photochemical grafting route to become practically workable for this application, there is little call for such investigation as the CuAAC reaction has proven to be easily applied and successful in this study.

4.5 Conclusion

Block copolymer patterning using a metal salt that was selectively soluble in only one block proved to be an effective method for creating well-separated, monodisperse arrays of Ni-based nanoparticles on a well-ordered graphite substrate. Despite the small dimensions involved, using a very anisotropic etch process with NH_3 gas, these nanoparticles served as the mask in order to create vertically aligned graphitic nanopillars on the surface of the graphite. Because of the preservation of the original horizontal alignment of the graphene layers in the substrate, the sidewalls of the nanopillars expose exclusively edge plane graphite. Two functionalization strategies were investigated for tethering molecules to these edge planes. The first, photochemical grafting of an alkene, performed admirably in the first step but led to difficulties in the subsequent chemical steps. Specifically, the NHS-group reaction with a surface-bound amine appeared to be more difficult than anticipated. Conversely, the copper-catalyzed azide-alkyne cycloaddition (CuAAC) reaction strategy proved to be quite effective at modifying the graphite surfaces, first with an azide group and then with the subsequent “click” reaction to add an alkyne, of which two successful examples were presented. These patterning and functionalization strategies may one day be part of a route to monodisperse, functionalized graphene nanoplatelets.

4.6 References

(1) Chung, D. D. L. *Journal of Materials Science*, **2002**, *37*, 1475.

(2) Rice, R. J.; McCreery, R. L. *Analytical Chemistry*, **1989**, *61*, 1637.

(3) Geim, A. K. *Science*, **2009**, *324*, 1530.

(4) Geim, A. K.; Novoselov, K. S. *Nature Materials*, **2007**, *6*, 183.

(5) Novoselov, K. S.; Fal'ko, V. I.; Colombo, L.; Gellert, P. R.; Schwab, M. G.; Kim, K. *Nature*, **2012**, *490*, 192.

(6) Peierls, R. E. *Annales de l'Institut Henri Poincaré*, **1935,** *5*, 177.

(7) Landau, L. *Physikalische Zeitschrift der Sowjetunion*, **1937**, *11*, 26.

(8) Novoselov, K. S.; Geim, A. K.; Morozov, S. V.; Jiang, D.; Zhang, Y.; Dubonos, S. V.; Grigorieva, I. V.; Firsov, A. A. *Science*, **2004**, *306*, 666.

(9) Novoselov, K. S.; Jiang, D.; Schedin, F.; Booth, T. J.; Khotkevich, V. V.; Morozov, S. V.; Geim, A. K. *Proceedings of the National Academy of Sciences*, **2005**, *102*, 10451.

(10) Novoselov, K. S.; Geim, A. K.; Morozov, S. V.; Jiang, D.; Katsnelson, M. I.; Grigorieva, I. V.; Dubonos, S. V.; Firsov, A. A. *Nature*, **2005**, *438*, 197.

(11) Stankovich, S.; Dikin, D. A.; Dommett, G. H. B.; Kohlhaas, K. M.; Zimney, E. J.; Stach, E. A.; Piner, R. D.; Nguyen, S. T.; Ruoff, R. S. *Nature*, **2006**, *442*, 282.

(12) Schniepp, H. C.; Li, J. L.; McAllister, M. J.; Sai, H.; Herrera-Alonso, M.; Adamson, D. H.; Prud'homme, R. K.; Car, R.; Saville, D. A.; Aksay, I. A. *Journal of Physical Chemsitry B*, **2006**, *110*, 8535.

(13) McAllister, M. J.; Li, J.-L.; Adamson, D. H.; Schniepp, H. C.; Abdala, A. A.; Liu, J.; Herrera-Alonso, M.; Milius, D. L.; Car, R.; Prud'homme, R. K.; Aksay, I. A. *Chemistry of Materials*, **2007**, *19*, 4396.

(14) Cai, D.; Song, M. *Journal of Materials Chemistry*, **2007**, *17*, 3678.

(15) Bagri, A.; Mattevi, C.; Acik, M.; Chabal, Y. J.; Chhowalla, M.; Shenoy, V. B. *Nature Chemistry*, **2010**, *2*, 581.

(16) Moon, I. K.; Lee, J.; Ruoff, R. S.; Lee, H. *Nature Communications*, **2010**, *1*, 73.

(17) Tung, V. C.; Allen, M. J.; Yang, Y.; Kaner, R. B. *Nature Nanotechnology*, **2008**, *4*, 25.

(18) Shao, Y.; Wang, J.; Engelhard, M.; Wang, C.; Lin, Y. *Journal of Materials Chemistry*, **2010**, *20*, 743.

(19) Li, X.; Cai, W.; An, J.; Kim, S.; Nah, J.; Yang, D.; Piner, R.; Velamakanni, A.; Jung, I.; Tutuc, E.; Banerjee, S. K.; Colombo, L.; Ruoff, R. S. *Science*, **2009**, *324*, 1312.

(20) Li, X.; Cai, W.; Colombo, L.; Ruoff, R. S. *Nano Letters*, **2009**, *9*, 4268.

(21) Kwon, S.-Y.; Ciobanu, C. V.; Petrova, V.; Shenoy, V. B.; Bareno, J.; Gambin, V.; Petrov, I.; Kodambaka, S. *Nano Letters*, **2009**, *9*, 3985.

(22) Yan, X.; Cui, X.; Li, L.-S. *Journal of the American Chemical Society*, **2010**, *132*, 5944.

(23) Wang, X.; Ruther, R. E.; Streifer, J. A.; Hamers, R. J. *Journal of the American Chemical Society*, **2010**, *132*, 4048.

(24) Strother, T.; Knickerbocker, T.; Russel, Jr., J. N.; Butler, J. E.; Smith, L. M.; Hamers, R. J. *Langmuir*, **2002**, *18*, 968.

(25) Franking, R. A.; Landis, E. C.; Hamers, R. J. *Langmuir*, **2009**, *25*, 10676.

(26) Benson, M. C.; Ruther, R. E.; Gerken, J. B.; Rigsby, M. L.; Bishop, L. M.; Tan, Y.; Stahl, S. S.; Hamers, R. J. *ACS Applied Materials & Interfaces*, **2011**, *3*, 3110.

(27) Ruther, R. E.; Franking, R. Huhn, A. M.; Gomez-Zayas, J.; Hamers, R. J. *Langmuir*, **2011**, *27*, 10604.

(28) Metz, K. M.; Goel, D.; Hamers, R. J. *Journal of Physical Chemistry C*, **2007**, *111*, 7260.

(29) Kolb, H. C.; Finn, M. G.; Sharpless, K. B. *Angewandte Chemie*, **2001**, *40*, 2004.

(30) Li, J. Q. *Journal of Physical Chemistry C*, **2008**, *112*, 10345.

(31) Devadoss, A.; Chidsey, C. E. D. *Journal of the American Chemical Society*, **2007**, *129*, 5370.

(32) Franking, R; Hamers, R. J. *Journal of Physical Chemistry C*, **2011**, *115*, 17102.

(33) Moulder, J. F.; Stickle, W. F.; Sobol, P. E.; Bomben, K. D. *Handbook of X-ray Photoelectron Spectroscopy*, Perkin-Elmer Corp., Eden Prairie, MN, 1992.

Chapter 5

Summary and Future Directions

5.1 Summary

This work has primarily focused on the use of silicon as an anode material for next-generation lithium and lithium-ion batteries. These battery systems already occupy a very important place in the modern technological landscape, and their importance will only continue to grow as we seek to implement large-scale renewable energy generation in our society. Use of renewable energy sources such as solar and wind energy necessitate batteries to store energy for times when the wind is calm or the sun is not shining. Next-generation lithium and lithium-ion batteries will have higher capacities, necessitating new electrode materials, and will be safer, necessitating new electrolytes. As with any complex system, with these new components must also come understanding of their interrelationships in order to design the best batteries possible.

In the first portion of this thesis, a method of constructing lithium primary batteries that can operate at extremely high temperatures was described. These batteries can reach temperatures of 190 °C, which is above the melting point of lithium and is a temperature regime reached by only a very small number of battery systems previously reported. The battery performance was found to depend somewhat on the electrolyte, and an organosilicon compound, F1S3M2, was found to offer the best performance. The cause of the electrolyte dependence and some electrode capacity loss were assigned to decomposition of the SEI forming on the anode surface. This work may lead to practical battery systems for deep-earth exploration robotics, which need to be powered autonomously in environments with extremely high ambient temperatures.

Next, a more fundamental study on the SEI layer formation of organosilicon electrolytes on silicon anodes was undertaken. Organosilicon electrolytes offer much higher safety than current battery electrolytes and can be structurally tailored and blended to have all the same advantages as the current state of the art electrolytes as well. The SEI formation on single-crystal silicon was found to be strongly voltage-dependent and relatively fast, occurring on a timescale of minutes. Through a detailed correlation analysis, the main features of the SEI were an initial formation of a phosphorus- and fluorine-rich layer followed by a later deposition of a carbon- and oxygen-rich layer. These results should lead to a better understanding of the SEI formation on other forms of silicon as well.

Finally, in a somewhat different vein, the patterning, synthesis, and functionalization of graphitic nanopillars was successfully demonstrated and characterized. Because of the immense interest in graphene in recent years, methods have been sought (with limited success) for reliable syntheses of well-characterized graphitic and graphenic structures. In this portion of the work, block copolymer patterning of a metal salt was used to create a well-ordered array of nanoparticles on a graphite surface. A plasma etching process was then used to create well-separated graphitic nanopillars that were relatively monodisperse in diameter. Finally, chemical functionalization of these nanopillars was investigated via two methods: a photochemical grafting-based reaction and an azide-alkyne “click” reaction. The click chemical route was found to be more reliable and successful in functionalizing the nanopillars with a selection of different molecules. These studies may one day lead to soluble graphene nanoplatelets, which would be an interesting material for the continuing explorations of graphene’s unique properties.

5.2 Future Directions

5.2.1 High-Temperature CF_x / LiSi Battery Systems

One major question remaining with regards to the high-temperature battery systems explored in Chapter 2 is how much of the irreversible capacity loss may be recovered by using a different chemistry. The F1S3M2 electrolyte proved to offer the best performance with the silicon anodes, while germanium anode cells performed better than silicon anode cells when both used tetraglyme-based electrolyte. It remains to be determined if a cell using F1S3M2 electrolyte and a germanium anode would perform better still. If not, then a more complex relationship of electrolyte (and, presumably, the SEI layer formed from it) and anode surface is implied, where the two must be co-optimized in order to see performance benefits. Furthermore, F1S3M2 is far from the only organosilicon compound that has been synthesized for battery usage, and other related electrolyte solvents are an obvious next step to explore in the quest for even better performance.

The principal conclusion of the work presented in this thesis is that at high temperature, the SEI layer that forms on the silicon anode is not stable, and most likely dissolves back into the electrolyte from whence it came. One strategy to attempt to solve this problem, then, would be to aim for electrolyte components that could form a more stable SEI layer, perhaps most easily through cross-linking of the SEI species that form on the surface. This could occur because of majority components like the electrolyte solvent or salt themselves, or through the use of additives. Indeed, many optimized electrolytes already contain additives such as vinyl carbonate or fluoroethylene carbonate[1,2] that are believed to enhance the SEI layer's structure. The use of

additives such as these was not explored in the work presented here, but is an attractive next step for future work.

Lastly, the anode used in these cells was less than ideal in a major respect – namely, commercial battery systems generally use microscale particles of active material in a binder/carbon black matrix. The smaller size of the active material particles increases the surface area available for lithium intercalation and deintercalation, enhancing the rate capability of the batteries. In the cells described in Chapter 2, bulk silicon wafer anodes were used, which will certainly be less well-performing than nanoscale silicon particles as have recently been shown to be superior[3]. If better-performing electrolytes/SEI layers are discovered, it may enable the use of such micro- or nanoparticle electrode materials, enhancing the practicality of these battery systems. It would also enhance the possibility of repeated cycling if a secondary cathode material were used that was as thermally stable as CF_x with the added ability of being able to be repeatedly charged and discharged. $LiFePO_4$ is one possible candidate for such cells[4].

5.2.2 SEI Formation on Single-Crystal Si Anodes From Organosilicon Electrolytes

The studies presented in Chapter 3 indicate that the SEI formation on single-crystal silicon wafer samples proceeds primarily as a function of voltage, and consists of an early fluorine- and phosphorus-enriched layer than subsequently becomes covered by a carbon- and oxygen- enriched layer. Though the voltage points selected for this study were able to flesh out these crucial details, one obvious direction for future studies is to more fully establish more exact voltage points at which compositional changes in the SEI occur. Shorter time points would also be useful to pinpoint the time scale of SEI formation more accurately.

Another area for further research is how much the SEI formation depends on the nature of the silicon electrode. The end goal of all of these studies must necessarily apply to nanoscale silicon of some type, as it is well established that the best cycling performance is only attained with silicon nanomaterials[5,6]. The samples investigated in these studies had a native oxide present on the silicon surface; it is known that the oxide can play a role in SEI formation through the formation of lithiated silicon oxide[7] or fluorinated silicon oxide[8], so studies examining the effect of removing the native oxide on the SEI would be of great interest. The crystal face, doping type (n- or p-type), and dopant level might also have effects on the SEI formation, probably most likely in terms of the "onset" voltages of electrolyte decomposition.

Finally, once SEI formation on silicon is sufficiently well understood, one might imagine a more intentional process for SEI design, wherein some aspect of the cell chemistry is intentionally tailored to form a "designed" SEI instead of simply relying on whatever decomposition reactions of the electrolyte occur on the electrode surface. This could be done by including additives (generally present as a small percentage) in the electrolyte, which is already done in some cases[9], or even by structural design and synthesis of the electrolyte solvent itself. The ideal silicon SEI would be very mechanically compliant (probably by inclusion of long cross-linking chains) electrochemically stable once formed, very conductive to both electrons (to maintain electrical contact between the Si particles it joins), and porous to Li^+ cations. Future studies such as these may even integrate the currently separate roles of binder and SEI, which would be a triumph for rational battery electrode design.

5.2.3 Functionalized Graphite Nanopillars as a Route to Graphene Nanoplatelets

In the work described in chapter 4, though the chemical functionalization of the graphite nanopillars was successful in both synthetic strategies, the main questions remaining have to do with the utility of the functionalization. The eventual goal of the project is to produce soluble graphene nanoplatelets by virtue of the long soluble chains grafted onto the pillars. Nevertheless, the thermodynamics of the system still present a challenge. Specifically, the idea was that the grafted side chains would provide a thermodynamic driving force to solublizing the nanoplatelets. However, even in the nanopillar geometry the side chains are at least partially accessible to the solvent, and they may even be completely solvated depending on the grafting density. The enthalpic difference between the nanopillars and the soluble nanoplatelets is therefore expected to be minimal as far as the side chains are concerned, though at least the separated nanoplatelets in solution are entropically favored. Enthalpically, though, the main difference is the energetic penalty paid when the basal planes of the platelets are separated from one another, which can be quite large despite the fact that graphene layers do slide across one another (generally under macroscopic forces). In order to accomplish the end goal of the project, then, some way around this obstacle must be envisioned.

One method for increasing the solubility of the nanoplatelets is to use a solvent known to have favorable interactions with conjugated carbons. There has been already been some work on this subject with regards to graphene[10]. Certain pyrrolidones such as N-methyl and N-cyclohexyl pyrrolidone seem to perform well in these applications. One might even imagine a similar functionalization scheme to the ones described above but with a pyrollidone-containing polymer

replacing the PEG. Such a functionalized polymer might easily slip between the graphene layers, exfoliating the platelets easily.

Another possible way to encourage the graphene nanoplatelets to separate would be chemical or electrochemical intercalation into the spaces between the layers, for example with an alkali metal. A very large number of graphite intercalation compounds are known[11], some of which increase the interlayer spacing of the graphite significantly. The best choice would probably be an intercalant that forms stage 1 compounds, where the intercalant is present between every layer and its neighbors. This sort of intercalation scheme would be expected to produce monolayer graphene discs after exfoliation. Having said this, an interesting side direction would be to form stage 2 compounds, which alternate layers with intercalants present and layers with the natural graphite spacing and no intercalant species. Exfoliation of this sort of compound might be expected to produce predominantly bilayer graphene, which has turned out to be an interesting material in its own right[12].

Finally, the best way to increase the applicability of the graphite nanopillars would be to find ways to increase the potential yield and selectivity of the syntheses. In the samples described in chapter 4, the surface was covered with nanopillars approximately 200 nm tall, but if taller pillars could be successfully created, the potential yield of graphene nanoplatelets would be that much larger. The best way to accomplish this goal would be a more anisotropic etch process with minimal undercutting, either using a different etch chemistry or different plasma-generating electronics such as a higher electric field. In addition, graphite slabs such as the ones used in these studies will always have “non-pillar” areas on the sides and bases beneath the pillars, and any conceivable exfoliation method might also remove material from those edges as well.

Removal from the “non-pillar” areas would be expected to produce graphite flakes of uncontrolled size and thickness. Having too much of such material around would make isolation of the true graphene nanoplatelets a serious challenge, and thus any way to increase the selectivity of the process for only the one-layer-thick nanoplatelets would be of very large benefit.

5.3 References

(1) McMillan, R.; Slegr, H.; Shu, Z. X.; Wang, W. *Journal of Power Sources*, **1999**, *81-82*, 20.

(2) Choi, N.-S.; Yew, K. H.; Lee, K. Y.; Sung, M.; Kim, H.; Kim, S.-S. *Journal of Power Sources*, **2006**, *161*, 1254.

(3) Liu, X. H.; Zhong, L.; Huang, S.; Mao, S. X.; Zhu, T.; Huang, J. Y. *ACS Nano,* **2012**, *6*, 1522.

(4) Kurita, T.; Lu, J.; Yaegashi, M.; Yamada, Y.; Nishimura, S.; Tanaka, T.; Uzumaki, T.; Yamada, A. *Journal of Power Sources*, **2012**, *214*, 166.

(5) Wu, H.; Cui, Y. *Nano Today*, **2012,** *7*, 414.

(6) Liu, X. H.; Zhong, L.; Huang, S.; Mao, S. X.; Zhu, T.; Huang, J. Y. *ACS Nano,* **2012**, *6*, 1522.

(7) Philippe, B.; Dedryvère, R.; Allouche, J.; Lindgren, F.; Gorgoi, M.; Rensmo, H.; Gonbeau, D.; Edström, K. *Chemistry of Materials,* **2012,** *24*, 1107.

(8) Philippe, B.; Dedryvère, R.; Gorgoi, M.; Rensmo, H.; Gonbeau, D.; Edström, K. *Chemistry of Materials*, **2013,** *25*, 394.

(9) Nie, M.; Abraham, D. P.; Chen, Y.; Bose, A.; Lucht, B. L. *Journal of Physical Chemistry C*, **2013**, *117,* 13403.

(10) Hernandez, Y.; Nicolosi, V.; Lotya, M.; Blighe, F. M.; Sun, Z.; De, S.; McGovern, I. T.; Holland, B.; Byrne, M.; Gun'Ko, Y. K.; Boland, J. J.; Niraj, P.; Duesberg, G.; Krishnamurthy, S.; Goodhue, R. Hutchison, J.; Scardaci, V.; Ferrari, A. C.; Coleman, J. N. *Nature Nanotechnology*, **2008**, *3*, 563.

(11) Dresselhaus, M. S.; Dresselhaus, G. *Advances in Physics*, **2002**, *51*, 1.

(12) Ohta, T.; Bostwick, A.; Seyller, T.; Horn, K.; Rotenberg, E. *Science*, **2006,** *313*, 951.